Airborne Measurements of the Spectral Surface Albedo over Morocco and its Influence on the Radiative Forcing of Saharan Dust

Dissertation

zur Erlangung des Grades
"Doktor
der Naturwissenschaften"
am Fachbereich 08
der Johannes Gutenberg-Universität
in Mainz

Eike Bierwirth

geb. in Hannover

Mainz, den 6.5.2008

Summary

This PhD thesis deals with “airborne measurements of the spectral surface albedo over Morocco and its influence on the radiative forcing of Saharan dust”. It is embedded into the DFG research project SAMUM, the Saharan Mineral Dust Experiment which investigates the optical and microphysical properties of Saharan dust aerosol, its transport, and its radiative effect. The SMART-Albedometer is extended in its spectral range and applied in a field campaign within SAMUM which was conducted in May–June 2006 in south-eastern Morocco. At two ground stations and aboard two aircraft measurements in an almost pure plume of Saharan dust were conducted. Airborne measurements of the spectral upwelling and downwelling irradiance are used to derive the spectral surface albedo in its typical range in the experiment region. Typical spectral types are presented and compared to the surface albedo derived from MISR satellite data. Furthermore, the radiative forcing of the observed Saharan dust is estimated in dependence on the surface albedo and its regional variations.

Zusammenfassung

Die vorliegende Dissertation (in englischer Sprache) beschäftigt sich mit dem Thema ”Flugzeuggetragene Messungen der spektralen Bodenalbedo in Marokko und ihr Einfluss auf den Strahlungsantrieb von Saharastaub”. Sie ist thematisch eingebettet in die DFG-Forschungsgruppe SAMUM (Saharan Mineral Dust Experiment), die die optischen und mikrophysikalischen Eigenschaften von Saharastaub in der Atmosphäre, seinen Transport und seinen Strahlungsantrieb untersucht. Zunächst wird das Messgerät, das SMART-Albedometer, und die technische Erweiterung seines Wellenlängenbereiches beschrieben. Im Mai–Juni 2006 wurde in Südost-Marokko ein Feldexperiment organisiert, in dem mit Hilfe von zwei Bodenstationen und zwei Forschungsflugzeugen Messungen in nahezu reinem Saharastaub-Aerosol durchgeführt wurden. Spektrale Messungen der auf- und abwärtsgerichteten Strahlungsflussdichte an Bord eines Flugzeuges werden genutzt, um daraus die spektrale Bodenalbedo für verschiedene Gebiete in den Provinzen Ouarzazate und Zagora des Königreiches Marokko abzuleiten. Typische Spektralverläufe werden gezeigt, und mit zeitgleichen Messungen des Satelliteninstruments MISR verglichen. Darüber hinaus wird der Strahlungsantrieb des beobachteten Saharastaubes in Abhängigkeit von der spektralen Bodenalbedo und deren Variationen untersucht.

D77 – Mainzer Dissertation

Contents

1 Introduction

1.1 The climatic relevance of desert dust

Climate is described by physical variables which include the different forms of energy — temperature, wind, electromagnetic radiation — and thermodynamic quantities such as pressure and humidity. The time interval of the statistics of climate variables is defined as 30 years by the World Meteorological Organization (WMO). While the global climate has changed considerably in the history of the Earth, the currently observed trends indicate that changes occur at an unprecedented speed. The scientific knowledge about this process is revised by the Intergovernmental Panel on Climate Change (IPCC), an organisation set up by the WMO and the United Nations Environment Programme (UNEP). It is summarised in a series of reports, the most recent of which appeared in 2007 (a.o., Forster *et al.*, 2007). The report concludes that "humans have exerted a substantial warming influence on climate", with an estimated global anthropogenic radiative forcing[1] of $+1.6[-1.0, +0.8]\,\mathrm{W\,m^{-2}}$. While one of the major atmospheric agents — greenhouse gases with a radiative forcing of $+(2.63 \pm 0.26)\,\mathrm{W\,m^{-2}}$ — is classified at a *high* level of scientific understanding, the radiative forcing of aerosol particles of $-(0.5 \pm 0.4)\,\mathrm{W\,m^{-2}}$ is rated at a *medium-low* level of scientific understanding. The radiative forcing of the various aerosol components is even less certain; that of mineral dust is estimated as $-(0.1 \pm 0.2)\,\mathrm{W\,m^{-2}}$.

In order to improve the scientific understanding of the microphysical and optical properties of mineral dust, its transport in the atmosphere, and its radiative effect, a group of German research institutes initiated the Saharan Mineral Dust Experiment (SAMUM), funded by the German Research Foundation (Deutsche Forschungsgemeinschaft, DFG). The Sahara is the largest source of mineral-dust aerosol in the world, with an estimated contribution to global dust emissions between 61 % and 77 % (Cakmur *et al.*, 2006, Fig.11). The location of the experiment was close to the dust sources in the south-eastern Moroccan provinces of Ouarzazate and Zagora (Heintzenberg, 2009, see also Section 3.2). This PhD thesis is part of SAMUM (project # 2) and was conducted at the Leibniz Institute for Tropospheric Research (IfT) in Leipzig, Germany, and (from October 2006 on) at the Institute of Atmospheric Physics at Johannes Gutenberg University, Mainz, Germany. Parts of this thesis have been submitted in an article to a special issue on SAMUM to appear in Tellus B (Bierwirth *et al.*, 2009).

[1] See Section 1.2 for the definition of physical quantities. In IPCC, the radiative forcing is referenced to the pre-industrial state of the year 1750.

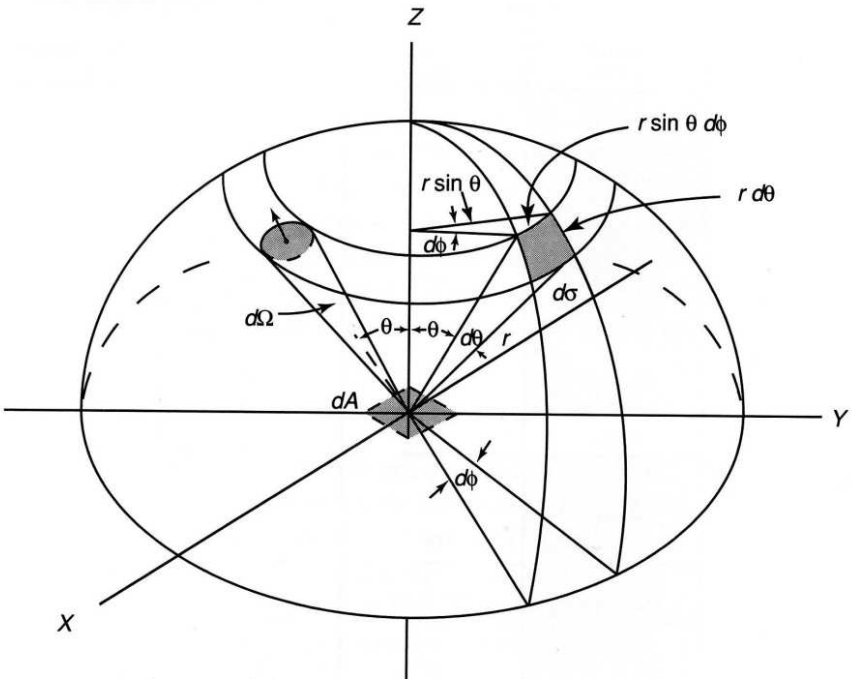

Figure 1.1: The angles that are relevant for the definition of radiance. This figure is adopted from Liou (2002).

The first chapter gives some definitions, motivates research on the radiative effect of desert dust and its coupling with, e.g., surface albedo, and a review of literature relevant in this field. The second chapter describes the work done on the SMART-Albedometer, an instrument for airborne spectral measurements of solar radiation which has been extended in its spectral range in this work. Two experiments — a test campaign and the field experiment within SAMUM — are outlined in Chapter 3. The surface albedo derived from the SAMUM measurements is analysed in Chapter 4. The influence of this surface albedo and its variations on the radiative forcing of Saharan dust is investigated in Chapter 5. Conclusions are summarised in Chapter 6.

1.2 Definitions

1.2.1 Radiative quantities

Consider the energy of an electromagnetic wave which passes through a given area. The differential amount of energy $\mathrm{d}E$ that passes through an element $\mathrm{d}A$ of this area in time $\mathrm{d}t$ in the solid angle $\mathrm{d}\Omega$ in a direction $\vec{\Omega}$ defines the **radiance** I as

$$I(\vec{\Omega}) = \frac{\mathrm{d}E}{\mathrm{d}t\,\mathrm{d}A\,\mathrm{d}\Omega\,\cos\,\theta}\,. \tag{1.1}$$

Here θ is the angle between $\vec{\Omega}$ and the z axis which is oriented perpendicularly to the unit area $\mathrm{d}A$ (see Fig. 1.1 for an illustration).

The unit of the radiance I is W m^{-2} sr^{-1}. If the radiance is related to a wavelength interval $[\lambda, \lambda + \mathrm{d}\lambda]$, the spectral radiance I_λ is defined as follows:

$$I_\lambda(\vec{\Omega}) = \frac{\mathrm{d}E}{\mathrm{d}t\,\mathrm{d}\lambda\,\mathrm{d}A\,\mathrm{d}\Omega\,\cos\,\theta}\,. \tag{1.2}$$

The unit of the spectral radiance I_λ is W m^{-2} sr^{-1} nm^{-1} (assuming that the wavelength λ is given in nm). A spectrally dependent quantity which is expressed in this wavelength-differentiated form is marked by the subscript λ. In this form, the quantity is obtained independent of the irregular wavelength grid of a measurement instrument, e.g. a spectrometer.

The **irradiance** F is defined as the integral of the radiance over the solid angle, weighted with the cosine of the angle of incidence θ on a horizontal surface (θ =0° describes perpendicular incidence). The solid angle element $\mathrm{d}\Omega$ is expressed in terms of the two direction angles θ and φ:

$$d\Omega = \sin\,\theta\,\mathrm{d}\theta\,\mathrm{d}\varphi\,. \tag{1.3}$$

This follows from Fig. 1.1 and the definition of the solid angle $\Omega = \mathrm{d}\sigma/r^2$, $\mathrm{d}\sigma$ being the surface-area element of a sphere of radius r, delimited by the intercept of the surface and the cone that includes the solid angle Ω. It is common practice to consider upwelling ($\uparrow$) and downwelling ($\downarrow$) components separately:

$$\begin{aligned} F^\downarrow &= \int_{\mathrm{LH}} I(\vec{\Omega})\,\cos\,\theta\,\mathrm{d}\Omega \\ &= \int_0^{2\pi}\int_{\pi/2}^{\pi} I(\theta)\,\cos\,\theta\,\sin\,\theta\,\mathrm{d}\theta\,\mathrm{d}\varphi \qquad (1.4) \\ F^\uparrow &= \int_{\mathrm{UH}} I(\vec{\Omega})\,\cos\,\theta\,\mathrm{d}\Omega \\ &= \int_0^{2\pi}\int_0^{\pi/2} I(\theta)\,\cos\,\theta\,\sin\,\theta\,\mathrm{d}\theta\,\mathrm{d}\varphi \qquad (1.5) \end{aligned}$$

where "LH" and "UH" extend over all directions of the lower and upper hemisphere, respectively. With the substitution $\mu = \cos\,\theta$ this simplifies to

$$\begin{aligned} F^\downarrow &= \int_0^{2\pi}\int_{-1}^{0} I(\mu)\,\mu\,\mathrm{d}\mu\,\mathrm{d}\varphi \qquad (1.6) \\ F^\uparrow &= \int_0^{2\pi}\int_0^{1} I(\mu)\,\mu\,\mathrm{d}\mu\,\mathrm{d}\varphi\,. \qquad (1.7) \end{aligned}$$

The unit of the irradiance F is W m^{-2}. The spectral irradiance F_λ is defined with the unit W m^{-2} nm^{-1}.

In the atmosphere, the downwelling irradiance F consists of a **direct** component F_{dir} (which comes from the Sun without scattering in the atmosphere) and a **diffuse** component F_{diff} (which stems from scattering processes with atmospheric molecules and particles, and also includes radiation reflected from the surface back into the atmosphere):

$$F^\downarrow = F^\downarrow_{\mathrm{dir}} + F^\downarrow_{\mathrm{diff}} \tag{1.8}$$

The upwelling irradiance is diffuse only:

$$F^{\uparrow} \equiv F^{\uparrow}_{\text{diff}} \tag{1.9}$$

The difference between the downwelling and the upwelling irradiance is called **net** irradiance. In this work it is generally assumed that the diffuse component is spatially homogeneous. Furthermore, only cloud-free cases are considered.

The **actinic flux density** F^{a} is defined as the unweighted integral of the radiance over the solid angle. It is usually taken over the entire sphere, as its main application is the estimation of the entire radiant energy that can be absorbed by an air molecule:

$$F^{\text{a}} = \int_0^{2\pi} \int_{-1}^{1} I(\mu)\, \mathrm{d}\mu\, \mathrm{d}\varphi \tag{1.10}$$

At any altitude z above the surface, the **albedo** ρ is defined as the ratio of upwelling and downwelling irradiance:

$$\rho(\lambda, z) = \frac{F^{\uparrow}_{\lambda}(z)}{F^{\downarrow}_{\lambda}(z)} \tag{1.11}$$

A case of special interest is the **surface albedo** $\rho_{\text{surf}} = \rho(z = 0)$. This dimensionless function ranging between 0 and 1 indicates how much of the incoming irradiance is reflected. The remainder $(1 - \rho_{\text{surf}})$ is absorbed by the surface.

Similarly, the reflectance R is defined as

$$R(z) = \frac{\pi \cdot I^{\uparrow}(z)}{F^{\downarrow}_{\lambda}(z)}\,. \tag{1.12}$$

The reflectance is therefore identical to the albedo if the upwelling radiance is isotropic, i.e. $\pi \cdot I^{\uparrow} = F^{\uparrow}_{\lambda}$. Otherwise it changes with the direction in which $I^{\uparrow}$ is measured.

At the top of the atmosphere (TOA), the net irradiance $(F^{\downarrow} - F^{\uparrow})$ is zero in a global and temporal mean, if the Earth is in a radiative equilibrium with its surroundings. This equilibrium is usually maintained by a net inflow of energy in the solar spectral range (also called shortwave; 0.3–4 μm) and a net outflow of energy in the terrestrial (or longwave, thermal infrared) spectral range (4–50 μm) of equal magnitude. This equilibrium means that the climate is stable.

However, the energy budget of the Earth-atmosphere system can be changed by a variety of perturbations. For example, aerosol (solid or liquid particles suspended in the air), which scatters and absorbs parts of the solar radiation, may vary in concentration, type, or distribution. The surface properties may change with a re-distribution of vegetation (e.g., deforestation, desertification). Also the solar activity may vary. Cultural processes may modify the concentration of greenhouse gases such as carbon dioxide. All such perturbations (regardless whether their reason is natural or anthropogenic) disturb the radiative equilibrium and may lead to climate change. If a perturbation persists[2], climate stabilises but in a different state than before the perturbation[3].

[2] longer than a few multiples of the time period on which climate is defined

[3] But as any perturbed physical system, climate may perform oscillations before stabilising, and these oscillations may have more or less dramatic consequences for any living being that experiences them.

In order to quantify the radiative effect of such perturbations, the **radiative forcing** ΔF (or Direct Radiative Effect, DRE) is defined as the difference of the net irradiances in the perturbed (subscript "pert") and the non-perturbed (subscript "0") case:

$$\Delta F = \left(F^{\downarrow} - F^{\uparrow}\right)_{\text{pert}} - \left(F^{\downarrow} - F^{\uparrow}\right)_{0} \tag{1.13}$$

With this definition, a positive ΔF at top-of-atmosphere (TOA) describes a warming of the atmosphere by the perturbation, while a negative ΔF describes a cooling. The entire atmospheric radiation spectrum (0.3–50 μm) has to be considered. Nevertheless, the radiative forcing is usually discussed separately for the shortwave spectral range and for the longwave spectral range because different physical processes have to be considered in the two spectral ranges. The sum of the shortwave and the longwave component of the radiative forcing is also called **net** radiative forcing. It is a difference whether a local (or instantaneous) or a global forcing is investigated. The radiative forcing discussed in this work is a local one; otherwise the global distribution mechanisms of Saharan dust would have to be taken into account.

From radiative transfer theory it follows for the TOA radiance that

$$I^{\uparrow}_{\text{TOA}}(\mu,\varphi) = \frac{F_0}{4\mu}\left[\mathcal{S}(\mu,\varphi,\mu_0,\varphi_0) + \frac{4\rho_{\text{surf}}}{1-\overline{s}\cdot\rho_{\text{surf}}}\cdot\mu\mu_0\mathcal{T}(\mu)\mathcal{T}(\mu_0)\right] \tag{1.14}$$

(Chandrasekhar, 1950), where (μ,φ) is the "viewing" direction of the TOA radiance, (μ_0,φ_0) denotes the position of the sun, $\mathcal{S}$ and $\mathcal{T}$ stand for the entire scattering function and the transmissivity of the atmosphere, respectively, while $\overline{s}$ quantifies the fraction of ground-leaving (reflected) radiance that is scattered back to the surface by the atmosphere. F_0 is the extraterrestrial solar irradiance. As a consequence of Eq. 1.14, the TOA radiative forcing, which is the difference of two TOA net irradiances, is a linear function of the surface albedo ρ_{surf} under the condition that $(1-\overline{s}\cdot\rho_{\text{surf}})$ is close to unity. This requirement will be met the better, the darker the surface is and the cleaner the atmosphere is. This relationship in the context of SAMUM data will be looked upon in Section 5.2.

1.2.2 Aerosol properties

When an electromagnetic (EM) wave hits an aerosol particle, parts of the EM energy are absorbed by the particle. Furthermore, a certain portion is scattered into a different direction. The fraction of the energy of the EM wave lost per unit length due to absorption in the material is quantified by the **absorption coefficient** b_{abs}. Likewise, the fraction of energy lost due to scattering is quantified by the **scattering coefficient** b_{sca}. Both b_{abs} and b_{sca} bear the unit m^{-1}. The sum of both is called **extinction coefficient** b_{ext}. An initial irradiance F_0 that travels a distance s through an absorbing and scattering medium is attenuated to

$$F = F_0 \cdot \text{e}^{-b_{\text{ext}}\cdot s} \tag{1.15}$$

(the Law of Beer, Lambert and Bouguer).

The ratio of scattering to extinction is expressed by the **single scattering albedo** $\tilde{\omega}$ defined as:

$$\tilde{\omega} = \frac{b_{\text{sca}}}{b_{\text{ext}}} = \frac{b_{\text{sca}}}{b_{\text{sca}} + b_{\text{abs}}} \,. \tag{1.16}$$

The dimensionless **optical depth** (or optical thickness) τ of a layer of scattering and absorbing material that extends from altitude z_1 to z_2 is defined as the vertical integral of the extinction coefficient of this layer:

$$\tau = \int_{z_1}^{z_2} b_{\text{ext}}(z)\, \mathrm{d}z \,. \tag{1.17}$$

The directional pattern of the scattering of radiation by a particle is described by the phase function $p(\vartheta)$ which describes the probability that photons are scattered in particular directions (that differ from the direction of incidence by the scattering angle ϑ). The phase function may exhibit complex shapes, especially for non-spherical particles such as mineral dust aerosol particles. Within this work, a simpler description of the scattering properties is used — the **asymmetry parameter** g which is defined as

$$g = \int_{4\pi} p(\vartheta)\, \cos(\vartheta)\, \mathrm{d}\vec{\Omega} \,. \tag{1.18}$$

g ranges between -1 and $+1$. The more negative g is, the more radiation is scattered backwards, while high positive values reflect strong forward scattering. Values around zero indicate equal scattering in the backward and in the forward hemisphere.

All these quantities are wavelength-dependent. In the case of the extinction coefficient and consequently of the optical depth, this dependence is parametrised by the Ångström formula

$$\tau(\lambda) = \tau(\lambda = 1\,\mu\text{m}) \cdot \lambda^{-\alpha} = \beta \ \cdot \lambda^{-\alpha}, \,. \tag{1.19}$$

with λ given in μm. As a rule of thumb, the **Ångström exponent** α increases with decreasing size of the aerosol particles.

All quantities in this paragraph are used in this work exclusively for aerosol particles, although they may be applied as well in a more general sense.

1.2.3 Geometric and meteorological quantities

In order to simulate the radiation field in the atmosphere, a number of further parameters have to be known. These include:

- The solar zenith angle (SZA) θ_{s} measures the distance between the Sun and the zenith direction. θ_{s} is usually expressed in degrees. Sunrise and sunset occur at $\theta_{\text{s}} = 90°$ (disregarding refraction effects).
- The vertical profiles of atmospheric temperature, pressure and humidity, measured by radiosondes.

- The concentration profile of trace gases, such as ozone, nitrogen dioxide, and carbon dioxide: Standard profiles (Mid-latitude summer conditions, defined by Anderson *et al.* (1986)) are used that are scaled to the actual pressure and temperature conditions.

- The ozone profile can be scaled to the actual total (columnar) ozone content.

- The elevation of the surface above sea level (a.s.l.).

- The surface temperature determines longwave emissions of the surface.

1.3 Motivation

One of the goals of SAMUM is an estimation of the radiative effect of Saharan dust. This requires calculations with a radiative transfer model, because the radiation field in the atmosphere needs to be reproduced and simulated (a) under the same conditions as during the SAMUM measurements; (b) under the same conditions as during the SAMUM measurements, but without the dust in the model atmosphere; and (c) under slightly modified conditions in order to assess the separate influence of different parameters.

The radiative transfer model is driven by a set of parameters that adequately describe all quantities that are relevant for the radiation field in the given atmosphere. This includes not only scattering and absorption by air molecules and by aerosol particles (SAMUM measurements of these are summarised in Section 3.2.1) but also reflections on the ground surface. The latter are quantified by the surface albedo (Eq. 1.11).

The optical properties of gases and aerosol, as well as the surface albedo are wavelength-dependent, and are regionally variable. So far, however, no measured data of the spectral surface albedo in the Sahara have been available. There are a few spectra of the albedo of desert surfaces published (Fig. 1.2), but most of them cover only a limited spectral range, and none of them is representative for Morocco or the Sahara, nor do they contain information about the regional variability.

Detailed measurements of the surface albedo are possible with the new SMART[4]-Albedometer for almost the entire solar spectral range at high spectral and radiometric resolution. The SMART-Albedometer is operated on an aircraft. This makes it possible to estimate how representative the measurements are for the region in question, and it yields information about the spatial variability of the spectral surface albedo on a regional scale.

The obtained surface-albedo data can then be used as a boundary condition for the radiative transfer calculations. With these, the radiative forcing of Saharan dust can be estimated not only locally, but also in dependence on geographical variations of the characteristics of the underlying surface. Also the spectral behaviour of the radiative forcing can be investigated, which allows conclusions about the influence of different quantities,

[4]Spectral Modular Airborne Radiation Measurement SysTem

not only of the surface albedo but also of aerosol properties.

Another reason why regional measurements of the spectral surface albedo in SAMUM are needed is to provide a constraint for the satellite retrievals of aerosol properties and of surface albedo itself. Such retrievals generally suffer from a poor knowledge about the spectral surface characteristics. This problem is described in more detail in Section 1.4. The measurement flights during SAMUM are collocated with overpasses of satellites from which aerosol properties and surface albedo are retrieved. The spatial and temporal coincidence of these airborne and spaceborne measurements gives a unique opportunity to estimate the consequences of the uncertainties of the assumptions used in these retrievals.

Furthermore, several studies indicate that a high surface albedo of arid areas suppresses rain formation and therefore stabilises deserts (Charney, 1975; Bonfils *et al.*, 2001; Knorr and Schnitzler, 2006). Also for studies in this direction airborne measurements of the surface albedo are useful as a support and validation of large-scale measurements with satellite instruments.

1.3.1 Surface-albedo measurements: State of the art

Measurements of the surface albedo are generally possible by three approaches, each of which has its own advantages and drawbacks.

First, ground-based measurements can be conducted with stationary instruments mounted a few metres above the surface. Such measurements are accurate for this type of surface, but spatial variations of the surface type are hard to assess. Either the instrument has to be moved from one spot to the next (but then temporal variations, like weather, SZA, diurnal plant cycles have to be accounted for), or a network of instruments has to be deployed. In any case the regional representativity of the obtained data is unsure. Therefore, only a limited number of point measurements are performed with this technique.

The second approach is to measure the surface albedo from an aircraft. The surface albedo is derived for certain patches of land beneath the aircraft, the size of which is determined by the field of view of the sensor and by the aircraft altitude above ground. Atmospheric masking of the radiation between the surface and the aircraft has to be taken into account. While this technique allows regional measurements with spatial and temporal flexibility, it is demanding and therefore rarely carried out in practice. Only few instruments are prepared to be mounted on an aircraft, and also the choice of aircraft is limited. If a scanning spectroradiometer is applied, the ground speed of the aircraft is usually a significant drawback, as a single scan lasts a few minutes, so different spectral intervals have been detected mostly over different surfaces.

The third approach uses radiance measurements from satellite instruments to derive the surface albedo. The first and principal problem is the separation of the atmospheric and the surface contributions to the radiance signal at TOA. It is necessary to know the

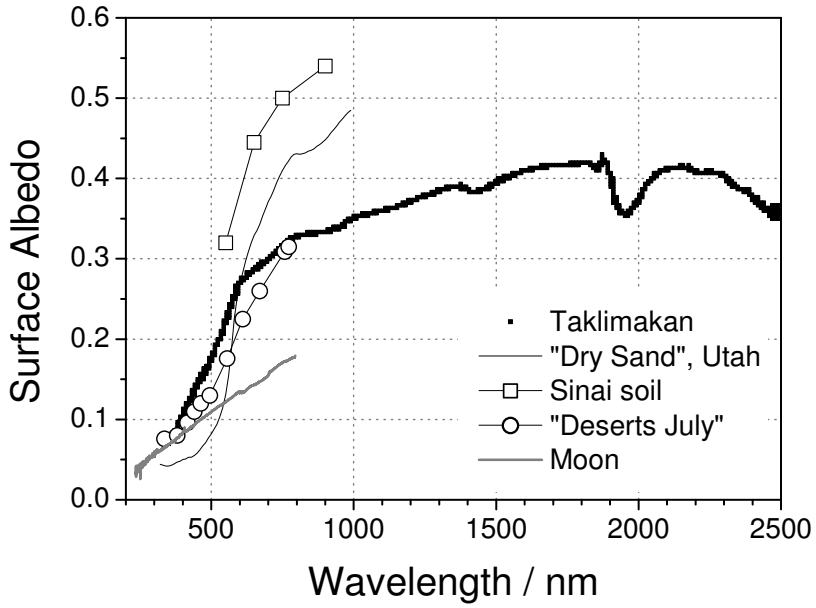

Figure 1.2: Surface-albedo spectra of desert surfaces from literature: From the Taklimakan desert, China (thick line; Aoki et al.*, 2002); the "dry sand" sample from Monument Valley, Utah, USA (Bowker* et al.*, 1985); desert area on Sinai (open squares; Otterman, 1981); the "Deserts (July)" spectrum of Koelemeijer* et al. *(2003) (open circles); and the spectral albedo of the lunar surface (grey line), determined from satellite measurements (GOME; Dobber* et al.*, 1998).*

optical depth of the atmosphere, including aerosol particles, for a derivation of the surface albedo, but for the retrieval of the optical depth it is necessary to estimate the surface albedo. This separation is especially difficult over land where the surface reflection is usually much stronger than the atmospheric signal. One way to tackle this problem is based on the assumption that the temporal variation of the surface albedo is slow compared to that of the atmosphere. Measurements from a certain time period, usually 10–20 days, are evaluated assuming that variations are due to atmospheric variations (e.g., an aerosol outbreak). The major advantage of satellite measurements is their global coverage and their long operation which allows to track long-term variations like land-use changes and deforestation.

A general obstacle in surface-albedo measurements are clouds. Satellite measurements are not possible for places beneath clouds. Aircraft can fly below the clouds, but the cloud cover is almost never horizontally homogeneous or constant in time, which makes it very hard to estimate the downwelling irradiance at the surface as it will certainly differ significantly from the irradiance measured at flight altitude (due to different viewing geometries). Therefore, all SAMUM measurement flights have been scheduled to avoid clouds.

In the following an overview is given over the published surface-albedo data obtained with either of the three approaches.

Ground-based measurements

Ground-based measurements of the spectral surface albedo have been collected in the Taklimakan desert by Aoki *et al.* (2002) for the wavelength range of 350–2500 nm (see Fig. 1.2), and with a scanning spectroradiometer (250–1050 nm) in Antarctica by Wuttke *et al.* (2006). The measurement of the spectral albedo of snow with a set of intermediate-resolution spectrophotometers (300–2500 nm) is reported by Grenfell *et al.* (1994). Kylling *et al.* (2000) retrieved the spectral surface albedo of snow between 320 nm and 500 nm from ground-based global and direct measurements of the downwelling irradiance (enhancement of backscattered radiation over bright surfaces). A similar approach under cloud cover has been followed by Li and Trishchenko (2001) in Oklahoma, USA. Multi-band measurements of bare soil in Sinai in comparison to Landsat data is presented by Otterman (1981) (cf. Fig. 1.2). The influence of a surface tilt on the surface-albedo measurement is investigated by Mannstein (1985) and by Sicart *et al.* (2001). The broadband shortwave surface albedo in western Tibet has been measured to range between 0.18 and 0.28, depending on soil moisture (Wang *et al.*, 2005). That in a rocky desert (gobi) in northern China was determined as 0.21 by Wang *et al.* (1998). The reflective properties of coastal sand dunes were investigated in Israel by Levin *et al.* (2007).

Airborne measurements

An instrument (similar to ours) for airborne irradiance measurements is the Solar Spectral Flux Radiometer (SSFR) which covers the wavelength range from 350 to 2100 nm (Pilewskie *et al.*, 2003). It is applied for the derivation of the surface albedo around Mexico City by Coddington *et al.* (2008). A comparison study with the airborne SSFR and ground-based albedo measurements is presented by Michalsky *et al.* (2003).

Webb *et al.* (2000) applied a scanning spectroradiometer (290–500 nm) at different flight altitudes, investigating the influence of atmospheric masking. Spectral surface-albedo measurements from both SSFR (300–1700 nm) and an earlier version of the SMART-Albedometer (330–995 nm) have been analysed by Wendisch *et al.* (2004), who proposes a method for the elimination of atmospheric masking from the data at flight altitude. Webb *et al.* (2004) present cloud-albedo and surface-albedo measurements with three airborne instruments (the NILU-CUBE at 312 and 340 nm, a scanning spectroradiometer (300–500 nm) and the SMART-Albedometer (290–1000 nm)) in England. A scanning spectroradiometer (400–2400 nm) on a helicopter was applied by Rutan *et al.* (2003) in central North America, reducing the spatial disadvantage of a scanning instrument in airborne measurements.

Bowker *et al.* (1985) have collected 156 reflectance spectra of different surface types and plant species, derived from laboratory, ground-based, and airborne measurements. Their desert-type spectrum "Dry Sand" is shown in Fig. 1.2.

Airborne measurements of the broadband surface albedo have been performed with pyranometers in north-west Africa by Rockwood and Cox (1978), over southern Israel by Ben-Gai *et al.* (1998), and over Nauru in the South Pacific by Matthews *et al.* (2002).

Measurements from satellites

Surface-albedo products derived from spaceborne radiance measurements are available from various instruments; these include:

- the Moderate Resolution Imaging Spectroradiometer (MODIS) (7 wavelength bands 0.47–2.1 μm, see Schaaf *et al.*, 2002);

- the Medium-Resolution Imaging Spectrometer (MERIS) at 15 wavelength bands from 412 nm to 900 nm;

- the Multi-angle Imaging SpectroRadiometer (MISR; 4 wavelengths 446–866 nm in nine viewing angles; see Diner *et al.*, 1998);

- the Advanced Spaceborne Thermal Emission and Reflection Radiometer (ASTER), reflectance at 9 wavelength bands from 520 nm to 2430 nm, also in form of a "spectral library" of typical reflectance spectra, which is available online at `http://speclib.jpl.nasa.gov/`.

Reflectances measured by the Advanced Very High Resolution Radiometer (AVHRR) are used to derive the broadband surface albedo by an empirical linear function (Song and Gao, 1999; Strugnell *et al.*, 2001). Tanskanen and Manninen (2007) derive the ultraviolet surface albedo from reflectivity measurements of the Total Ozone Mapping Spectrometer (TOMS). Koelemeijer *et al.* (2003) have derived a dataset of typical surface albedos (at 11 wavelengths; cf. Fig. 1.2) from TOA radiances measured by the Global Ozone Monitoring Experiment (GOME). From the time series of radiance measurements on the geostationary Meteosat satellite, the angular dependence of the reflectance and subsequently the surface albedo is derived by a method by Pinty *et al.* (2000). The impact of variations of the surface albedo (derived from ASTER data) on the urban radiation balance of Dubai and Abu Dhabi is investigated by Frey *et al.* (2007). Tsvetsinskaya *et al.* (2002) relate the MODIS-derived surface albedo to a soil classification of Northern Africa.

Li *et al.* (2005) model the relationship between the albedo at TOA and at the surface with variations of the SZA, aerosol optical depth, and columnar ozone amount. The impact of surface-albedo inhomogeneities is investigated in 1D and 3D models by Ricchiazzi and Gautier (1998) and by McComiskey *et al.* (2006). Ground-based, airborne (SSFR) and space-borne albedo measurements with MODIS are compared by Trishchenko *et al.* (2004). Surface-albedo datasets from MODIS and the Common Land Model are compared by Zhou *et al.* (2003a) and consequently improvements of the model are suggested. Zhou *et al.* (2003b) found a strong correlation between the shortwave surface albedo from MODIS and the longwave surface emissivity from ASTER. Another comparison of the surface-albedo product of various spaceborne instruments has been performed by Ba *et al.* (2001).

Summary. Each of the three approaches is used in a variety of applications, and the different methods are still under investigation, e.g. in various comparison studies. With regard to SAMUM, however, it must be said that *the* representative desert-type spectrum of surface albedo is not available, especially at the desired spectral resolution and being typical for the particular experiment region of SAMUM. Own measurements with the SMART-Albedometer are therefore indispensable.

1.3.2 The radiative effect of desert dust: Literature review

The optical properties of mineral-dust aerosol depend on the chemical composition and the size distribution. This former is determined by the source region, while the latter changes with transport time. The larger the distance from the source (both vertically and horizontally), the less large particles are contained in the aerosol due to sedimentation. Such a change in the size distribution tends to increase the Ångström and asymmetry parameters. Furthermore, the shape of the aerosol particles is relevant especially for mineral dust. While most simulations of the aerosol optical properties assume a spherical shape of the aerosol particles, dust grains are non-spherical in most cases. Because of the intrinsic variability of dust clouds and because of other possible error sources, e.g. by different assumptions about unknowns, the reported values of the optical properties of mineral dust vary widely. A study by Claquin *et al.* (1998) emphasises the uncertainties that are imposed on estimations of the radiative forcing by uncertainties of the particle size distribution and the surface albedo. Tegen and Lacis (1996) calculated the spectral dependence of the single-scattering albedo $\tilde{\omega}$ and the asymmetry parameter g of aerosol particles of different sizes (effective radii between $0.1\,\mu$m and $9\,\mu$m), but by Mie theory, i.e. disregarding the non-sphericity of the particles. For mineral dust, $\tilde{\omega}$ is generally high (>0.9) in the visible spectrum except for large particles, and drops to low values for higher wavelengths. The steep decrease moves from wavelengths of $3\,\mu$m to $8\,\mu$m and the lowest $\tilde{\omega}$ values increase from 0.0 to 0.5 with increasing particle size.

Sokolik and Toon (1996) compare different optical dust models that yield largely different results for $\tilde{\omega}$ and g, and conclude that "there is no way to decide which of the various models is more appropriate" for an assessment of regional dust effects. Variations between source regions and assumptions, e.g., about refractive indices make a simple, widely applicable dust model impossible. Instead, many regional studies are reported with different assumptions and/or measured data of optical dust properties. In particular, the radiative effect of different types of mineral dust is subject of various studies. An overview of obtained values of dust forcing at TOA and at the surface in recent publications is given in Table 1.1 (global studies) and Table 1.2 (regional studies, mostly using measured optical properties).

The global studies (Table 1.1) agree that the annual and global mean of the *shortwave* radiative forcing at TOA is negative, with values ranging from $-0.92\,\mathrm{W\,m^{-2}}$ to $-0.02\,\mathrm{W\,m^{-2}}$. The only exception is a positive value of $+0.05\,\mathrm{W\,m^{-2}}$ found by Balkanski *et al.* (2007) for a strongly absorbing dust type, S2. However, this modelled dust type had

a much higher imaginary part of the refractive index (i.e., was much stronger absorbing) than actual values from AERONET[5] measurements implied. The less absorbing dust type S1, however, has a refractive index that agrees well the measurement.

The global and annual mean of the *net* radiative forcing at TOA can be both positive or negative. Most values lie between $-1.2\,\mathrm{W\,m^{-2}}$ and $+0.14\,\mathrm{W\,m^{-2}}$. Two cases exhibit a stronger positive value: One ($+0.35\,\mathrm{W\,m^{-2}}$) is due to the exceptional positive shortwave forcing of the strongly absorbing dust type of Balkanski *et al.* (2007). The second one ($+0.39\,\mathrm{W\,m^{-2}}$) stems from a strong longwave contribution. The authors (Myhre and Stordal, 2001) argue that this is due to the global dust distribution used for this case which includes a significant amount of dust higher than 2 km.

The regional studies (Table 1.2) also generally agree that the shortwave radiative forcing of dust at TOA is negative. Only two values are positive; these are due to the use of strongly absorbing minerals in the model. Tegen and Lacis (1996) have used the same refractive indices as Balkanski *et al.* (2007). The net radiative forcing at TOA is mostly negative. The range of values is of course much larger for the regional studies than for global averages.

A correlation between Saharan dust outbreaks on the North Atlantic and a reduced sea-surface temperature was found by Schollaert and Merrill (1998). Hansen *et al.* (1997) state that the radiative forcing of aerosol at the surface shifts from cooling to heating when the single-scattering albedo of the aerosol particles exceeds 0.86, but also that the sign of the forcing still depends on other parameters, such as the altitude of the aerosol layer.

Wang *et al.* (2006) performed model studies of the radiative forcing of an Asian dust plume with respect to the aerosol optical depth, the single-scattering albedo and the asymmetry parameter. When the single-scattering albedo of the dust is increased from 0.80 to 0.86, they find that the TOA net radiative forcing over bright desert surfaces drops from +12 to $+3\,\mathrm{W\,m^{-2}}$, while the surface forcing shifts from below $-80\,\mathrm{W\,m^{-2}}$ to values between -70 and $-80\,\mathrm{W\,m^{-2}}$. Over darker surfaces, however, the TOA net forcing is always negative.

Shell and Somerville (2007b) found that the net radiative forcing of dust at TOA increases with an increase of the asymmetry parameter or the dust particle size (which are related to each other), and with a decrease of the dust single-scattering albedo. Furthermore they state that it tends to be more positive when the dust layer is elevated higher in the atmosphere. They confirm the radiative forcing at the surface to be generally negative and larger in magnitude than the TOA forcing.

[5]The AErosol RObotic NETwork (AERONET) provides quality-assured AOD data from a global network of sun photometers.

Tegen and Lacis (1996) relate dust forcing at the tropopause to particle size and dust-layer height. The forcing is negative for particles smaller than a critical size which depends on the dust-layer height, and positive for larger particles. Forcing is found to be smaller for lower dust layers.

Díaz *et al.* (2001) modeled the local shortwave radiative forcing of mineral dust over land at $-4.5\,\mathrm{W\,m^{-2}}$ with an assumed land surface albedo of 0.22 and averaged over a distribution of AOD values between 0.06 and 0.6. Using the formula of Sokolik and Toon (1996) suggests that the radiative forcing by dust over land may vary between $+5\,\mathrm{W\,m^{-2}}$ and $-24\,\mathrm{W\,m^{-2}}$ depending on the aerosol model (with cloud fraction set to zero and AOD set to 0.321 as measured during SAMUM at $1\,\mu$m on 19 May, 2006).

Balkanski *et al.* (2007) found that the shortwave radiative forcing of dust is positive when the (broadband) surface albedo exceeds 0.2. Aerosol radiative forcing studies (not only dust) by Liu *et al.* (2007) find positive TOA values only over Central Asia and the Arctic and link this to the bright surface albedo of those regions. Hatzianastassiou *et al.* (2004) calculated the global and annual mean of the TOA radiative forcing of all aerosols as $-0.6\,\mathrm{W\,m^{-2}}$, with positive[6] regional values only over desert regions due to a high surface albedo and strong absorption, especially at blue-ultraviolet wavelengths. Stone *et al.* (2007) investigate an Asian-dust event in Alaska over snow-covered surfaces. They found that a variation of 1 % in the surface-albedo input to the model leads to a variation of 5 % in the shortwave forcing at the surface. Lyamani *et al.* (2006) obtained shortwave forcings of a dust event in Spain between -2 and $-12\,\mathrm{W\,m^{-2}}$ in dependence on the solar zenith angle, with strongest forcing occurring at 70°.

The main conclusion of this comparison study is that variations and uncertainties in the optical dust properties, in the spatial and size distribution of the dust, and of the surface albedo lead to a wide range of possible values of radiative forcing, especially when local effects are regarded. Even the sign and the amplitude of the globally and annually averaged radiative forcing, albeit more constrained, depend on assumptions about those quantities. In this context, SAMUM offers a rare opportunity to study the radiative effect of Saharan dust using actual measurements of those quantities.

1.4 Problems of satellite retrievals

Satellite observations are the only possible method to obtain global long-term data of atmospheric or surface properties on a regular basis. Generally, a satellite platform can be designed for two exclusive preferences: high spatial resolution or high temporal resolution. High spatial resolution is achieved by instruments carried on satellites on low orbits (typically, 300 km above ground, just high enough to avoid atmospheric friction).

[6] The authors use a definition that yields forcings of opposite signs, compared to the definition in this work.

Radiative Forcing of Dust: Annual and Global Mean

Authors	TOA SW	TOA LW	TOA net	Surface SW	Surface LW	Surface net	Remarks
Tegen *et al.* (1996)			0.14				
Miller and Tegen (1998)			−0.1			−2.1	Soil dust annually
	−0.45	0.46	0.0	−2.96	0.24	−2.72	Soil dust, summer
Woodward (2001)	−0.16	0.23	0.07	−1.22	0.40	−0.82	
Myhre and Stordal (2001)	−0.02	0.41	0.39				Dust type 1
	−0.53	0.13	−0.40				Dust type 2
Jacobson (2001)			−0.14			−0.85	
Perlwitz *et al.* (2001)	−0.5	0.1	−0.4	−2.1	0.4	−1.7	
Claquin *et al.* (2003)			−1.2				
Myhre *et al.* (2003)			−0.4				Saharan dust
Miller *et al.* (2004)	−0.33	0.15	−0.18	−1.82	0.18	−1.64	
Miller *et al.* (2006)	−0.62	0.23	−0.39	−1.31	0.49	−0.82	
Yoshioka *et al.* (2007)	−0.92	0.31	−0.60	−1.59	1.13	−0.46	
Shell and Somerville (2007a)	−0.73	0.23	−0.49	−1.34	0.37	−0.97	
Balkanski *et al.* (2007)	−0.68	0.29	−0.39			−0.92	Dust type S1
	0.05	0.30	0.35			−1.44	Dust type S2

Table 1.1: Values of global mean radiative forcing of mineral dust from literature for shortwave (SW), longwave (LW), and net (SW+LW) forcing at top of the atmosphere (TOA) and at the surface, in $W\,m^{-2}$. Balkanski dust type S1: 1.5 % hematite internally mixed; S2: Patterson-Volz refractive indices.

Authors	$\tilde{\omega}$	g	TOA SW	TOA LW	TOA net	Surface SW	Surface LW	Surface net	Remarks
Tegen and Lacis (1996)			+15	+5	+20				Regional, annual mean
Tegen *et al.* (1996)					(−2.1) − (+5.5)				Local variations
Hsu *et al.* (2000)				10–25					July av., over land
			−(40 − 50)	3–12	−(28 − 47)				July av., over ocean
Díaz *et al.* (2001)	0.89	0.83	−9.7						Locally, over ocean
			−4.5						Locally, over land
Haywood *et al.* (2001)	0.86	0.67	−(35 − 60)	4.4	−(31 − 56)				Locally, over ocean
Haywood *et al.* (2003)	0.95	0.74	−(44 − 129)						Locally, over ocean
Highwood *et al.* (2003)				6.5			11.5		Locally, over ocean
Meloni *et al.* (2004)	0.96–0.97	0.79–0.80	−(5 − 6)			−(12 − 14)			Locally 14/07/2002
	0.88–0.89	0.81–0.82	−(1 − 2)			−(23 − 25)			Locally 16/07/2002
Wu *et al.* (2005)					0.68			−2.78	E Asia regional, annual mea
Costa *et al.* (2006)	0.75–0.76	0.72–0.80	−40			< −400			Yellow Sea, single ever AOD = 0.4–2.0
Deepshikha *et al.* (2006)	0.82		+4.5			−22.8			Regional, annual mean
	0.97		−0.9			−11.8			Regional, annual mean
Wang *et al.* (2006)	0.88–0.92		−4.3	1.0	−3.3	−10.0	1.6	−8.4	Regional mean
Shell and Somerville (2007b)	0.97	0.8	−0.65		−0.42	−1.3		−0.88	Local instantaneous
Christopher and Jones (2007)			−7.75	1.44	−6.31				Summer mean, Atlant Ocean
Zhu *et al.* (2007)	0.964	0.745	−8.4	4.4	−4.1	−11.2	5.3	−5.9	Spring mean, Yellow Sea
	0.933	0.680	−12.4	5.4	−7.0	−22.4	4.6	−17.8	Summer mean, Arabian Sea
	0.948	0.690	−14.4	8.3	−6.1	−23.0	8.8	−14.2	Summer mean, Saharan Coa
Helmert *et al.* (2007)	0.967		−178	32	−146	−291	77		S Sahara
	0.967		−19	4	−15	−29	9		N Sahara
	0.967		−15	2	−13	−15	3		Europe
	0.901		−146	33	−113	−338	87		S Sahara
	0.901		−17	5	−12	−34	10		N Sahara
	0.901		−12	2	−10	−15	3		Europe

Table 1.2: Values of regional radiative forcing of mineral dust from literature for shortwave (SW), longwave (LW), and net (SW+LW) forcing at top of the atmosphere (TOA) and at the surface, in $W\,m^{-2}$.

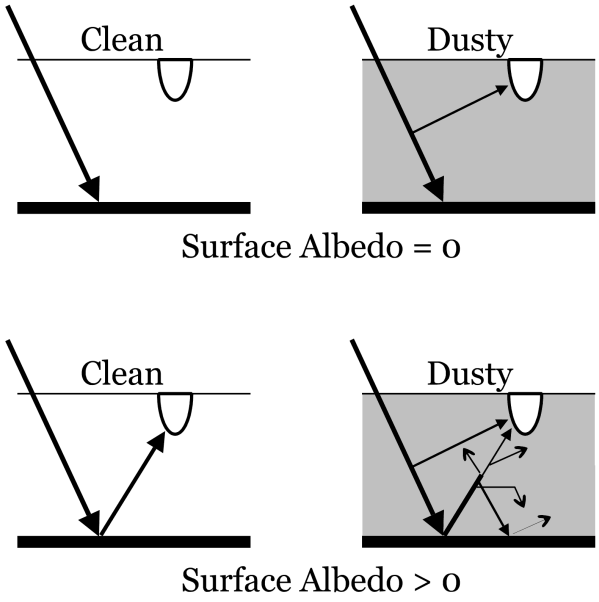

Figure 1.3: Why does the radiative forcing of dust depend on the surface albedo: A downward-looking observer at TOA over a dark surface receives more radiation with dust than without dust because scattered radiation is the only upward component. Over bright surfaces an additional upward component is present also in the clear case, which is attenuated by dust. Radiation scattered back to the surface is again partly absorbed there.

An example is the NASA[7] *Earth Observing System* (EOS) with currently 25 satellite missions. Typically, these satellites are on polar orbits around the Earth, and the same spot on the surface is in view once or twice in a fortnight. Hence, high spatial resolution is achieved at the cost of low temporal resolution. On the other hand, satellites at an orbit of 36,000 km above ground have the same angular velocity as the Earth and therefore are *geostationary*, i.e. they are always above the same surface spot. An example is the Meteosat series of ESA[8]. While instruments on geostationary satellites are able to follow processes at a high temporal resolution, their spatial resolution is low because of the huge distance from the object of observation.

While weather processes are best observed from geostationary satellites (because of their high temporal resolution and their constant and wide field of view), slower processes such as aerosol transport are being followed from low-orbit platforms with global coverage. Apart from the low temporal resolution, space-borne aerosol observations suffer from one major drawback of satellites: The only observed quantity is the radiance at TOA; all other parameters have to be extracted from this quantity. The TOA radiance is the sum of contributions from different sources — scattering from air molecules and aerosol particles, reflections from the surface and from clouds. For aerosol and surface observations, the object of interest is usually lower than clouds, so views that include clouds are not usable and consequently are discarded from the dataset (cloud screening). Scattering processes at air molecules are well understood, so their contribution to the TOA radiance can be calculated easily from the time of the observation and the viewing geometry. However, a

[7]National Aeronautics and Space Administration, USA
[8]European Space Agency

remaining problem is the separation of the aerosol signal from the surface signal. Both are known to change and depend on various parameters not all of which are known. For example, the aerosol optical depth (AOD) depends on the air humidity at the aerosol altitude, which is not directly available. The surface reflectance depends, for instance, on the viewing geometry, on the vegetation cycle, and on ground humidity.

Several approaches are being followed to tackle this unpleasant situation. One of the first is simple: analyse the data only over surfaces known to be dark. Such a surface is the ocean. Therefore, many available aerosol products from satellite observations are not available over the continents.
A more sophisticated approach tries to distinguish the aerosol signal from the surface signal by the assumption that the surface properties change much more slowly than aerosol properties (at a given location). For example, a short-term surface-reflectance database is derived from observations of the Moderate Resolution Imaging Spectroradiometer (MODIS) by coupling all available (i.e., cloud-free) data over a 16-day period (Schaaf *et al.*, 2002). These data are available on request; for the operational retrieval of AOD, however, rather crude assumptions about the surface albedo are applied: the surface reflectance at 470 nm and at 660 nm is derived by a parametrisation of the radiance at 2.1 μm(where aerosol influence is considered to be low), viewing angle, and independently retrieved vegetation information[9] (Levy *et al.*, 2007). Another promising, yet challenging, approach is to use multi-angle information. The Multi-angle Imaging SpectroRadiometer (MISR) measures TOA radiances at nine viewing angles (nadir and 26.1°, 45.6°, 60.0°, and 70.5° in both forward and aftward direction) at four wavelengths: 446 nm, 558 nm, 672 nm, and 866 nm. This multi-angle information improves the analyses of aerosol and surface properties, compared to single-view techniques (Diner *et al.*, 1998). In particular, information about the phase function is obtained which improves the aerosol classification, which in combination with the increased optical path length improves the retrieval of AOD. With an enhanced aerosol retrieval and with multiple viewing angles, the determination of the surface albedo is also improved.

Other AOD retrievals attempt to make use of the fact that atmospheric and aerosol scattering has a stronger polarising effect than surface reflection (Deuzé *et al.*, 2001) or that surface reflectance is generally low in the blue spectral region (von Hoyningen-Huene *et al.*, 2003; Hsu *et al.*, 2006).

Despite this multitude of approaches, the AOD retrieval from satellite data is still not satisfactory. Kokhanovsky *et al.* (2007) performed an intercomparison between the AOD retrieval of 10 different algorithms that use data from 6 satellite instruments for a cloudless scene over Central Europe. The different results show significant variations of AOD between each other and in comparison to AERONET data. The authors give a number of reasons for the differences: instrumental effects, such as calibration differences

[9] Until MODIS algorithm version C004, in use until 2005, merely a linear relationship between the surface reflectance at 2100 nm, 660 nm and 470 nm was assumed.

and different information content; horizontal inhomogeneity effects; and, most important, different *a priori* assumptions in the retrieval algorithms. Those assumptions concern aerosol properties (shape, size distribution, refractive indices, spectral optical properties), trace gases, and the surface reflectance. Veefkind *et al.* (2000) found that "the assumed surface albedo should be within 0.01 of the true value to ensure that the retrieved AOD is within 0.1 of the true value".

In order to compare the sensitivity of the TOA radiance, as measured by satellite instruments, to different aerosol and surface parameters, the TOA radiance has been calculated by a radiative transfer model (see next section). Different scenarios have been assumed that reflect the situation during the SAMUM experiment. The measured values of the surface albedo and of the dust single-scattering albedo, asymmetry parameter, and AOD have been applied in the model. The calculation has then been repeated with variations of each parameter, and the resulting TOA radiances have been compared to each other. As a measure of the influence of each parameter ξ on the TOA radiance, the *response ratio* RR is introduced as

$$RR_\xi = \frac{\text{Variation in TOA radiance}}{\text{Variation of input parameter } \xi} = \frac{\partial I^{\uparrow\, TOA}}{\partial \xi} \,. \tag{1.20}$$

For example, a response ratio for the surface albedo of 0.4 means that a surface-albedo change of $x\,\%$ leads to a change in TOA radiance of $0.4 \cdot x\,\%$.
The following values have been used as input for modelling:

- Single-Scattering Albedo $\tilde{\omega}$: 0.87, **0.94**, 0.98
- Asymmetry parameter g: 0.63, **0.68**, 0.75
- AOD: 0.1, **0.4**, 0.7, 1.1
- Surface Albedo: **Hamada-type spectrum**, Hamada $\pm 10\,\%$, Hamada $\pm 50\,\%$.

The boldface value is the default value (typical for SAMUM) for each parameter. Calculations have been performed with variations of one parameter, with all other parameters at their default values. In some cases this has been repeated for all alternative values of a second parameter (e.g. variations of the surface albedo for different values of AOD).
All calculations have been performed for five different viewing geometries (satellite positions) — due south and 60° east of the southern direction; and at zenith angles of 0°, 30° and 70°. 70° has been chosen because this is the maximum viewing angle of the satellite instrument MISR. The location of the sun was 60° east of the southern direction and at a zenith angle of 20° in all calculations.

Results: Of all calculations, the two extreme cases of viewing geometry (satellite zenith angles of 0° and 70° are shown in Figs. 1.4–1.6. Each figure has two panels, the left one for nadir view (satellite zenith angle of 0°) and the right one for maximum slant view (satellite zenith angle of 70°). Shown are the spectral response ratios for the aerosol single-scattering albedo (Fig. 1.4), the surface albedo (Fig. 1.5), both for several values of

AOD. The spectral response ratio for the AOD (above surfaces of three levels of brightness, but the same spectral behaviour) is shown in Fig. 1.6. In most cases, the response ratio for one parameter depends only little on the *absolute* value of this parameter. This is not true, however, for the AOD, and also for $\tilde{\omega}$ in case of high AOD values. Whenever the absolute value is influential, the figures show more than one curve with the same symbol, each curve standing for one of the absolute values.

Fig. 1.4 shows that the aerosol single-scattering albedo $\tilde{\omega}$ has the largest influence on the TOA radiance. At an AOD of 1.1, its influence strongly depends also on the absolute value of $\tilde{\omega}$. Under the extremest conditions in this survey, variations in $\tilde{\omega}$ lead to variations in TOA radiance almost four times as large. It follows that the correct choice of the aerosol model (assumption about the optical parameters) must be essential for a satellite retrieval of aerosol properties[10]. The influence of $\tilde{\omega}$ is strongest in the mid-visible around 600 nm. In Fig. 1.5 we see that the response ratio for the surface albedo increases throughout the visible spectral range and reaches unity at about 700 nm where it remains also for longer wavelengths. It is slightly reduced when the AOD is high, and this reduction is much stronger at high viewing angles because of the increased optical path through the aerosol layer.
Fig. 1.6 shows that the AOD has only little influence on the TOA radiance, compared to that of the single-scattering albedo and that of the surface albedo. The response ratio does not exceed 0.2 for nadir view, and even at at large viewing angles in just increases to 0.3, notwithstanding the threefold optical path through the aerosol layer. AOD is the primary quantity retrieved from satellite observations. It is therefore clear that uncertainties in the surface albedo and in $\tilde{\omega}$ (i.e. in the choice of the aerosol model) are a major problem in such a retrieval.

[10]Many satellite retrieval algorithms, such as that of MISR, have a certain choice of aerosol models which are used to model TOA radiances in look-up tables for the corresponding viewing geometry. Those modelled TOA radiances are compared to the measurement, and the aerosol model with the best fit is then used for the retrieval of the AOD.

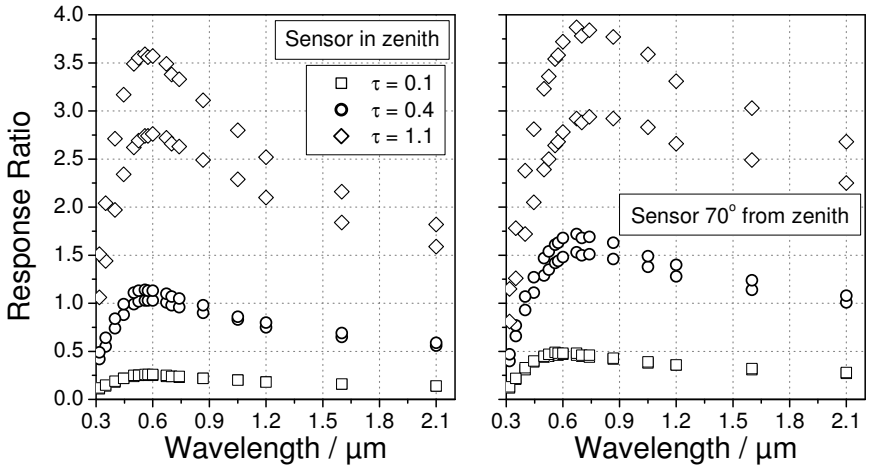

Figure 1.4: Calculated influence of the aerosol single-scattering albedo on the TOA radiance.

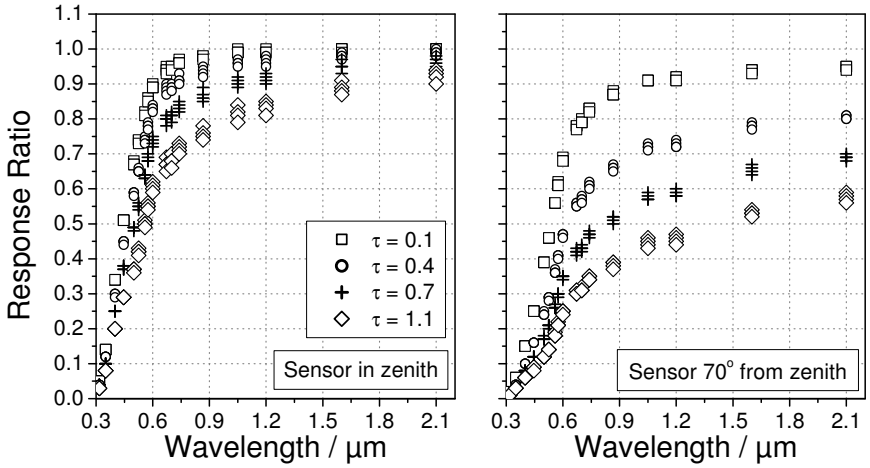

Figure 1.5: Calculated influence of the surface albedo on the TOA radiance.

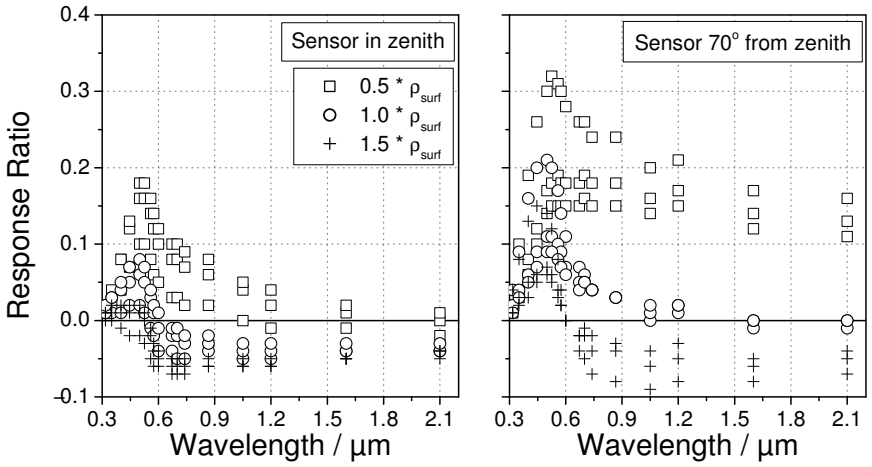

Figure 1.6: Calculated influence of the AOD on the TOA radiance.

2 The SMART-Albedometer

2.1 Overview

The Leibniz Institute for Tropospheric Research (IfT) in Leipzig, Germany, has developed a unique instrument for airborne radiation measurements, the *S*pectral *M*odular *A*irborne *R*adiation Measurement Sys*T*em (SMART)-Albedometer (Wendisch *et al.*, 2001) in collaboration with *enviscope GmbH*, a company in Frankfurt am Main, Germany. The experimental work described in this thesis is based on the SMART-Albedometer. Within this work, the wavelength range of the SMART-Albedometer has been expanded to the near infrared.

A key feature of the SMART-Albedometer is the horizontal stabilisation of the optical inlets during flight. A proper distinction of the radiation from the upper hemisphere (which includes the Sun) from the radiation from the lower hemisphere is crucial for studies of atmospheric radiation. The uncertainty due to any horizontal misalignment of the sensors is significant and often not sufficiently taken into account, as described by Wendisch *et al.* (2001). It is shown that even a slight horizontal misalignment of 1° gives rise to an irradiance uncertainty of more than 30 % (for a solar zenith angle of 70°). For an irradiance uncertainty of less than 1 % for solar zenith angles of up to 70°, proper levelling must be guaranteed to within 0.2°. These technical requirements are met by the horizontal stabilisation system of the SMART-Albedometer. A second system called STRAP (Stabilized Radiometer Platform) with similar properties has been developed in 2006 at the Naval Research Laboratory, Monterey (CA), USA (Bucholtz *et al.*, 2007, submitted).

2.2 Working principle

The SMART-Albedometer is a spectroradiometric system designed for the airborne spectral measurement of various radiometric quantities in the solar spectral range. Measurements can be performed either in upward or in downward direction, or both. Measurement in both directions is the default setup, hence the name *albedometer*, as the albedo is defined as the ratio of upwelling and downwelling radiation.

The SMART-Albedometer consists of the following four components: (1) The optical inlets, and the fibre optics, (2) the horizontal stabilisation system, (3) the spectrometers, and (4) the computer control system. A sketch of the current system is shown later in Fig. 2.3.

(1) The SMART-Albedometer can be operated with different kinds of optical inlets. The choice of the optical inlet determines which radiometric quantity is measured. In its current setup (as of 2007), inlets for the measurement of irradiance, radiance, and actinic flux density are available. All measurements presented in this work are irradiance measurements. The corresponding optical inlets are described in Section 2.5.

Actinic flux density is measured by isotropic inlets, manufactured by Meteorologie Consult GmbH, Königstein, Germany, based on frosted quartz domes. They have been described by Jäkel *et al.* (2005). Inlets for the measurement of radiances have been developed by A. Ehrlich, based on a Zeiss collimator lens with a viewing angle of 1.5°.

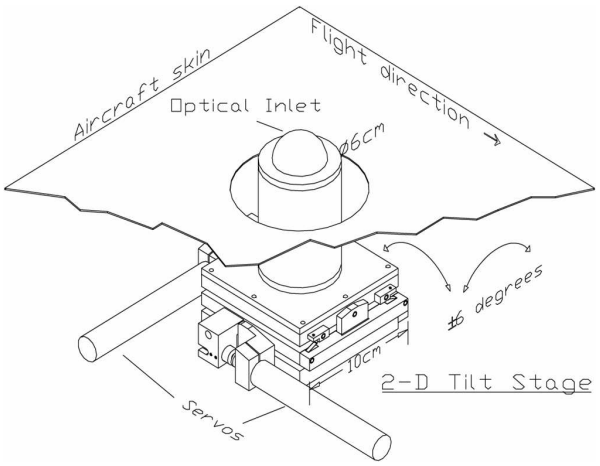

Figure 2.1: Sketch of the horizontal stabilisation platform for levelling the optical inlets on an aircraft. This image is from Wendisch et al. *(2001).*

(2) The horizontal stabilisation system has been jointly built by IfT and *envis-cope GmbH* and is described in detail by Wendisch *et al.* (2001). It is a platform that stabilises the optical inlets when they are mounted on an aircraft and keeps track of the aircraft attitude[1]. The inlets are horizontally aligned by servo motors (see Fig. 2.1) that are controlled by LabVIEW and MS-DOS software. This software gets the attitude data from an Artificial Horizon System (AHS) that determines the aircraft attitude. The temporal drift of the AHS is corrected by the signal received from satellites of the *Global Positioning System* (GPS) by two GPS antennas on the front and rear roof of the aircraft.

Horizontal stabilisation is achieved with an accuracy of better than ±0.2° over a range of pitch and roll angles of up to ±6°. The response is fast enough even for turbulent conditions (response time 43 ms, maximum angular velocity $3^\circ\,s^{-1}$).

(3) The optical signal is directed by optical fibres from the inlets into the spectrometers. Inside, the photons are spectrally dispersed by a grating and detected by a single-line photodiode array (PDA). The electric signal from the photodiodes is accumulated by an integrating circuit[2] over a user-adjustable period of time, called *integration time*. The integrated signal is amplified, digitised and stored in the front-end electronics (FEE) which transfers the data to the computer.

Each spectrometer can be used for any radiometric quantity[3], but the choice of the spectrometer determines the spectral range that can be measured. In order to cover the entire solar spectral range, two spectrometers are required: One for the irradiance in the visible part of the solar spectrum and a little more, namely 290 nm to 1000 nm; this

[1] Attitude: inclination of the aircraft fuselage with respect to the two main axes, usually expressed as *roll* and *pitch* angles.

[2] An operational amplifier in parallel to a capacitor

[3] Actually, actinic flux density investigations need a better UV sensitivity. Spectrometers that use CCD (Charge-Coupling Device) sensors are then better suited than spectrometers based on PDA sensors.

Name	Type	Spectral Range (nm)	Number of pixels	Resolution FWHM (nm)	Measured Quantity
VIS	MCS 55 UV/VIS	290–1000	1024	2–3	Irradiance (↑↓)
NIR	PGS NIR 2μ2	900–2200	256	9–16	Irradiance (↑↓)
AFDM	MCS 55 UV/VIS	280–700	512	2–3	Actinic Flux Density (↑↓)

Table 2.1: The three types of spectrometers of the SMART-Albedometer (during SAMUM 2006). A pair of each type is used in order to measure both upwelling and downwelling radiation (↑↓).

spectral range and the corresponding spectrometers are referred to as "VIS". A second spectrometer is needed to cover the near-infrared spectral range (1000 nm to 2200 nm), this is referred to as "NIR". Furthermore, the Actinic Flux Density Meter (AFDM) is used for the measurement of actinic flux densities in the spectral range from 290 nm to 700 nm.

Altogether, the SMART-Albedometer as used in this work comprised six spectrometers — two VIS, two NIR, and two AFDM (cf. Table 2.1). A pair of each is required for the measurement of both upwelling and downwelling radiation.

(4) Personal computers are used to control the spectrometers and also to read the digital signal from the FEE unit of the spectrometers and to store the data in ASCII files on hard disk. A computer is also required to control the horizontal stabilisation platform.

2.3 Extending the wavelength range

In this work, the SMART-Albedometer has been extended in its wavelength range. Originally it was designed for the spectral range between 290 nm and 1000 nm, i.e. the visible spectrum and a part of the near-infrared (NIR) range. The solar spectrum, however, contains significant radiation up to 3000 nm, and optical properties of aerosol and cloud particles and of the surface accordingly are relevant at such wavelengths. Furthermore, remote sensing of clouds (especially of cloud-particle phase) require coverage of the spectral region around 2.1μm (e.g., Sun and Shine, 1994). Therefore it was necessary to extend the spectral range of the SMART-Albedometer. Spectrometers that are compatible to the previous system have become available since 2005 for the spectral range from 900 nm to 2200 nm[4]. Calculations have shown that the resulting range from 290 nm to 2200 nm contains 96–99 % of the entire solar irradiance (downwelling irradiance at bottom-of-atmosphere; the actual value varies in dependence on humidity and aerosol optical depth, see Fig. 2.2). Hence it has been achieved to cover almost the entire solar spectrum with two spectrometers.

(1) New optical inlets for irradiance measurements have been purchased that exhibit an improved transmittance and angular sensitivity than the old set – especially for NIR wavelengths of up to 2.2 μm. The optical inlets have been purchased from the Bay Area Environmental Research Institute (BAERI), Sonoma, California (USA). They are based on an integrating sphere cut into a Spectralon® body. A conical baffle avoids direct illu-

[4]Spectrometers covering the spectral range from 900 nm to 1700 nm have been available earlier.

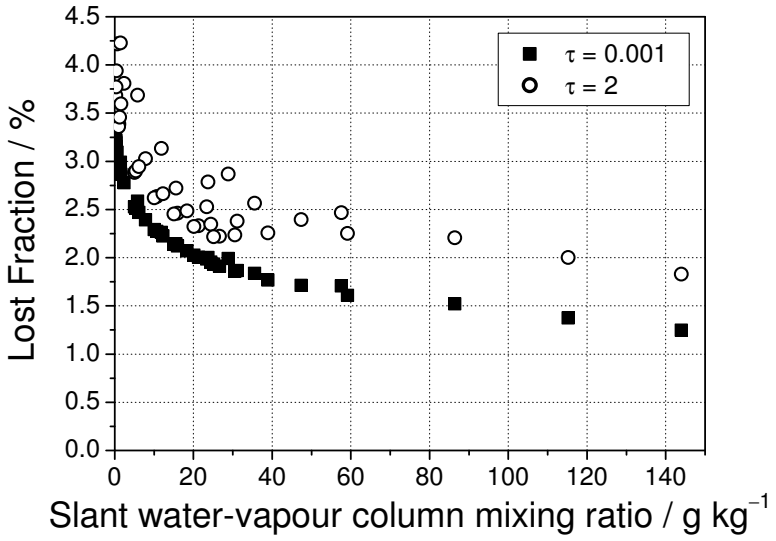

Figure 2.2: Fraction of the unobserved ("lost") irradiance spectrum when only the wavelength interval from 290 nm to 2200 nm is measured, instead of the full solar spectrum (assumed to range from 250 nm to 6000 nm). The lost fraction depends on both aerosol optical depth τ and on the water-vapour content of the atmospheric column (slant in direction of the Sun).

mination of the optical interface at the bottom of the sphere. The geometrical set-up has been designed to obtain an integration that is weighted with the cosine of the angle of incidence, in order to follow the definition of irradiance (Crowther, 1997, see Fig. 2.20). A characterisation of these inlets as well as an estimation of their field of view is outlined in Subsection 2.5.

Also new optical fibres have been obtained because the glass normally used has strong absorption features between 1 μm and 2 μm. Fibres have to be specially designed for the NIR wavelength range in order to avoid those absorption ranges. The new fibres are bundles that split up the signal from one sensor and leads it into a VIS spectrometer (using standard fibres) and into a NIR spectrometer (using NIR-specific fibres with better transmittivity for such wavelengths).

The *dark signal* of a spectrometer is the result of the dark current, a thermally induced current through each of the photodiodes which adds to the photocurrent induced by incoming photons. It is determined by the material characteristics of the semiconducting InGaAs layer in the photodiode, such as the In/Ga ratio and the concentration of impurities (dopants)[5]. The dark current increases with the photodiode temperature,

[5]Photodiodes consist of a *p*-*n* junction in a semiconducting material, i.e. two adjacent zones in the material that are positively and negatively doped, respectively. To this diode a reverse bias voltage is applied, and in consequence a depletion region is established between the *p* and the *n* zone. Whenever a photon with sufficient energy hits this depletion zone, an electron-hole pair is generated and leads to a measurable photocurrent. The minimum energy for the photon to be detected depends on the bandgap energy of the material. This results in a choice of materials for applications in different

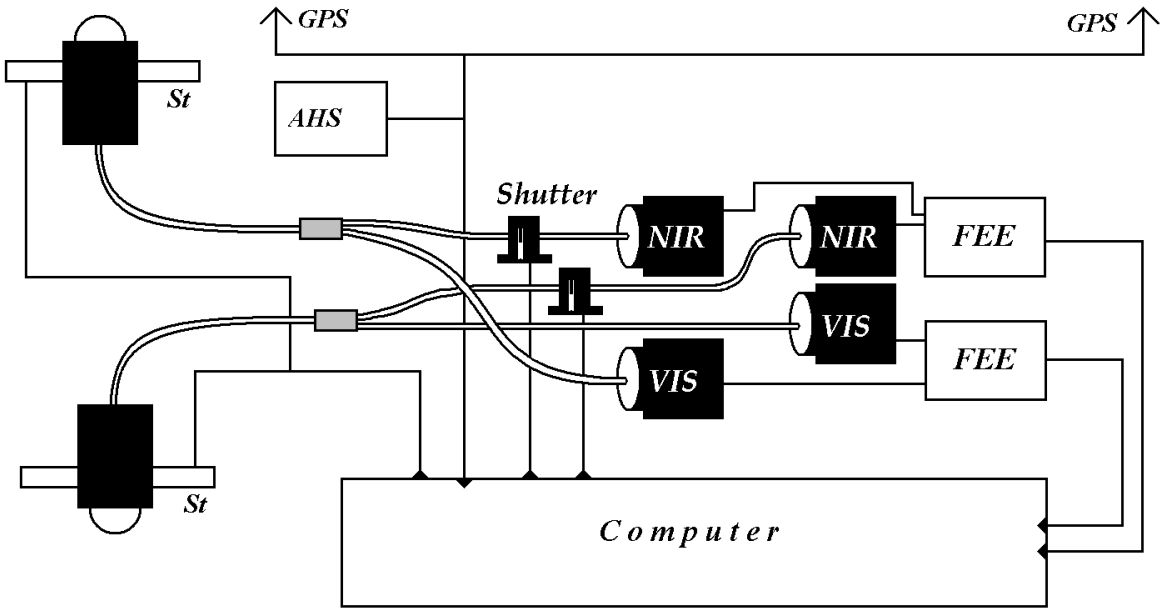

Figure 2.3: A sketch of a setup to measure irradiance with the SMART-Albedometer. From the optical inlets (left) the signal passes through a bifurcated optical fibre, one end of which leads to the NIR spectrometer (upper branch), while the other end leads to the VIS spectrometer (lower branch). A shutter is included in the NIR path for measurements of the dark signal of the NIR spectrometer. The measured signals are processed by the Front-End Electronics (FEE) and transferred to the data-acquisition port of the computer. The position and attitude data from the two GPS antennas and the Artificial Horizon System (AHS) are used to drive the horizontal stabilisation platforms (marked "St") on which the optical inlets are mounted. Power lines and the Actinic Flux Density Meter (AFDM) are omitted from this sketch.

and the dark signal also increases with the integration time. Due to electronic noise and possible temperature fluctuations it is not constant with time and therefore has to be (in principle) measured simultaneously to allow detection of the radiation signal. For the VIS and AFDM spectrometer this measurement is not done during flight. Instead, the dark signal is estimated from the pixels for wavelengths below 280 nm, as in that spectral range no natural radiation is encountered and the net signal can be assumed to be zero. The total signal level of the lowest 100 pixels thus allows an estimation of the current dark-signal level that is later subtracted from the measured spectrum. For the spectral range of the NIR spectrometers, however, this approach is not feasible, as it cannot be in general expected that at any wavelength of this range there is no natural radiation. Therefore, a shutter (OceanOptics Inc. Inline-TTL Shutter, purchased from OPTOcon GmbH, Dresden) has been included into the NIR optical path in order to measure the NIR dark signal (cf. Fig. 2.3). The shutter is plugged between the optical fibres from

wavelength ranges of detection. The dark current also grows with the bias voltage. For this reason, in the PGS *pin* photodiodes are applied: An intrinsic, i.e. undoped layer is introduced to obtain a *p-i-n* structure. The intrinsic layer takes the role of the depletion region which is hence present without a reverse bias voltage. The photodiode can therefore be operated with a much lower bias voltage, resulting in a reduced dark current. A small reverse voltage is still needed in order to accelerate the charge couples generated by the photons, i.e. to drive the photocurrent.

the spectrometer and from the sensor head, and provides a mechanical closure of the optical path. It is controlled by the spectrometer control software which synchronises the spectral measurements and the mechanical state of the shutter. The interval of the dark measurements can be chosen by the user, and the dark signal is stored and subtracted from all subsequent measurements, until a new dark measurement is started. During SAMUM, three dark scans have been inserted after each 11th radiation scan, that is once in 5–10 s (depending on the integration time). The shutter required an additional 12 V power supply that was implemented into the spectrometer system electronics.

(2) The horizontal stabilisation system has not been modified.

(3) The spectral range of the SMART-Albedometer has been extended from 290–1000 nm to 290–2200 nm. To this purpose, a pair of PGS 2.2 spectrometers has been purchased from Zeiss[6], Jena, Germany. These are *P*lain *G*rating *S*pectrometers with an InGaAs (Indium-Gallium Arsenide) photodiode detector array of 256 pixels. InGaAs detectors for the spectral range up to 2200 nm with reasonably low dark signals have become available only in 2006, and still require on-board Peltier cooling of the photodiodes to temperatures between −20 °C and −40 °C in order to reduce the dark signal.

All six spectrometers contained in the SMART-Albedometer have been mounted into an insulated 19" housing. See Fig. 2.4 for a illustration of the system and its components. The housing is equipped with fans and an additional Peltier element to cool its interior when operating in a warm environment. All spectrometers are certified up to temperatures of 40 °C but must not be stored above 60 °C as higher temperatures would melt the glue of the grating. Low temperatures are also important to keep the dark signal (especially that of the NIR spectrometers) as low as possible.

(4) Each pair of spectrometers (VIS irradiance, NIR irradiance, and actinic flux density) is controlled by a computer. Each computer runs a LabVIEW programme (provided by *enviscope GmbH*) and stores the measured raw data. The LabVIEW front-end panel allows control of the spectrometer parameters (integration time, number of averaged spectra) and of the shutter (open/closed/automatic mode, number of dark and radiation scans) and depicts a real-time plot of the measured data on the screen for diagnostic purposes. The data are stored on Flash disks as ASCII files that for each scan contain the time, the 16-bit-encoded signal of each pixel (−32768 to +32767), the integration time, the number of averaged scans (usually equal to 1), the shutter status, an error code, and in case of the NIR spectra also the dark signal of each pixel.

2.4 The NIR spectrometers

2.4.1 MMS version

The Monolithic Miniature Spectrometer (MMS) was the first type of NIR spectrometers released in 2004 for the spectral range up to 2.2 μm. Their performance was not satisfactory in series of tests and at a test campaign conducted at Brandis airfield (near Leipzig). Eventually, the MMS system was replaced by the PGS system (see next subsection) for

[6]Then Carl Zeiss Jena GmbH, Department Spektralsensorik, now Carl Zeiss MicroImaging GmbH.

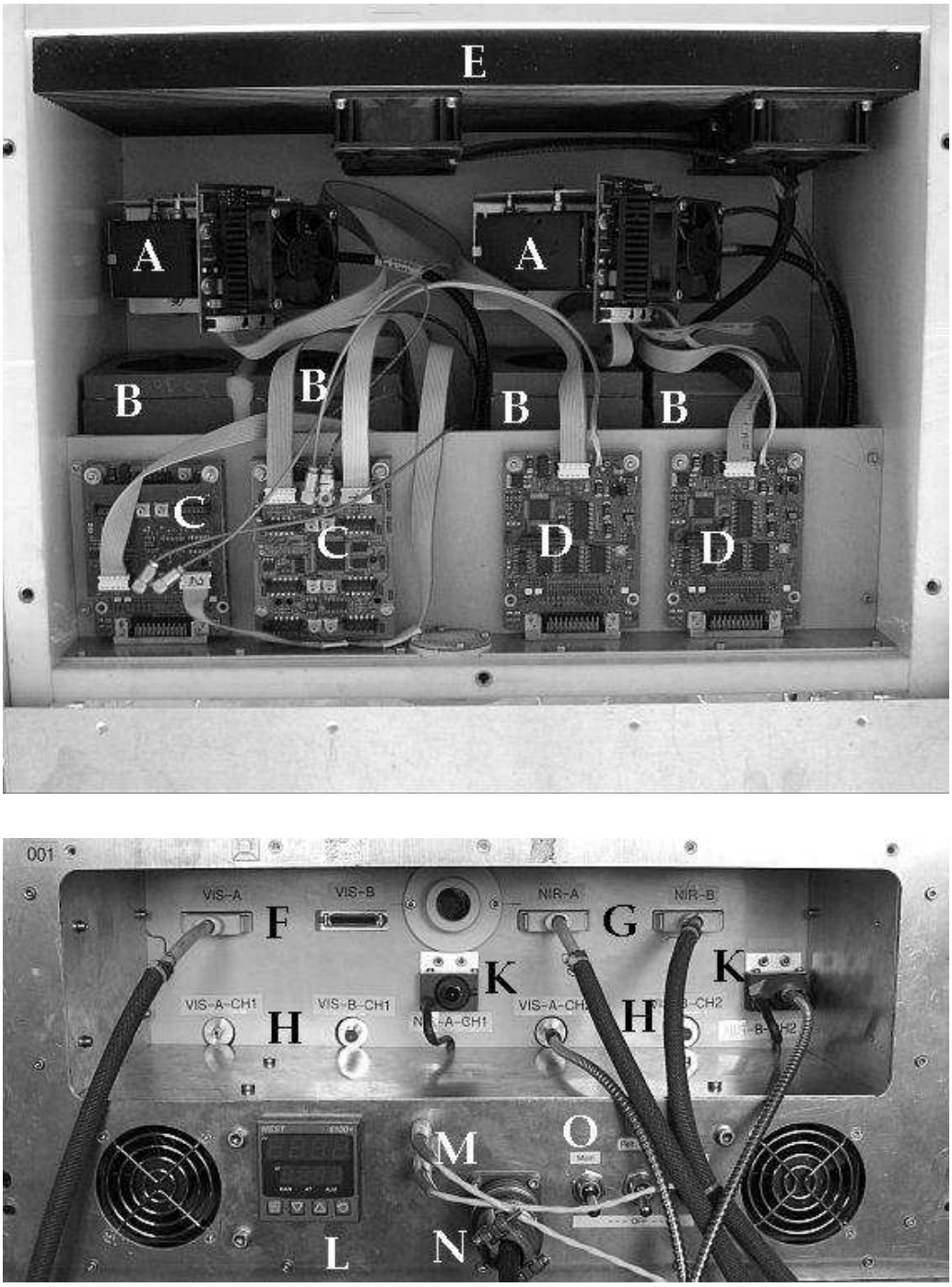

Figure 2.4: The SMART-Albedometer in its 19" housing. Upper panel: interior view, lower panel: the front panel. A: The PGS NIR spectrometers. B: MCS spectrometers for VIS irradiance and actinic flux density. C: Front-end electronics for VIS irradiance and actinic flux density (multiplexed, 2 spectrometers per card). D: Front-end electronics for NIR. E: Additional Peltier element for cooling of the interior. F: Data connection to the PC, for VIS irradiance and actinic flux density data. G: Data connection for NIR. H: SMA connectors for fibres from the optical inlets for VIS irradiance and actinic flux density. K: SMA connectors of the shutters for fibres from the optical inlets, for NIR. L: Temperature control panel for the Peltier (E). M: Shutter control connectors. N: 24 V power supply. O: Three power switches (mains, PGS Peltier, housing Peltier).

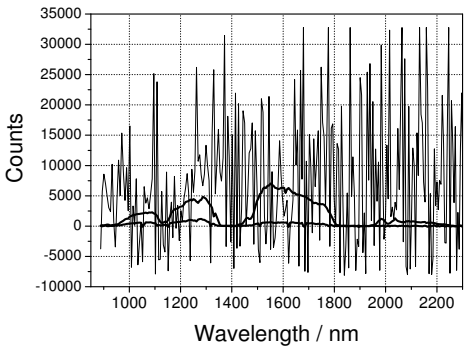

Figure 2.5: In the order of decreasing amplitude: The dark signal of the MMS spectrometer, the net downwelling irradiance, and the net upwelling irradiance spectra as measured during the Brandis test campaign. The fact that the dark signal reaches amplitudes much larger than that of the scientific signal is a severe limitation with respect to both sensitivity and data quality (noise).

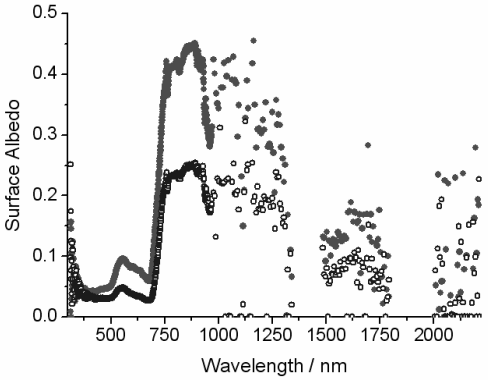

Figure 2.6: Two examples of the spectral surface albedo as measured during the Brandis test campaign. While a smooth albedo spectrum is obtained from the VIS spectrometer up to 1 μm, the albedo values derived from the NIR measurement with the MMS spectrometers are very noisy.

the SAMUM field campaign. Nevertheless, the tests of the MMS are described in this section as it shows some of the peculiarities that a poor dark signal-behaviour can possess.

The main drawback of the MMS is the magnitude and the temporal behaviour of the dark signal. The dark signal of the MMS is huge compared to the optical signal. Fig. 2.5 clearly shows that (1) the photodiodes are prone to saturation only because of the dark signal, and (2) any small fluctuation of the dark signal has a much stronger impact on the net signal. (1) limits the dynamic range of the spectrometer, as the integration time has to be chosen carefully to avoid dark-signal saturation. For conditions with low levels of radiation (such as clouds, winter, Arctic, dawn and dusk) it is then not possible to choose high integration times for good detection of the weak radiation. (2) is a major source of noise in the net signal, especially when measuring the weaker upwelling irradiance. This leads to a noisy surface-albedo spectrum in the NIR, cf. Fig. 2.6.

Under the condition that useful information can be measured with the range of integration times available (i.e., under bright conditions), the dark signal would not be a severe limitation *if it were constant with time*. However, the dark signal shows significant fluctuations. The dark signal of pixel n can be parametrised by a formula like

$$y_n(t) = y_0^{(n)}(t_{\mathrm{int}}) + u_n(t) + u_0(t) \tag{2.1}$$

where $y_0^{(n)}(t_{\mathrm{int}})$ describes the (almost linear) dependence on the integration time t_{int}, $u_n(t)$ are the individual fluctuations of the dark signal of pixel n, and $u_0(t)$ is the DC offset of the entire spectrum. This behaviour is shown in Fig.2.7, and Fig. 2.8 shows how this dark signal influences the measurement. In the spectra measured with NIR #1, the variations of $u_0(t)$ are obvious in the water-vapour absorption bands (at 1400 nm and at 1900 nm)

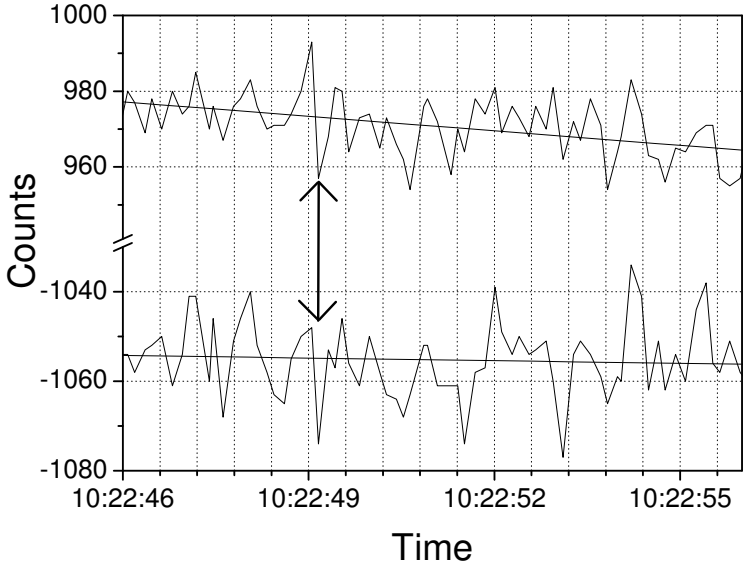

Figure 2.7: The temporal behaviour of the dark signal of two MMS pixels. Individual fluctuations $u_n(t)$ are obvious between any two scans, but also as a long-term drift, indicated by the different slope of a linear fits. Also some common fluctuations $u_0(t)$ (example marked by arrow) can be seen.

where the net signal should be zero. The net signal is calculated as the difference between two measurements, one with the optical inlet open and one with the inlet closed. As there is a time difference between these two measurements, the measured dark signal is not the same as the actual "dark" contribution to the measurement with the open inlet. Therefore, the offset of the net spectrum reflects the temporal change of the dark signal.

The spectra of NIR #2 on the right panel of Fig. 2.8 tell us that (1) the same illumination yields lower net signals; (2) the spectral sensitivity is different to that of NIR #1, (3) the DC offset seems more stable than in NIR #1, and (4) the dark signal is stronger than in NIR #1, leading to a much noisier signal, especially in the upper low-signal part of the spectrum. Later tests revealed that the jumps of the DC offset $u_0(t)$ are induced by voltage fluctuations in the power supply of the Peltier elements of the spectrometer. For the airborne configuration, a more stable power supply was used and the DC offset was no longer observed.

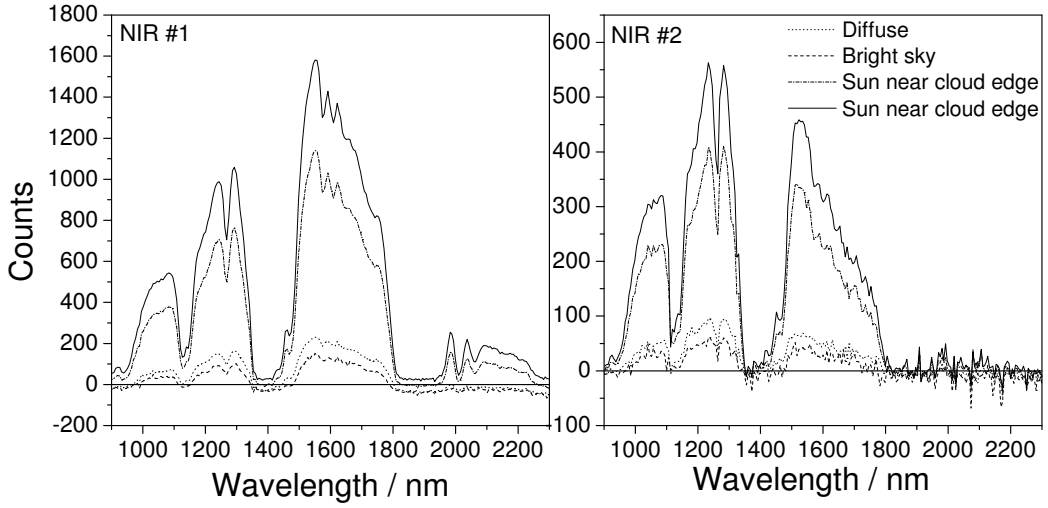

Figure 2.8: Solar spectrum (raw signal, dark signal subtracted) measured on a day with broken clouds, measured with both MMS NIR spectrometers. The four spectra have been measured at different cloud constellations: Diffuse *was taken with the sun completely covered;* Bright sky *with the sun behind a cloud edge with brightly illuminated clouds nearby that would cast shadows. The two* Sun near cloud edge *plots show the spectrum of diffuse plus direct solar radiation with clouds moving fast next to the solar disk. Integration time* $t_{\mathrm{int}} = 20\,\mathrm{ms}$. *Measured at IfT, 6 January, 2005.*

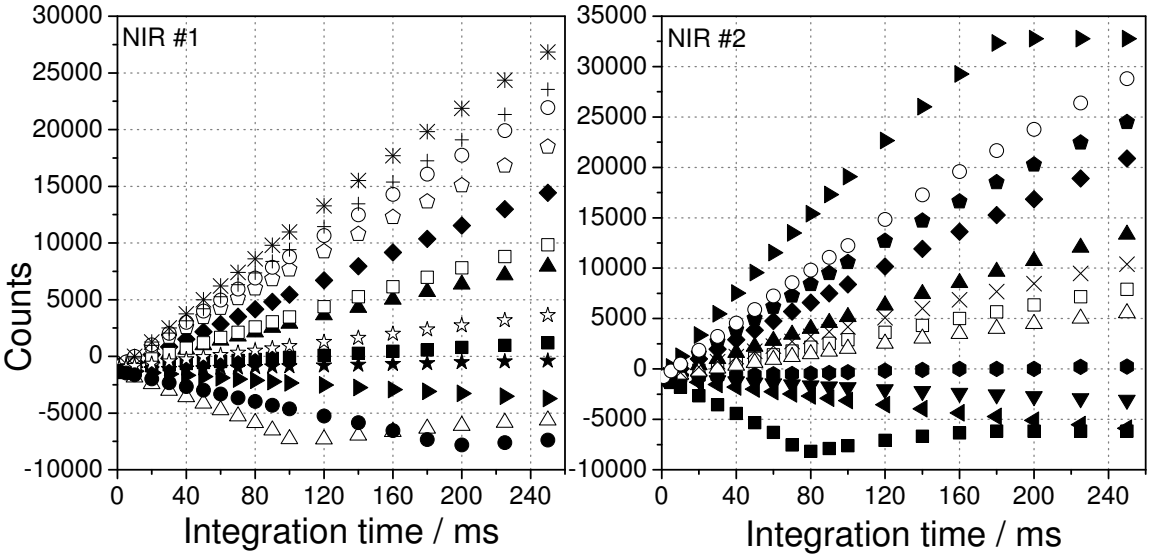

Figure 2.9: The dark signal of some examplarily chosen pixels of both MMS NIR spectrometers. Levels are generally higher in NIR #2, some pixels even exceed the maximum current so that their digitised value sticks at 32767 above certain integration times. Both spectrometers possess some pixels with a negative slope; above a certain integration time they enter a saturation regime: the exponential saturation behaviour is clearly visible in the solid-square curve of NIR #2.

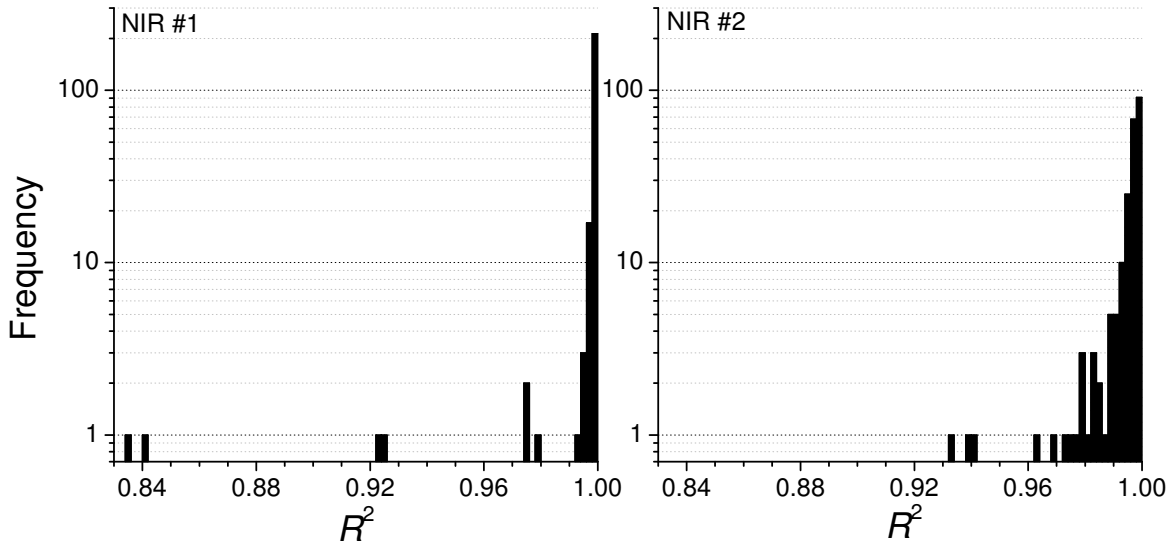

Figure 2.10: Histogram of coefficients of determination R^2 for a linear fit to the dark signal of MMS NIR spectrometers #1 and #2 in dependence on the integration time (up to 250 ms). Each bin is 0.002 wide. The lowest values correspond to pixels with a very low slope in Fig. 2.9.

The dark signal of each pixel n fluctuates around a fixed, characteristic mean value $y_0^{(n)}$. Its dependence on t_{int} is shown in Fig. 2.9. In the range of up to 250 ms, several pixels of NIR #2 overload, i.e. they reach the maximum value of 32767. Dark-signal levels of NIR #1 are lower and overload does not occur for $t_{\mathrm{int}} < 250$ ms. Some pixels have a negative slope and at some characteristic value of t_{int} change the sign of the slope. This seems to stem from a saturation process in the photodiode, as some curves exhibit a clearly exponential asymptotic behaviour. In total, NIR #1 has 14 pixels with this behaviour, while NIR #2 has 24 (out of a total of 256). Overload for $t_{\mathrm{int}} < 250$ ms occurs for 10 pixels of NIR #2. These numbers increase for longer integration times. Overall, these characteristics lead to the conclusion that the usable range of integration times is smaller for NIR #2 than for NIR #1. Consequently, in albedo measurements NIR #1 should be used for the lower upwelling irradiance, while the stronger downwelling irradiance favours the use of NIR #2 with lower integration times where it performs best.

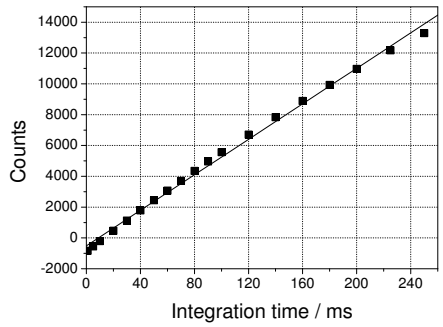

Figure 2.11: The typical curvature of the MMS dark-signal plot vs. integration time. It is generally more pronounced on NIR #2 than on NIR #1.

The linearity of the dependence of $y_0^{(n)}$ on t_{int} is checked in Fig. 2.10. The faulty pixels described in the preceding paragraph (overload and saturation effects) have been exempt from this evaluation. The correlation coefficients of NIR #1 are mostly larger than 0.996, with a few exceptions that have very low slopes in Fig. 2.9. The linearity of NIR #2 is not as good; the spread to lower values is larger. A close-up shows that the dark signal does indeed not exactly linearly increase with t_{int}; there is always a slight curvature which is more evident in NIR #2; see Fig. 2.11.

The dark-signal fluctuations $u_n(t)$ on time scales of a few seconds or longer can be accounted for by the shutter that is included into the NIR optical path and allows explicit measurements of the dark signal every few seconds. However, there are also faster fluctuations of the dark signal that are not accounted for by the shutter technique (see Fig. 2.7) and that are therefore imposed on the scientific signal. This amounts to a serious problem as the dark signal is very high, even higher than that of the detected radiation. Dark-signal fluctuations of only a few percent can and will have a strong impact on the net data, with no chance for a clean correction. Especially the weak upwelling irradiance is affected by dark-signal noise. The only way to reduce the noise would be long-term averaging. For airborne measurements averaging would lead to a serious decrease of spatial resolution. Eventually, the albedo spectrum is very noisy in the NIR range with the MMS spectrometers, as shown in Fig. 2.6.

t_{int} / ms	NOP PGS A	NOP PGS B
600	0	0
650	2	0
700	4	0
800	13	0
900	25	0
1150	65	0
1400	110	16
1600	137	50

Table 2.2: Number of overloaded pixels (NOP) for both PGS NIR spectrometers when measuring the radiation of a 1000-Watt lamp for different integration times.

2.4.2 New PGS spectrometers

Two NIR spectrometers of the new PGS system have been purchased and incorporated into the SMART-Albedometer (see Fig. 2.12). They are designated as PGS A and PGS B. With the PGS spectrometers, the NIR performance of the SMART-Albedometer was greatly improved. The manufacturers have optimised the photodiode material and reduced the dark signal to a significantly lower level, as shown in Fig. 2.13. With a low dark signal the integration time may be chosen in a larger range without the risk of saturation, net signals are less sensitive to dark-signal fluctuations and weaker signals can be detected.

The dark signal in dependence on the integration time is plotted in Fig. 2.14. Even at the maximum integration time of 1600 ms no pixels saturate or overload with the dark signal. Overload can occur, however, when an optically induced current is added to the dark current (Fig. 2.15). During tests with a 1000-Watt lamp, overload was observed for long integration times (Table 2.2) which are not expected to be used in experiments. Overload numbers may, however, change under ambient conditions.

The linearity of the dark signal with integration time is better than for the MMS NIR spectrometers (compare Fig. 2.16 of the PGS to that of the MMS, Fig. 2.10). For this comparison, the same range of integration times has to be taken into account. When, however, the full range of integration times is regarded, it is much

Figure 2.12: The NIR Plain-Grating Spectrometer (photo taken from Zeiss product information). The signal is fed into the optical fibre (upper right), falls onto the grating (inside at the lower left edge of the body) and is reflected on the photodiode array which carries the control electronics and a Peltier cooling unit, of which a fan is visible. – The insert on the lower right shows the InGaAs photodiode array (manufacturer product information from Hamamatsu, Japan).

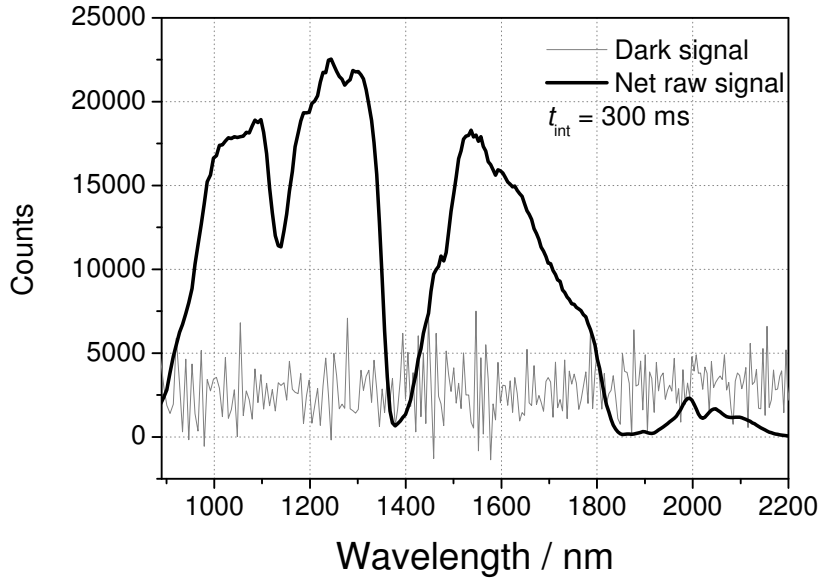

Figure 2.13: The dark signal of the PGS NIR spectrometers is lower than the signal of standard atmospheric radiation levels, extending the measurement capabilities of the SMART-Albedometer. In this plot a raw irradiance spectrum from the SAMUM campaign is shown (19 May, 2006) with the dark-signal (thin line) and the optical component (strong line). It has been recorded with an integration time of 300 ms.

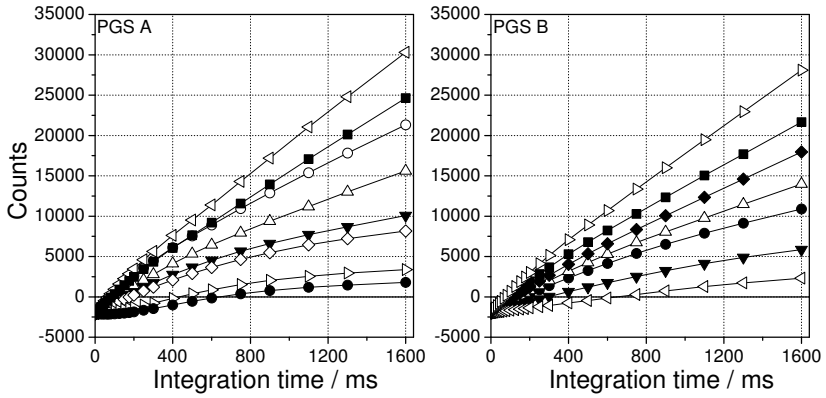

Figure 2.14: Dark signal of chosen pixels in dependence on the integration time for the two PGS NIR spectrometers.

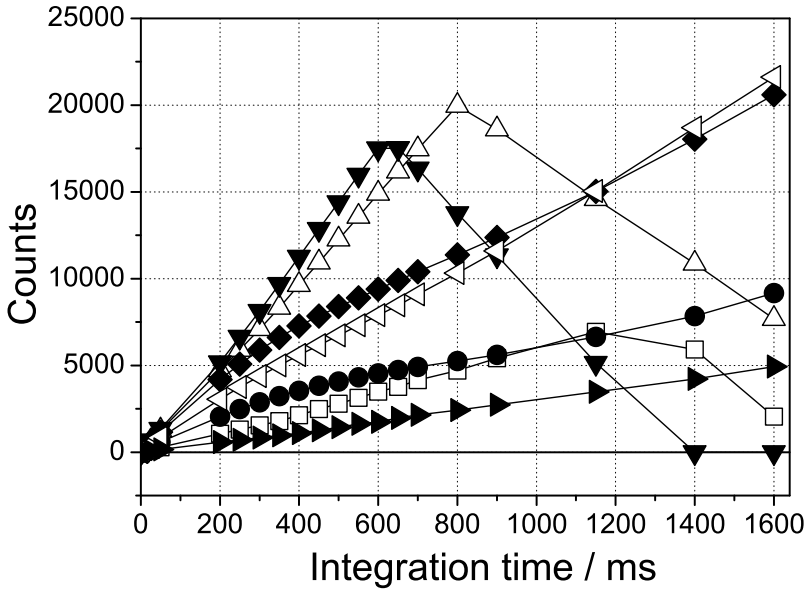

Figure 2.15: Net signal (illuminated minus dark) of a 1000-Watt lamp measured on the PGS A spectrometer. Several pixels overload because the sum of dark current and photocurrent exceeds the measurement range (32767 counts). While the dark-signal counts continue to increase with increasing integration time, the gross signal remains at 32767 counts. The net signal therefore decreases.

less appropriate to describe the dark-signal dependence on integration time with a linear formula (Fig. 2.16, lower panels). The curvature which has already been observed on the MMS spectrometers is more pronounced for long integration times (an exponential saturation process of the photodiodes). The non-linear behaviour of the dark signal with integration time is not critical for our measurements, because the dark signal is regularly measured with the shutters of the SMART-albedometer with an unchanged setting of the integration time. The dependence of the net signal on the strength of the light source is even better described by a linear relationship. To test this, a constant light source (1000-Watt lamp) has been placed in different distances from the optical inlet. In the distance range where the quadratic-distance law holds, the net signal vs. inverse squared distance is linearly fitted. The correlation is very good (Fig. 2.17).

In contrast, the dependence of the net signal on the integration time t_{int} shows strong deviations from linearity, especially for PGS A, not so much for PGS B (Fig. 2.18). Therefore it has to be guaranteed that each single raw dataset be converted to irradiance units by means of a calibration for which the same integration times as in the measurement has been used. Otherwise, the non-linearity leads to distortion and artificial peaks in the obtained spectrum.

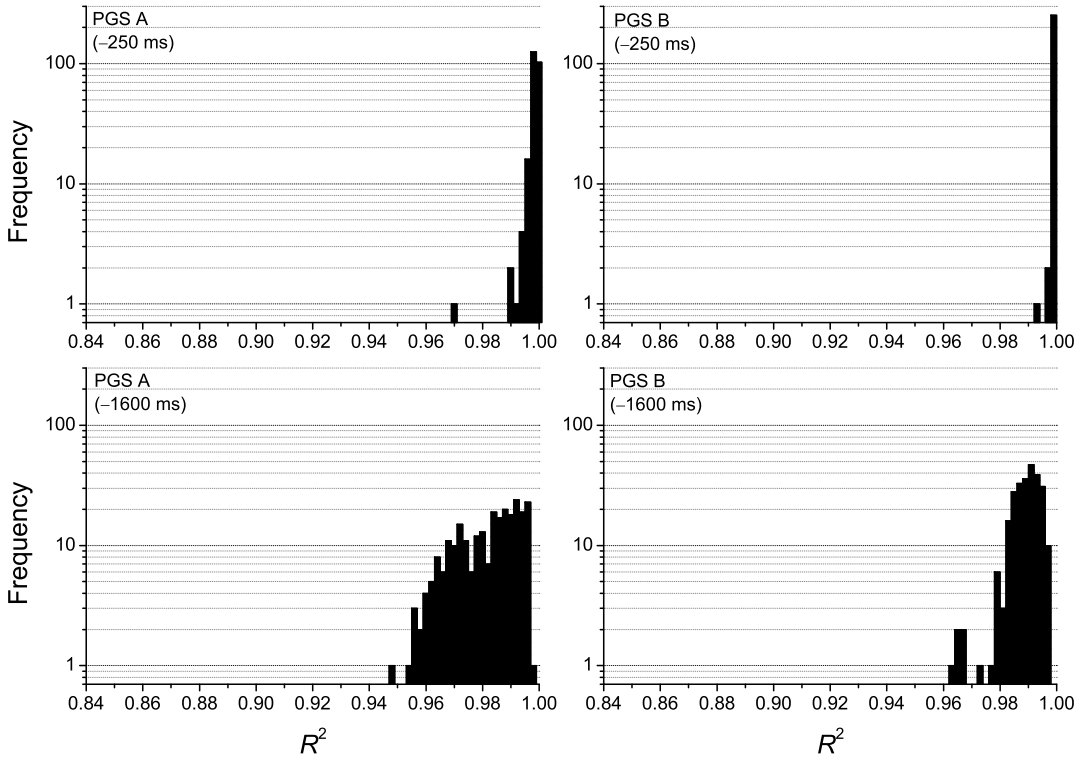

*Figure 2.16: Histogram of the coefficient of determination R^2 for a linear fit to the **dark** signal of the PGS spectrometers in dependence on the integration time. Upper panels: Taking into account only integration times up to 250 ms, for comparison to the MMS spectrometers, cf. Fig. 2.10. Lower panels: Taking into account the full range of integration times up to 1600 ms.*

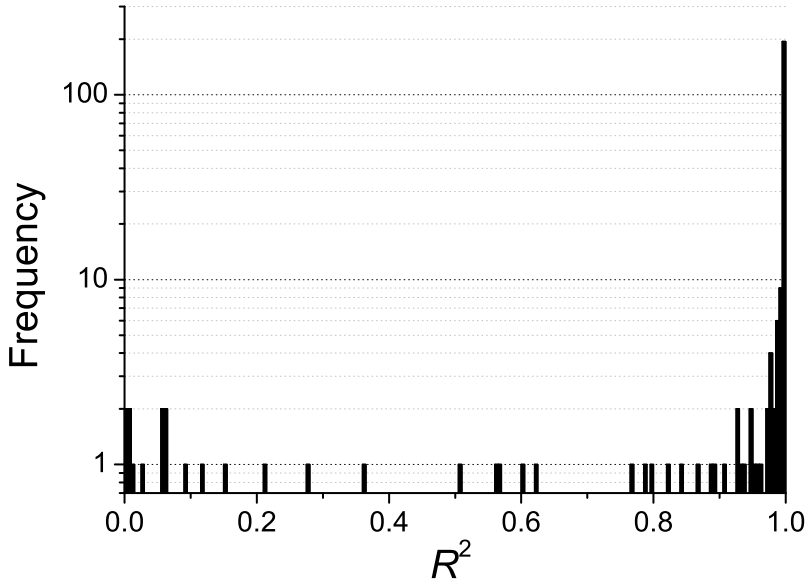

Figure 2.17: Histogram of the coefficient of determination R^2 for a linear fit of the net signal of the PGS B spectrometer in dependence on the radiation strength (represented by the distance r, namely r_{ref}^2/r^2) with $r_{\mathrm{ref}} = 50\,cm$ and r varying from 35 cm to 60 cm). Poor correlation values stem from the upper edge of the spectral range where net signals are very low and dominated by noise.

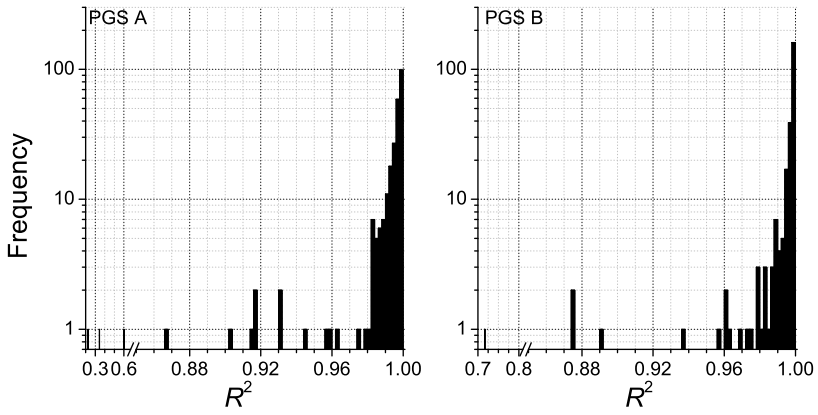

*Figure 2.18: Histogram of the coefficient of determination R^2 for a linear fit of the **net** signal of the PGS spectrometers in dependence on the integration time. Pixels that start to overload at a certain integration time have been analysed only for integration times without overload. Like in Fig. 2.17, lowest values of R^2 stem from low-signal pixels at the upper end of the measurement range.*

2.5 The optical inlets

2.5.1 Field of view of an ideal irradiance head

The irradiance optical inlets are designed to receive photons from all directions of a hemisphere. However, the cosine weighting makes certain photons more important than others, depending on their angle of incidence. Furthermore, when specifying a surface-albedo value for a certain point of flight, it is crucial to determine the surface area for which this value is significant. Given the measurement altitude h above ground, the area A, for which the measured surface-albedo value is significant, is given by:

$$A = \pi \cdot (h \cdot \tan\theta_{\mathrm{sig}})^2 \ , \tag{2.2}$$

where θ_{sig} is the maximum viewing zenith angle considered to yield significant contributions, or in other words half the angle of the cone from which radiation is considered to dominate the measured signal.

In order to quantify θ_{sig} we start from the definition of irradiance F as the cosine-weighted hemispherical integral of the radiance $I(\theta)$:

$$F = 2\pi \int_0^{\pi/2} I(\theta) \cos\theta \ \sin\theta \ d\theta \ . \tag{2.3}$$

The significant contribution F_{sig} is then given by the radiation that comes from a cone that is limited by the angle θ_{sig} ($0° < \theta_{\mathrm{sig}} < 90°$):

$$F_{\mathrm{sig}} = 2\pi \int_0^{\theta_{\mathrm{sig}}} I(\theta) \ \cos\theta \ \sin\theta \ d\theta \ . \tag{2.4}$$

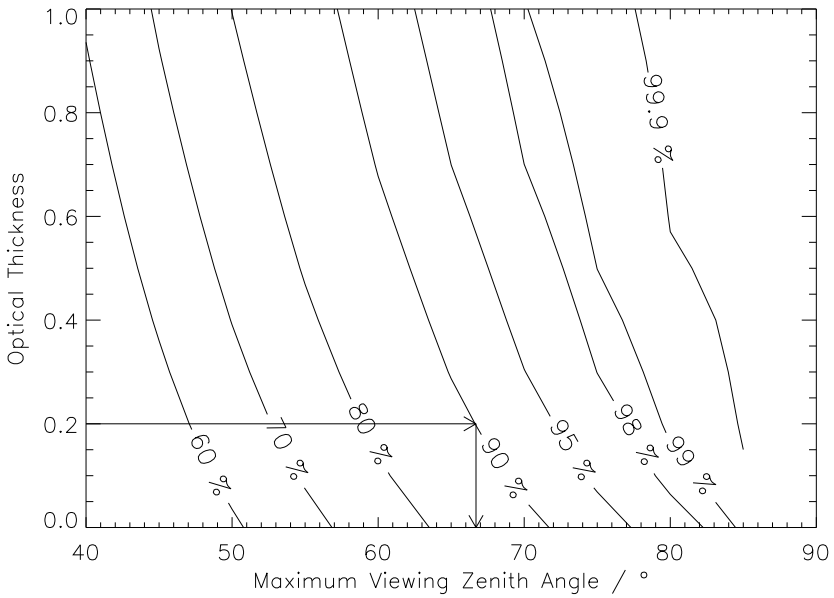

Figure 2.19: Contour plot of the fraction of measured surface *signal that is contributed by the irradiance that comes from directions within a certain maximum viewing zenith angle to the sensor. The contribution also depends on the optical thickness of the atmosphere, as surface photons at larger angles have travelled a longer optical path.*

On its way from the surface to the sensor, the radiance I_0 from the surface which is detected at an angle of incidence θ has been subject to extinction (neglecting multiple scattering) according to

$$I(\theta) = I_0 \exp\left(-\frac{\tau}{\cos\theta}\right) \ , \tag{2.5}$$

where τ is the optical thickness of the atmosphere. (Beware that here [and only here in this work] τ is AOD plus gas optical depth [Rayleigh]. Photons multiply scattered into this path otherwise than from the surface are neglected now.) Hence,

$$F_{\rm sig} = 2\pi I_0 \int_0^{\theta_{\rm sig}} \cos\theta \ \sin\theta \ \exp\left(-\frac{\tau}{\cos\theta}\right) d\theta \ . \tag{2.6}$$

The significance $\sigma(\theta_{\rm sig})$ is defined by the percentage

$$\sigma(\theta_{\rm sig}) = \frac{F_{\rm sig}}{F} = \frac{\int_0^{\theta_{\rm sig}} \cos\theta \ \sin\theta \ \exp\left(-\frac{\tau}{\cos\theta}\right) d\theta}{\int_0^{\pi/2} \cos\theta \ \sin\theta \ \exp\left(-\frac{\tau}{\cos\theta}\right) d\theta} \ . \tag{2.7}$$

This integral can easily be solved numerically. The result is shown in Fig. 2.19. This shows, for example, that at an optical thickness of 0.2, 90 % of the measured surface signal comes from within $\pm 67°$. At a flight altitude of 300 m the corresponding surface area is that of a circle of radius 643 m. If we ask for the area which contributes, say, 90 % of the measured signal, the corresponding viewing angle $\theta_{\rm sig}(\sigma = 90\,\%)$ of this area will decrease when the optical depth increases. This is because in an optically thicker medium the same optical path length is obtained on a shorter geometrical path length — and a shorter geometrical path length is achieved by reducing the viewing angle.

2.5.2 Characteristics of the optical inlets

Four sensor heads for the measurement of irradiance have been purchased from the Bay Area Environmental Research Institute (BAERI), Sonoma, California (see Fig. 2.20 for a sketch). They have been designed to detect radiation weighted by the cosine of its angle of incidence θ, where $\theta = 0$ corresponds to light that passes through the top of the quartz dome. The actual angular dependence of the sensitivity is, however, not a perfect cosine function. Thus the measured signal does not perfectly fulfil the definition of irradiance. To account for the difference, a cosine correction function $f_{\cos}$ is introduced (Wendisch, 2002) as

$$f_{\cos}(\theta) = \frac{F(\theta)}{F(\theta = 0) \cdot \cos\,\theta} \, . \tag{2.8}$$

This function yields correction factors that can be applied to the direct component of the measured signal to obtain the irradiance corrected for deviations from the ideal cosine weighting. $f_{\cos}$ has been determined for all sensor heads on our irradiance calibration stand, using constant illumination and turning the sensor head in $5 - 10°$ steps from $\theta = 0°$ to $\theta = 100°$. The results are fitted to a 9-order polynomial of the solar zenith angle. The resulting correction functions for all four sensor heads, VN1–VN4, are shown in Fig. 2.21, and the polynomial coefficients are tabulated in Table 2.3. The wavelength dependence was found to be small (see Fig. 2.22), and was neglected in the polynomial fit.

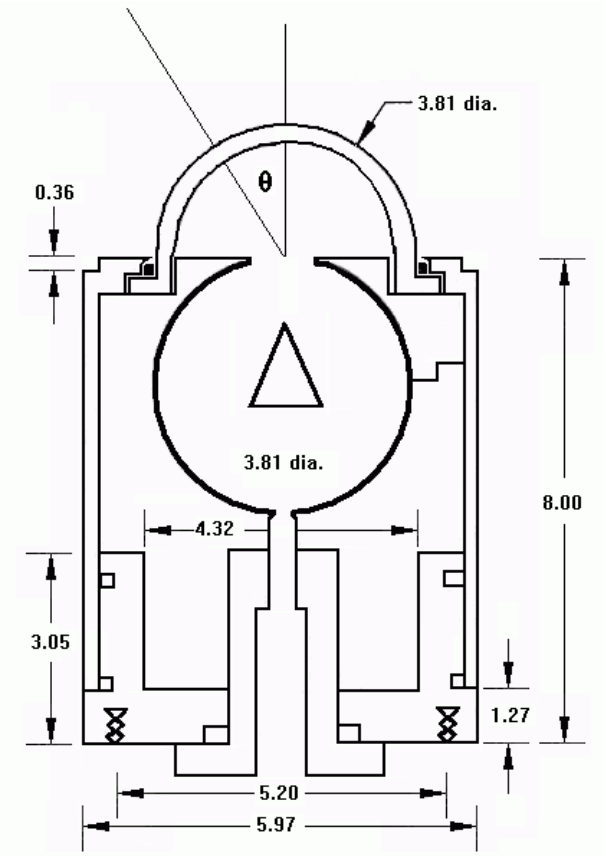

Figure 2.20: Sketch of the BAERI optical inlets for irradiance measurements. Through the top opening, radiation falls into a Spectralon® integrating sphere which provides the cosine-weighted collection of the signal and feeds it into the exit opening (bottom) which is designed for the connector of the optical fibres that lead to the spectrometers. A conical baffle is poised centrally in the integrating sphere to block direct illumination of the exit opening. The baffle occupies the entire field of view of the optical fibre in the exit port, which guarantees that each measured photon has experienced at least two reflections. For protection of the Spectralon® from contamination, a quartz-glass dome shields the top opening. The design is described in detail by Crowther (1997). All dimensions are given in cm.

This is another improvement in comparison to the older diffuser sensors. The maximum between 20° and 30° is caused by the geometry of the integrating sphere and the baffle (see Fig. 2.20): The half top angle of the baffle cone is 26°. Thus photons that enter the inlet at this angle have the highest probability of passing the baffle (parallel to its lateral surface) and hitting its base (and from there the exit) without further reflections. Compare this behaviour to that of the previously used diffuser inlets (cf. Fig. 2.21) which were based on transmission instead of reflection. Consequently, their cosine correction function is less than unity for most angles. The most important reason for their replacement, however, was that they are not applicable in the NIR range.

The correction function value is calculated as

$$f_{\cos}(\theta) = \sum_{k=0}^{9} c_k \cdot \theta^k \tag{2.9}$$

Sensor	c_0	c_1	c_2	c_3	c_4
VN1	1.00008	−1.51913E−3	−1.77407E−3	1.88173E−4	−1.16145E-5
VN2	1.00069	−9.69408E−3	1.74351E−3	−2.68498E−4	1.79312E-5
VN3	1.00035	−4.28413E−4	−1.46922E−3	1.23741E−4	−6.78057E-6
VN4	1.00062	−6.23409E−3	7.53669E−4	−2.03238E−4	1.64781E-5
Sensor	c_5	c_6	c_7	c_8	c_9
VN1	4.64574E−7	−1.12763E−8	1.57656E−10	−1.16522E−12	3.52655E−15
VN2	−6.17242E−7	1.21065E−8	−1.37711E−10	8.49680E−13	−2.20390E−15
VN3	2.77194E−7	−7.11140E−9	1.04082E−10	−7.94952E−13	2.46480E−15
VN4	−6.34224E−7	1.35687E−8	−1.66400E−10	1.09688E−12	−3.01255E−15

Table 2.3: Polynomial coefficients for the cosine correction of the direct component of the irradiance for all four sensor heads VN1–VN4.

Sensor	d_0	d_1	d_2	d_3	d_4
VN1	57.21578	−0.72207	4.02549E−3	−1.28145E−5	2.56777E−8
VN2	−173.99899	2.29014	−0.01321	4.40291E−5	−9.34050E−8
VN3	−68.65416	0.94979	−5.73549E−3	2.00650E−5	−4.47316E−8
VN4	−41.22209	0.59364	−3.70303E−3	1.33568E−5	−3.06075E−8
Sensor	d_5	d_6	d_7	d_8	d_9
VN1	−3.35796E−11	2.86404E−14	−1.53473E−17	4.68167E−21	−6.18129E−25
VN2	1.30750E−10	−1.20752E−13	7.09461E−17	−2.40646E−20	3.59093E−24
VN3	6.58139E−11	−6.38495E−14	3.93632E−17	−1.39889E−20	2.18313E−24
VN4	4.61306E−11	−4.56888E−14	2.86646E−17	−1.03369E−20	1.63275E−24

Table 2.4: Polynomial coefficients for the correction of the diffuse component of the irradiance for all four sensor heads VN1–VN4.

(θ given in degrees), with the coefficients c_k read from Table 2.3. Sensors VN1 and VN3 have been chosen for use with the airborne spectrometer system.

While $f_{\cos}$ is used for the correction of the direct component of the detected radiation, a different approach has to be applied for the diffuse component, because the signal consists of contributions from all angles. An integrated factor is used, and is tabulated as a 9-order polynomial of the wavelength for each of the four sensor heads. The polynomial coefficients are listed in Tab. 2.4, and a plot of the correction function is shown in Fig. 2.23. The correction function value is calculated as

$$f_{\text{diff}}(\lambda) = \sum_{i=0}^{9} d_i \cdot \lambda^i \tag{2.10}$$

(λ given in nm).

2.6 Calibration

2.6.1 Wavelength

The wavelength calibration is performed to confirm the relationship between the number of a pixel and wavelength of radiation measured by this pixel, as specified by the man-

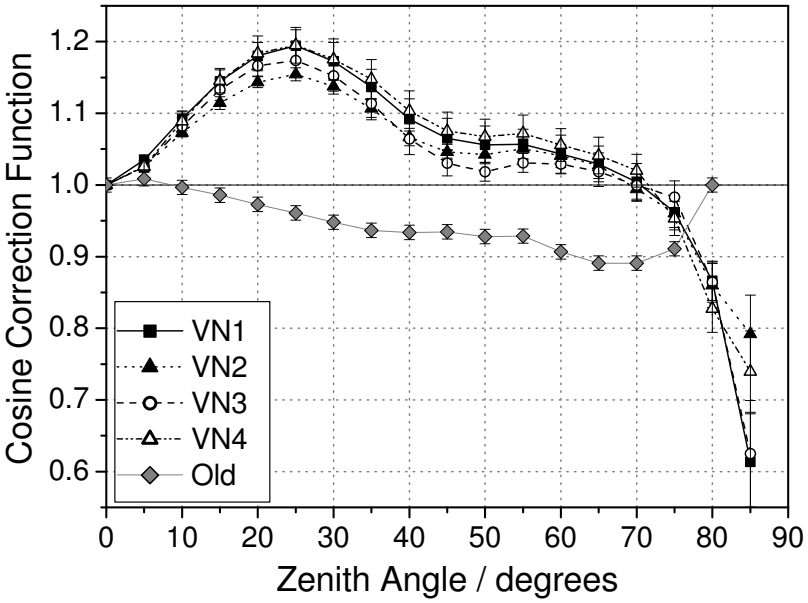

Figure 2.21: The cosine correction function for direct radiation for the four sensor heads VN1–VN4. The error bars indicate the range of values for different wavelengths. A sensor with an ideal cosine response function would have a constant value of 1 from 0° *to* 90°*, and 0 for angles larger than* 90°*. For comparison, the function of an old diffuser sensor ("Old") is shown (from Wendisch* et al.*, 2002).*

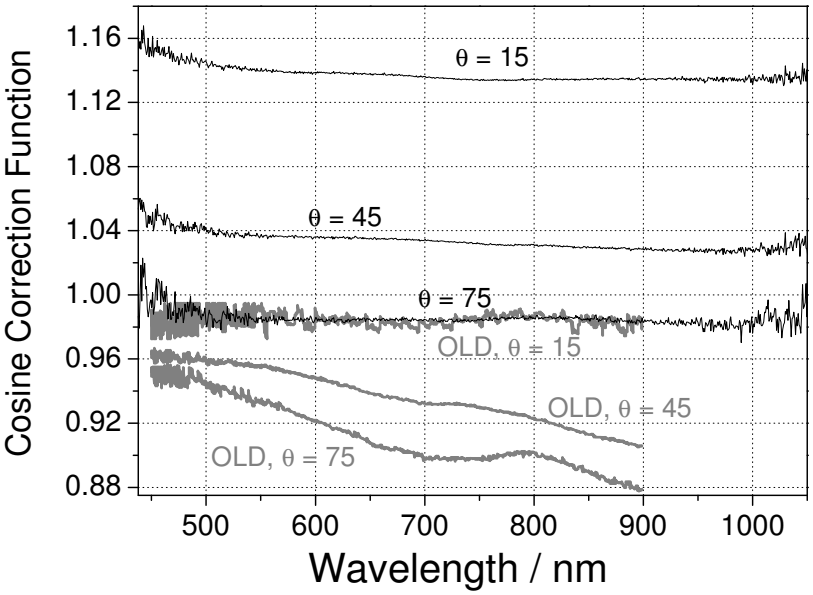

Figure 2.22: The wavelength dependence of the cosine correction function for direct radiation for sensor head VN3 (it is very similar for VN1, VN2, and VN4), and for comparison for an old diffuser sensor (grey lines) (from Wendisch et al.*, 2002).*

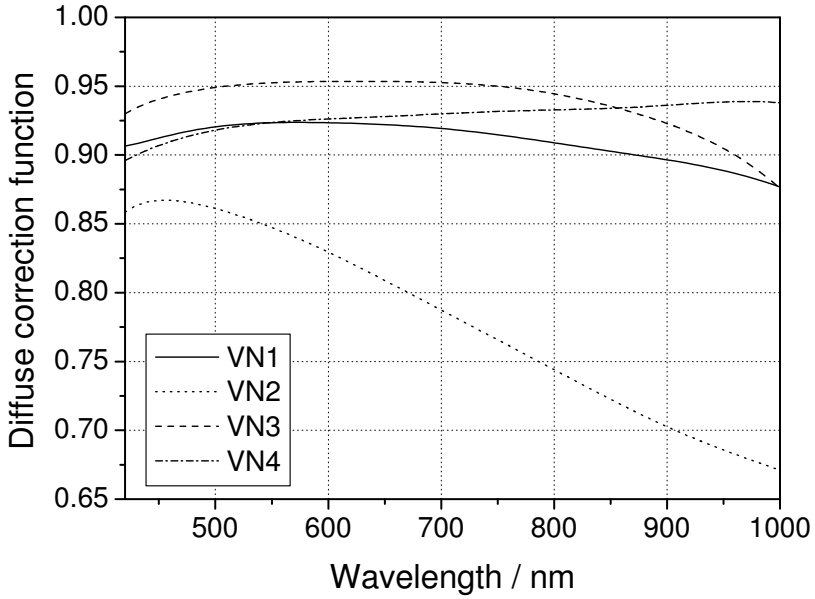

Figure 2.23: The correction function for diffuse radiation for the four sensor heads VN1–VN4.

ufacturer. This wavelength is determined by the grating of the spectrometer. Noble-gas emission lamps (Neon, Argon, Kryptonite) with a known spectrum of emission lines are used. The measured and the predicted spectrum are compared to each other in order to identify distinctive sets of emission lines. Only emission lines are used that do not overlap with other emission lines. Each line is then fitted to a Gauss curve. This yields the maximum position (in fractional pixel number units) of the measured Gauss curve, to which the nominal wavelength of this emission line is assigned. The total set of obtained pixel-wavelength relations is expressed as a polynomial function that covers all pixels of the spectrometer. Apart from the maximum wavelength, the Gauss-curve fit yields the line broadening (slit function) of the spectrometer. The measure of the line broadening is the full width at half maximum (FWHM) of the measured emission line (assuming that the actual wavelength range of the gas emission is infinitesimally narrow). Chosen emissions lines with their wavelengths and the obtained FWHM values are shown in Table 2.5.

2.6.2 Radiometric calibration

A 1000-Watt FEL calibration lamp (obtained from Opteema Engineering GmbH, Ilmenau, Germany) traceable to NIST[7] irradiance standards is used for the radiometric calibration of the spectrometric systems in the laboratory. Each combination of spectrometer, fibre, and optical inlet is mounted so that the inlet is exactly 50 cm from the reference point of the calibration lamp. The measured raw spectrum W_{cal} is related to the specified irradiance values F_{cal} of the calibration lamp to obtain the *absolute calibration factors*

[7]National Institute for Standards and Technology, USA

Wavelength / nm	Lamp	FWHM / nm
350.02	Hg	2.75
404.66	Hg	2.78
435.83	Hg	3.10
692.95	Ne	3.61
727.29	Ar	3.46
763.51	Ar	3.15
826.45	Ar	2.86
866.79	Ar	2.50
922.45	Ar	2.60
965.78	Ar	3.24
1014.25	HgAr	8.68
1125.80	Kr	10.16
1286.19	Kr	8.37
1442.70	Kr	10.16
1530.00	HgAr	10.11
1568.10	Kr	8.97
1582.01	Kr	12.56
1694.52	Ar	10.26
1709.88	Kr	9.57
1761.69	Kr	8.97
1782.89	Ar	15.54
1800.22	Kr	9.57
2116.55	Kr	14.35

Table 2.5: Spectral emission lines used for the wavelength calibration of the MCS (VIS) and PGS (NIR) spectrometers. Lamps used are mercury (Hg), mercury-argon (HgAr), argon (Ar), neon (Ne), and kryptonite (Kr).The full width at half maximum (FWHM) is that of a Gauss fit to the measured emission line.

f_{abs} for the given spectrometer system:

$$f_{\mathrm{abs}}(\lambda) = \frac{F_{\mathrm{cal}}(\lambda)}{W_{\mathrm{cal}}(\lambda)} \tag{2.11}$$

The optical connectors between the glass fibre and the spectrometers induce losses that vary whenever the plug is disconnected and reconnected (see Fig. 2.24). Furthermore, the transmissivity of the glass fibre depends on the geometric position of the fibre (bends). A series of test has been conducted with different combinations of bends in the fibre, with the optical inlet fixed in relation to a constant light source. The minimum bending radius of the optical fibres is 5 cm. The measured signals varies by up to a factor of 2.5, depending on wavelength (Fig. 2.25). Hence the transmission properties of the optical system between the optical inlet and the spectrometer change with each new system setup. This change needs to be quantified in order to compare the measuring system in the laboratory (where it is calibrated) and on the aircraft. A portable constant light source (an integrating Ulbricht sphere) is used for this purpose. After each measurement

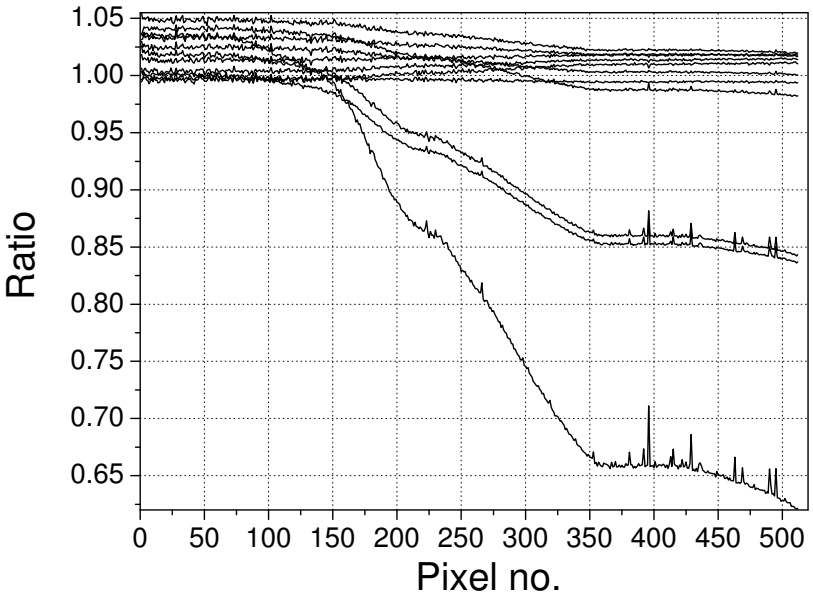

Figure 2.24: Change of the measured signal when the optical connector is unplugged and replugged several times, expressed as the ratio of each measured spectrum to the first.

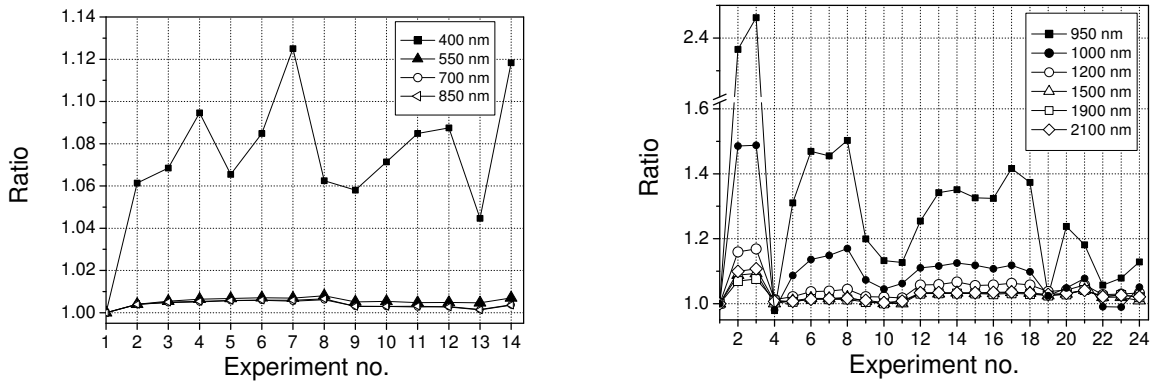

Figure 2.25: Results of the bending test for VIS (left) and NIR (right) wavelengths. The y axis is the ratio of the measured signal to that of the first experiment without bend. The bending test included 90° *turns, U turns, and* 270° *turns, each with different bending radii.*

flight, the spectrum F_{exp} of this lamp is measured and put in relation to the spectrum F_{lab} of the same lamp in the laboratory. This yields the *transfer calibration factors* f_{tra} for the correction of the spectrometer calibration:

$$f_{\mathrm{tra}}(\lambda) = \frac{F_{\mathrm{lab}}(\lambda)}{F_{\mathrm{exp}}(\lambda)} \tag{2.12}$$

2.7 Data analysis

Consider a dataset of n uncalibrated raw spectra from a measurement flight with a spectrometer with n_{pix} pixels. The datasets contains $n \cdot n_{\mathrm{pix}}$ points of raw data W_{ij} with $i = 0 \ldots n_{\mathrm{pix}}$ the pixel number and $j = 1 \ldots n$ the spectrum number. First, the log file of the horizontal stabilisation platform is analysed. Values of the pitch and roll angles must not exceed 5°, the acceleration limit is $0.5\,\mathrm{m\,s^{-1}}$, and the angular velocity is required to be lower than $3°\,\mathrm{s^{-1}}$. Whenever any of these limits is exceeded, the horizontal position of the optical sensors cannot be relied upon, and the measurements are discarded. The remaining dataset is $W_{ij'}$ where j' contains only those spectra that have been measured when the horizontal stabilisation worked within the specified parameters.

The dark signal $W_{i,\mathrm{dark}}$ is subtracted, and the net counts are multiplied with the absolute and transfer calibration factors from Eq. 2.11 and Eq. 2.12:

$$F^{(0)}_{ij'} = (W_{ij'} - W_{i,\mathrm{dark}}) \cdot f_{\mathrm{abs}} \cdot f_{\mathrm{tra}} \tag{2.13}$$

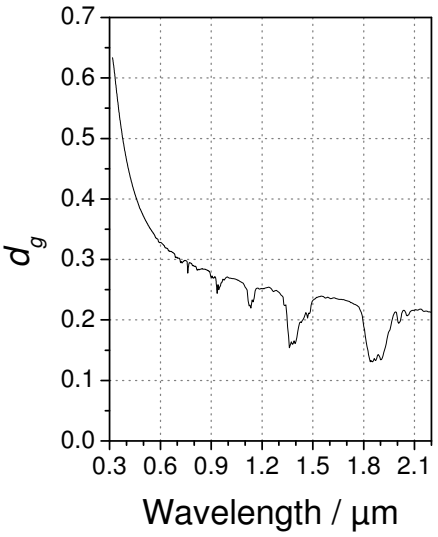

Figure 2.26: Diffuse fraction $d_g(\lambda)$ calculated for the dust conditions of Ouarzazate (Morocco) on 19 May, 2006.

In the next step, the obtained irradiance values have to be corrected for the non-ideal cosine characteristic of the respective sensor head (with the factors obtained in Eq. 2.9 and Eq. 2.10). For this it is necessary to estimate the direct ($F_{\lambda,\mathrm{dir}}$) and diffuse ($F_{\lambda,\mathrm{diff}}$) contribution to the irradiance under the given conditions. A radiative transfer model is used to calculate these components using the available atmospheric and aerosol information, and the diffuse fraction d_g, defined as

$$d_g(\lambda) = \frac{F_{\lambda,\mathrm{diff}}}{F_{\lambda,\mathrm{diff}} + F_{\lambda,\mathrm{dir}}}\,, \tag{2.14}$$

is saved. An example for the spectral shape of $d_g(\lambda)$ is shown in Fig. 2.26. It has been modelled for each measurement day using the spectral AOD measurements in Ouarzazate and/or Tinfou. The spectral behaviour of $d_g(\lambda)$ is dominated by Rayleigh scattering which is strongest at low wavelengths. Water-vapour absorption bands reduce $d_g(\lambda)$ because scattered radiation has a longer path in the water vapour than direct radiation.

The corrected irradiance values are then calculated as

$$F_{ij'} = (1 - d_g(\lambda_i)) \cdot F^{(0)}_{ij'} \cdot f_{\cos}(\theta_{j'}) + d_g(\lambda_i) \cdot F^{(0)}_{ij'} \cdot f_{\mathrm{diff}}(\lambda_i)\,. \tag{2.15}$$

This procedure is applied separately for the upwelling and the downwelling measurement. For upwelling irradiance, $d_g \equiv 1$ because there shall be no light source other than the sun which is always in the upper hemisphere.

Head	Position of receiving plane
VN1	−9.8 mm
VN2	−13.3 mm
VN3	−11.1 mm
VN4	−10.0 mm

Table 2.6: Position of the effective receiving plane of the four irradiance inlets, related to the top surface of the inlet housing.

2.8 Measurement uncertainties

The uncertainty of the irradiance measurements is determined by various sources: by radiometric and geometric uncertainties during calibration, by uncertainties connected with the determination of the correction factors of the optical inlets, by the uncertainty of the horizontal stabilisation during flight, and by fluctuations of the dark signal. Each of these factors is discussed in the following.

The uncertainty of the 1000-Watt calibration lamp, as specified by the manufacturer, amounts to 1.7 % between 250 nm and 1800 nm, and 3.4 % between 1800 nm and 2200 nm.

The distance between the calibration lamp and the optical inlet has to be the same as in the supplied specifications. While the reference point of the lamp is well defined, that of the optical inlet is not. The effective receiving plane of the inlet has to be determined by applying the squared-distance law: The inlet is illuminated by a constant light source, their distance is varied and the resulting measured irradiance is recorded. The plot of irradiance versus inverse-squared-distance plot is extrapolated to zero radiation, which yields the geometric position of the receiving plane. The values for the four optical inlets are given in Table 2.6. The uncertainty in the extrapolation process and of the final geometric adjustment has been estimated to yield ±1 % uncertainty in the irradiance data.

The determination of the cosine correction factors is limited by the angular uncertainty of the turntable (0.2°). This leads to ±1 % uncertainty in the irradiance.

Furthermore, the angular uncertainty of the horizontal stabilisation platform on the aircraft (also 0.2°) causes ±1 % irradiance uncertainty.

The fluctuations of the dark signal have to be considered separately for the VIS and the NIR spectrometers. There is a slight wavelength dependence of the dark signal of the VIS spectrometers, which is neglected in the data analysis as in-flight measurements of the VIS dark signal are not possible. Instead, the dark signal is estimated from the signal of the pixels below 290 nm. No photons should be detected in this range. The error made by the assumption of spectral independence amounts to maximum ±3 % of the dark signal. Typical values are 200 counts of dark signal (mean value of pixels below 290 nm), 20000 counts during a bright measurement (e.g., downwelling irradiance on a cloudless day) or 1000 counts during a darker measurement (e.g., upwelling irradiance). The error by the assumption of spectral independence then amounts to 0.03 % in the bright case and 0.7 % in the darker case. The temporal variability can be neglected, as the correction data are measured without time delay.

Error	$\lambda =$ **250–1000 nm**	$\lambda =$ **1000–1800 nm**	$\lambda =$ **1800–2200 nm**
Calibration lamp	1.7 %	1.7 %	3.4 %
Receiving Plane	1 %	1 %	1 %
Cosine Correction	1 %	1 %	1 %
Horizontal Misalignment	1 %	1 %	1 %
Dark-signal fluctuations	<0.7 %	<1.5 %	<1.5 %
Transfer Calibration	2 %	2 %	2 %
Sum	7.4 %	8.2 %	9.9 %
Gaussian Combination	**3.2 %**	**3.5 %**	**4.6 %**

Table 2.7: Measurement uncertainties of irradiance measurements.

The dark signal of the NIR spectrometers varies temporally, while its wavelength dependence is known and accounted for. For common measurement parameters (integration time, shutter cycle), the dark signal of the PGS spectrometers varies within ±50 counts. This corresponds to 0.3 % of the measured signal under bright conditions (15000 counts) and up to 1.5 % under darker conditions with lower (a few thousand) signal counts.

The calibration stability is checked after each measurement flight with a transfer calibration (portable integrating sphere as light source). During SAMUM, the obtained correction factors varied within ±2 %. This range is valid for all wavelengths.

The different sources of uncertainty can be considered independent of each other. Therefore they are combined by Gaussian error combination, and all values are presented in Table 2.7. The resulting irradiance uncertainty ammounts to 3.2 % for the range of the VIS spectrometers and 3.5 % to 4.6 % for the range of the NIR spectrometers. The uncertainty of the albedo at flight level, calculated as the ratio of the upwelling and the downwelling irradiance, is $\sqrt{2}$ times these values, following the law of propagation of random errors. The uncertainty of the derived surface albedo is larger, as the retrieval algorithm involves more quantities that bear uncertainties. An estimation with the help of sensitivity studies is presented in Section 4.2.

3 Experiments and Model

In this chapter, the two first field experiments of the extended SMART-Albedometer are described. For testing the SMART-Albedometer under ambient conditions, a test campaign has been performed in Brandis near Leipzig in 2005. This Brandis campaign is described in the first section. In 2006, the SAMUM field campaign took place in Morocco. The SAMUM measurements are described in the second section. The third section introduces the radiative transfer model that is used in combination with the measurements.

During both campaigns, the SMART-Albedometer was installed on a twin-engine Partenavia aircraft, callsign D–GERY (see Fig. 3.1). It is owned and operated by *enviscope GmbH* (Frankfurt am Main, Germany). It has been modified for the needs of scientific measurement flights, so it provides platforms and openings in the fuselage for optical and aerosol inlets, as well as wing pods. With the scientific payload of SAMUM, the maximum altitude is 3 km above sea level, and the maximum range is 4 flight hours at a speed of 60–70 $\mathrm{m\,s^{-1}}$.

3.1 Brandis Test Campaign

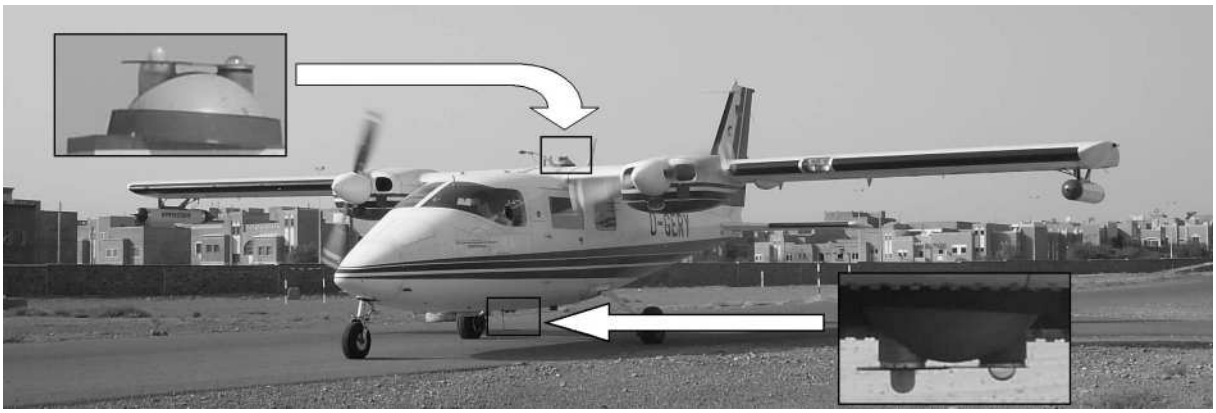

Figure 3.1: The Partenavia aircraft (D–GERY) at Ouarzazate airport, Morocco, with the upward-looking and downward-looking sensors of the SMART-Albedometer. Left to the upward-looking sensor is the aerosol inlet for PSAP, CPC, and the nephelometer. MOCIS is installed in the wingpods.

Instrument	Quantity
SMART-Albedometer	Up- and downwelling irradiance, 300–2200 nm Up- and downwelling actinic flux density, 250–700 nm
PSAP	Aerosol absorption coefficient
Radiance Research nephelometer	Aerosol scattering coefficient
CPC-3010	Aerosol particle number concentration
MOCIS	Particle impactor system

Table 3.1: Instrumentation of the Partenavia aircraft during the Brandis campaign, 2005.

3.1.1 General

A test campaign has been conducted from 27 June to 06 July, 2005, at the airfield in Brandis, a small town approximately 20 km to the East of Leipzig. This airfield has been chosen because its proximity to the IfT measurement field at Melpitz which is approximately another 20 km further east. This allows uncomplicated overflights for closure experiments with ground-based measurements.

Measurement flights have been conducted on 3 and 4 July, 2005. The flight pattern of both days is depicted in Fig. 3.2 and was designed to cover a wide range of different surface types. After the flight to Melpitz the track follows an almost northwesterly path along River Elbe, mostly above farmland and along the riverbed; then at the town of Elster the track turns in a southwesterly direction crossing farmland, a lake, and patches of wood until Gräfenhainichen is reached, then a third leg is flown in southeasterly direction across the *Dübener Heide* forest back to Melpitz. This pattern has been repeated at different altitudes: 1000 ft, 5500 ft, and 3500 ft.

This first airborne test of the new version of the SMART-Albedometer with extended wavelength range was generally successful. Problems have arisen, however, for the NIR spectrometer, especially with respect to upwelling irradiance, as the MMS spectrometers were used. At the necessary integration times the dark signal of the MMS spectrometers is so strong that its fluctuations impose a severe noise on the net signal that cannot be corrected (see Section 2.4.1). In this flight, integration times of around 200 ms have been chosen for the NIR instrument, as real-time quicklook spectra had suggested this to be an acceptable compromise between low signal intensity and strong dark signal. In the data evaluation process it turned out, however, that nevertheless the obtained NIR albedo spectra are very noisy. Longer integration times should have been used in favour of a higher signal-to-noise ratio, even though this leads to a higher number of saturated (or non-linear) and therefore useless pixels. This would have meant to have less but better data. Due to these problems, the NIR range has been excluded from the further evalutation.

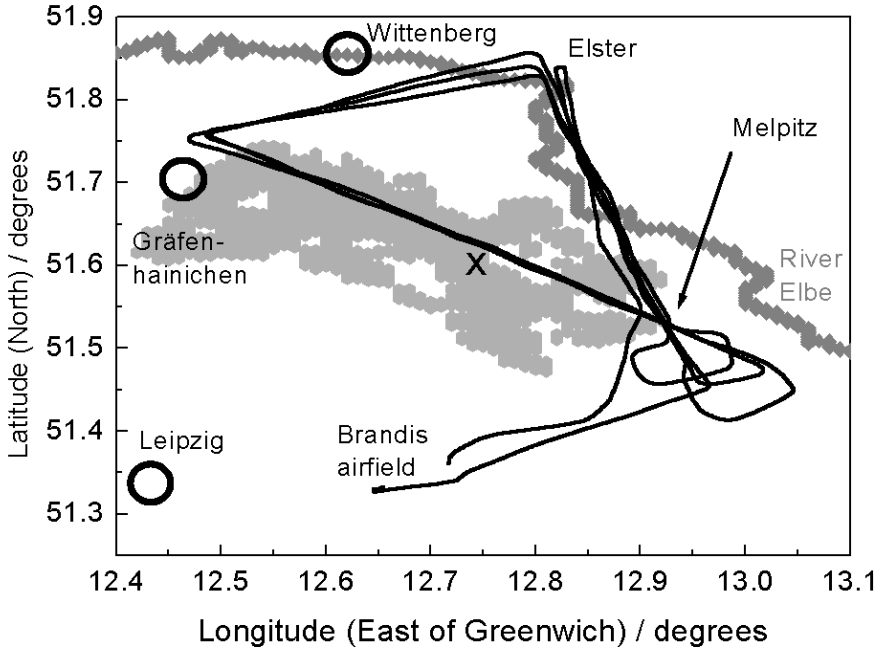

Figure 3.2: Diagram of the flight pattern on 4 July, 2005, during the Brandis campaign. The grey area in the centre is the Dübener Heide forest. The location of nearby cities and of the Melpitz ground station is indicated. The forest-farmland boundary used for the estimate of the effective view of the optical inlets is marked as "x". Parts of the same pattern have been flown on 3 July.

3.1.2 Surface-Albedo Measurements

Over land, vegetation is the major factor influencing the surface albedo. The measurement area included farmland with different crops, forests and groves, wetlands on the banks of River Elbe, towns and villages, roads and railways, and one lake. The SMART-Albedometer always measures an areal average of the surface albedo, because from our elevated point of view we detect irradiance reflected from a wide area that includes different surface types. Nevertheless, sufficiently large homogeneous areas – especially of forest and farmland – have been encountered to identify their typical surface-albedo spectra.

Spatial resolution is additionally restricted by the speed of the aircraft. A typical speed for the Partenavia aircraft is $60\,\mathrm{m\,s^{-1}}$. With an average integration time of more than one second (for the VIS spectrometer) surface elements smaller than 60 m will only contribute a small percentage of photons to the measured spectrum. Therefore, small-scale features such as isolated bushes or trees, roads, or railways hardly yield a measurable impact on the measured spectra.

We have used the data to confirm the effective field of view of the optical inlets. The theoretical field of view of an ideal cosine-weighting inlet has been derived in Section 2.5.1. For an experimental confirmation, a clear boundary between dark and bright surfaces offers a good test case – the temporal development of the measured surface albedo should depict the movement across the boundary.

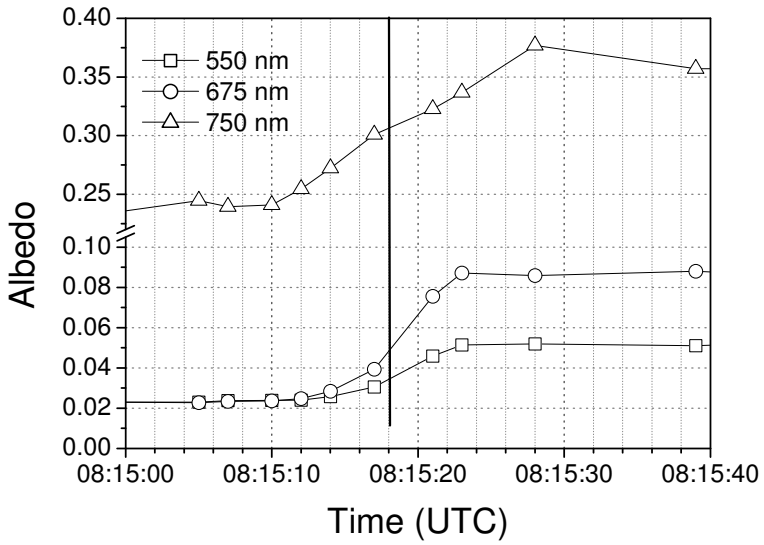

Figure 3.3: Development of the surface albedo whilst flying from forest into farmland at two wavelengths below the vegetation step (450 nm and 675 nm) and one beyond (750 nm). The boundary was crossed at 08:15:18 UTC (marked by a line).

In the flight pattern of the Brandis experiments, two such boundaries were crossed: the points where the aircraft entered and left the Dübener Heide forest. The edge of the forest runs almost perpendicularly to the flight direction, so there is a sharp transition from relatively bright farmland surface to darker forest-covered surface, and vice versa. The surface albedo at different wavelengths during the transition from forest to farmland is shown in Fig. 3.3. The strong increase corresponds to the change in surface type. At 750 nm, 70 % of the increase are reached 5 seconds after the crossing of the border line. We assume therefore that 70 % of the viewed surface circle at that moment was farmland. The area of a circle segment is given by

$$A_i = r^2 \arccos\left(1 - \frac{d_i}{r}\right) - \sqrt{2rd_i - d_i^2} \cdot (r - d_i) \ , \tag{3.1}$$

where r is the circle radius, $i = 1, 2$ denotes one of the two segments, A_i is the area of segment i, and d_i is that part of the circle diameter that lies within the section. For an illustration, see Fig. 3.4.

With the help of Eq. 3.1, we find that axis of a circle segment that covers 70 % of the entire circle has a length of $1.33 \cdot r$. The aircraft is above the centre of the circle, while the forest-farmland boundary forms the edge of the segment, so the distance between the aircraft nadir and the boundary is $0.33 \cdot r$. We know that this distance has been passed in 5 seconds at an aircraft speed of $60\,\mathrm{m\,s^{-1}}$ so $0.33 \cdot r = 60\,\mathrm{m\,s^{-1}} \cdot 5\,\mathrm{s} = 300\,\mathrm{m}$ and thus $r = 921\,\mathrm{m}$. At an altitude of 180 m above ground, this leads to an effective maximum viewing angle of 79°.

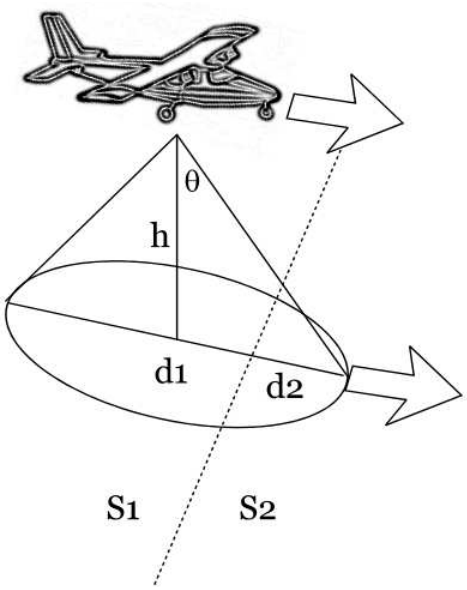

Figure 3.4: Plot showing the geometry of flying across a surface-type boundary. The circular field of view (radius r) is divided in two segments with surface type s_1 and s_2. The segment axes d_1 and d_2 (parallel to the flight direction, $d_1 + d_2 = 2r$) determine the area ratio and thus the contribution of both albedo types.

This estimation however, disregards the cosine weighting of the optical inlets. An algebraic expression that includes cosine weighting into Eq. 3.1 is not available. Therefore, the "cosine-weighted area" of a circle segment has to be calculated numerically. The circle area is approximated as a composition of many small squares. The sum is taken of the area of all squares that fall into the segment, multiplied by the cosine of the viewing angle of each square. Without this multiplication, the sum is an approximation of the result of Eq. 3.1. The ratio of the segment area with and without cosine weighting to the area of the entire circle is plotted in Fig. 3.5. The unweighted plot is not distinguishable from that of the algebraic expression, so the approximation with squares of $r/100$ width is sufficiently precise.

We can now use Fig. 3.5 to determine the distance of the aircraft to the surface-type

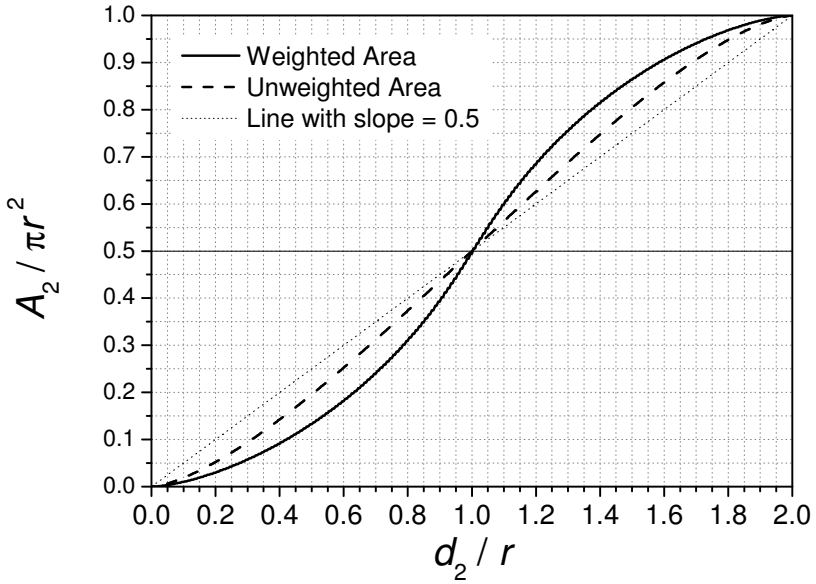

Figure 3.5: Ratio of the area of a circle segment to the area of the entire circle, in dependence on the position of the segment boundary. See Fig. 3.4 for an illustration of the geometry. The segment area can be calculated isotropically (with respect to the viewing angle) according to Eq. 3.1 (dashed line), or numerically taking into account the cosine weighting of the optical inlet (area elements just beneath the aircraft contribute more than those at high viewing angles).

boundary from the relative albedo change. The value of $0.33 \cdot r$ for 70 %, disregarding cosine weighting (dashed line), can thus be confirmed. If the cosine weighting is taken into account (solid line), a value of $0.23 \cdot r$ is found. Using the aircraft speed and altitude, this translates to an effective maximum viewing angle of 82° instead of 79°.

The same estimation is done at 450 nm. From Fig. 3.3 we read that 80 % of the albedo change has occurred 3 s after the aircraft has passed the forest-farmland boundary. Taking cosine weighting into account, Fig. 3.5 tells us that the aircraft has moved $0.37 \cdot r$ into the farmland area, so $0.37 \cdot r = 60\,\mathrm{ms}^{-1} \cdot 3\,\mathrm{s}$ and thus $r = 486\,\mathrm{m}$. Thus the effective maximum viewing angle at 450 nm is 70°, compared to 82° at 750 nm.

The AOD has been derived from sun photometer measurements in Melpitz as 0.35 at 450 nm and 0.16 at 750 nm. Standard Rayleigh optical depth (0.22 and 0.03 at 450 nm and 750 nm, respectively) has to be added to obtain total extinction. Then, according to Fig. 2.19, a viewing angle of 82° at 750 nm yields 99 % of the surface signal. A viewing angle of 70° at 450 nm yields 96–97 %. The difference in these percentages is mainly caused by the temporal resolution of the measurement, which is low for this application. Allowing a time uncertainty of ±1 s, the percentage obtained for this case from Fig. 2.19 ranges between 89 % and 99 %.

Nevertheless, we see that the derived angles yield 96–99 % of the measured surface signal. This leads to the conclusion that at NIR wavelengths even the contributions from large viewing angles cannot be neglected (at least for cases with high contrast, such as this case with a transition from forest to farmland). At blue wavelengths, the largest viewing angles contribute very little, but these are not less than 70°.

In order to check whether this wavelength-dependent behaviour is due to the wavelength dependence of the optical depth (dominated by that of the Rayleigh component), or by the enhanced surface albedo in the NIR (more photons available let the information be carried further), the same estimation is repeated for a red wavelength just below the vegetation step. At 675 nm, 82 % of the albedo change have occurred 3 s after passing the forest-farmland boundary. This is almost the same as at 450 nm, and accordingly the effective maximum viewing angle is also similar, 68°. But with reduced optical depth at this wavelength (0.21 measured AOD, 0.04 Rayleigh), this angle contributes a mere 93 % to the measured signal. This is less than at 450 nm, although the value at 750 nm is higher than that at 450 nm. Even though again we have to consider the uncertainties due to the low temporal resolution, this means that the field of view is larger when the surface is brighter, and that over dark surfaces the reduction of optical depth with increasing wavelength does not necessarily increase the field of view significantly.

Examples for albedo spectra of different surface types are given in Fig. 3.6. Typical features are the local maximum around 550 nm which corresponds to the omnipresent green colour, and the vegetation edge around 700 nm which is a consequence of the heat-

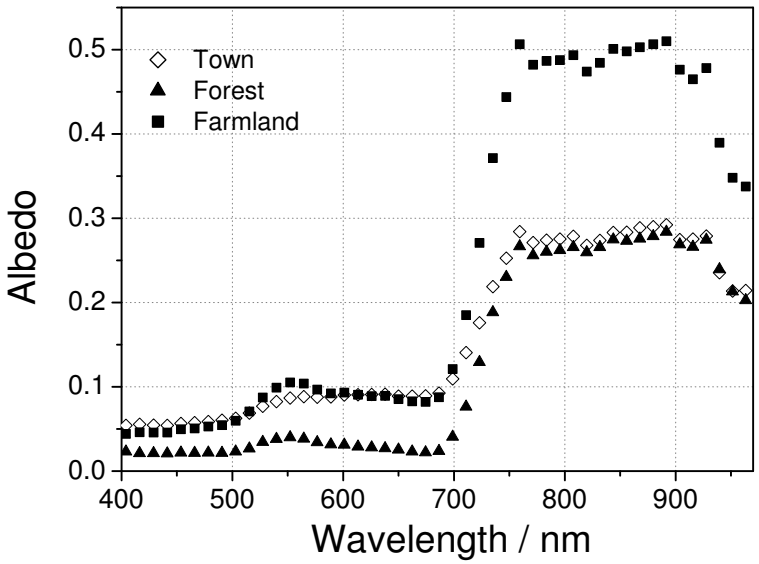

Figure 3.6: Example plots of the spectral surface albedo derived from irradiance measurements during the Brandis campaign above different surface types — a town, forest, and farmland. The small peak at 762 nm is caused by the oxygen absorption band at this wavelength (no atmospheric correction has been performed for the Brandis data).

protection mechanism of plants (increased reflection of harmful infrared radiation). The shape and values of the spectral surface albedo (especially in the 550–700 nm range) and the height of the 750–900 nm plateau depend on surface characteristics such as plant species, vegetation season, and coverage. Generally, forests exhibit low surface-albedo values.

Most surface-albedo spectra can be classified by certain sensitive wavelengths. This can be done by making use of some typical spectra features. One of these is the so-called vegetation step (or red step) around 700 nm. It is dominated by the reflection at the boundary between air and the cell walls of the plant tissue. Vegetated surfaces appear darker below 700 nm. In this range plant absorption is dominated by carotenoid pigments (around 480 nm) and chlorophylls (around 680 nm), with a peak inbetween where absorption is less which represents the green colour of vegetation (Bowker *et al.*, 1985).

By comparing the surface-albedo values at different wavelengths, say, 550, 650, and 750 nm, a surface-albedo spectrum can be classified with indices and even related to the surface type. Several such indices are presented in the literature for an assessment of vegetation properties such as water content, or photosynthetic productivity (see, for instance, Gamon *et al.*, 1995; Peñuelas and Filella, 1998). A common example of those indices is the *Normalised Difference Vegetation Index* (*NDVI*; *ibd.*) which is generally defined as

$$(R_{\mathrm{NIR}} - R_{\mathrm{red}})/(R_{\mathrm{NIR}} + R_{\mathrm{red}})\,. \tag{3.2}$$

Here, R_{NIR} and R_{red} are the reflectances at NIR and red (visible) wavelengths, respectively (or wavelength ranges, in case broadband detectors are used). The *NDVI* for the surface-

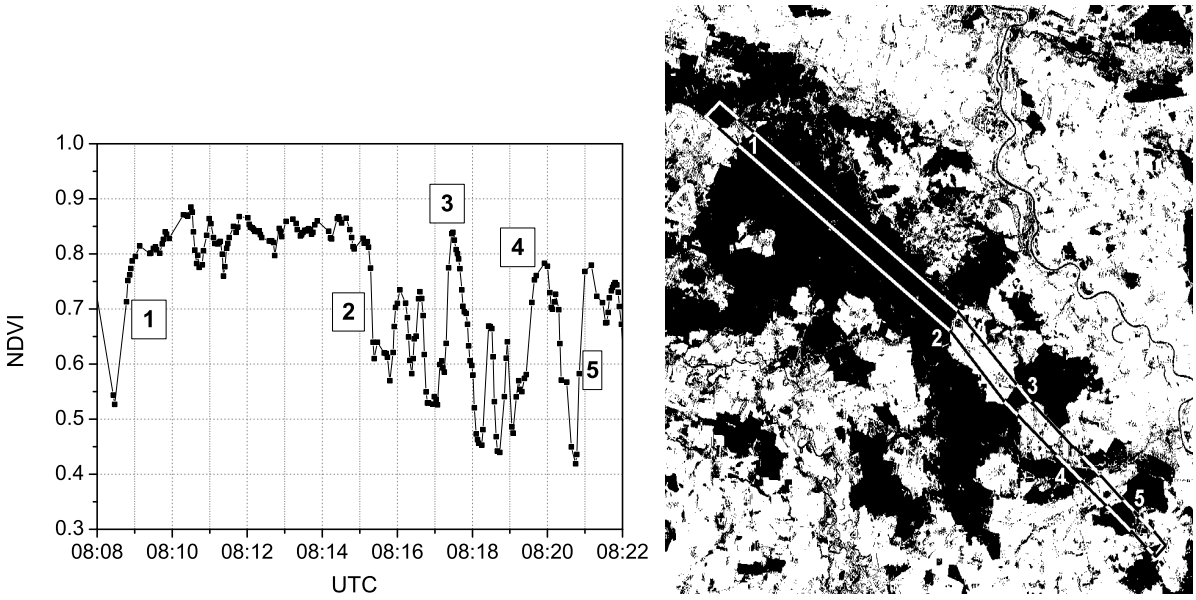

Figure 3.7: The Normalised Difference Vegetation Index (NDVI) (see text), calculated from the surface-albedo values at 645 nm and 900 nm for a flight segment on 4 July, 2005.

albedo data from the Brandis campaign has been calculated using measurements at 645 nm and 900 nm. For a flight leg above forest and farmland areas this is shown in Fig. 3.7. The sharp increase at 08:09 UTC and the decrease at 08:15 UTC neatly corresponds to the points where the aircraft entered and left the Dübener Heide forest (points 1 and 2, respectively). Also the peaks at 08:17, 08:20, and 08:21 coincide with the crossing of other forest areas (points 3, 4, and 5). Smaller peaks reflect smaller vegetation features, such as groves. Farmland areas are essentially represented by low values of *NDVI*. This may be due to a lack of chlorophyll in the ripening cereals grown in the measurement region, as the experiment was conducted in July. With reduced chlorophyll absorption *NDVI* will increase. But also the increased visibility of the underlying soil between the cereal plants contributes to the decreased *NDVI*. Forests and groves appear in a green colour also in July, and they hide the soil from airborne observers, and correspondingly they lead to high *NDVI* values.

#	Research Group(s)	Title
1	Institute for Atmospheric Physics, German Aerospace Center (DLR)	Airborne in-situ and remote-sensing studies on the vertical and area distribution of microphysical and optical properties of Saharan dust
2	Institute for Remote Sensing, German Aerospace Center (DLR); Leibniz Institute for Tropospheric Research (IfT)	Radiative properties of Saharan dust; In-situ aircraft measurements and model calculations
3	Leibniz Institute for Tropospheric Research (IfT)	Regional modelling of the Saharan dust cycle
4	Leibniz Institute for Tropospheric Research (IfT); Institute for Meteorology, University of Munich	Vertically resolved characterisation of Saharan dust based on observations with lidars
5	Leibniz Institute for Tropospheric Research (IfT)	Hygroscopicity and optical properties of dust particles: Technical development and field application
6	Institute for Atmospheric Physics, Johannes Gutenberg University Mainz; Institute for Mineralogy, Technical University Darmstadt	Physicochemical parameters of desert aerosols
7	Institute for Environmental Research, University of Bremen	Dust aerosol REtrievAl from spaceborne instruMentS (DREAMS)

Table 3.2: The seven project groups that make up the SAMUM consortium.

3.2 SAMUM - The Saharan Mineral Dust Experiment

The *Sa*haran *M*ineral D*u*st Experi*m*ent (SAMUM) is a DFG[1]-funded joint project of several German research institutes. One of the major objectives of this project is to enhance the understanding of the radiative effect of Saharan mineral dust. The range of theoretical and experimental tasks is covered by various working groups from different institutes. These groups joined together to form seven projects which are listed in Table 3.2. Additional corporation has taken place with the Mohammed I. University of Oujda, Morocco, as a local partner, as well as with the MISR team of NASA Jet Propulsion Laboratory (JPL) for a link to satellite measurements.

3.2.1 Field campaign

The SAMUM field campaign took place in May and June, 2006, in the provinces of Ouarzazate and Zagora in south-eastern Morocco. A map of the region is shown in Fig. 3.8. It is located south of the High Atlas mountains which blocks air masses from the

[1]Deutsche Forschungsgemeinschaft - German Research Foundation

Instrument	Quantity
SMART-Albedometer	Up- and downwelling irradiance, 300–2200 nm Up- and downwelling actinic flux density, 250–700 nm
PSAP[2]	Aerosol absorption coefficient at 565 nm
Nephelometer 3563[3]	Aerosol scattering coefficient at 450, 550, and 700 nm
CPC-3010[3,4]	Aerosol particle number concentration
MOCIS[5]	Particle impactor system

Table 3.3: Scientific instrumentation of the Partenavia aircraft during the SAMUM campaign, 2006.

North. It is close to the Sahara desert which lies to the south and to the east of the Zagora basin. The SMART-Albedometer was mounted on the D–GERY Partenavia aircraft which was based on the airport of Ouarzazate. The Compact Radiation Measurement System (CORAS) was also operated on this airport, as well as three lidars, a sun photometer, and a radiosonde station for measurements of the aerosol and meteorological conditions. At the second SAMUM location in Tinfou (near Zagora) in-situ dust measurements and aerosol sampling were conducted and a sun photometer was operated. A second aircraft, the Falcon of the German Aerospace Center (DLR), operated from Casablanca Airport and provided in-situ aerosol measurements and remote-sensing data from a nadir-looking lidar. Additionally, results from the satellite instruments MERIS (Medium Resolution Imaging Spectrometer) and MISR (Multi-Angle Imaging SpectroRadiometer) and from a complementary lidar station in Évora (Portugal) have been incorporated into the SAMUM project. A detailed description of the experiment and the results from the various project groups are to be presented in a special issue of the journal *Tellus B* (Heintzenberg, 2009).

A total of 13 measurement flights have been performed with the Partenavia aircraft (Fig. 3.1) in the period from 19 May to 6 June, 2006. A map showing all flight routes is shown in Fig. 3.9. The flights were planned on a day-to-day basis in order to follow the actual dust conditions, but were in general designed to fly over the broadest possible range of surface types. The prevailing surface type in the provinces of Ouarzazate and Zagora is barren hamada (stone desert) of brown-reddish colour. However, also vegetated spots are encountered, mainly in form of oasis in the valleyw of the rivers Drâa and Dadès, as well as vegetation spots at the outflow of small valleys from the Atlas mountains. To the south of Zagora the river Drâa evaporates which forms a salt crust in the dry lake Iriki, hence a particularly bright spot.

The SMART-Albedometer operated on all 13 flights without technical problems. The integration time was adjusted manually by the flight engineer for an optimal exploitation of the dynamic range in dependence on the actual radiation conditions. Cabin temperatures ranged between 10 °C and 40 °C and did not pose a problem to the cooling system of the spectrometers.

[2]Particle Soot/Absorption Photometer, manufactured by Radiance Research, Seattle, USA.
[3]Manufactured by TSI Inc., Shoreview, USA.
[4]Condensation Particle Counter.
[5]Mobile Cascade Impaction System, developed by Johannes Gutenberg University, Mainz, Germany.

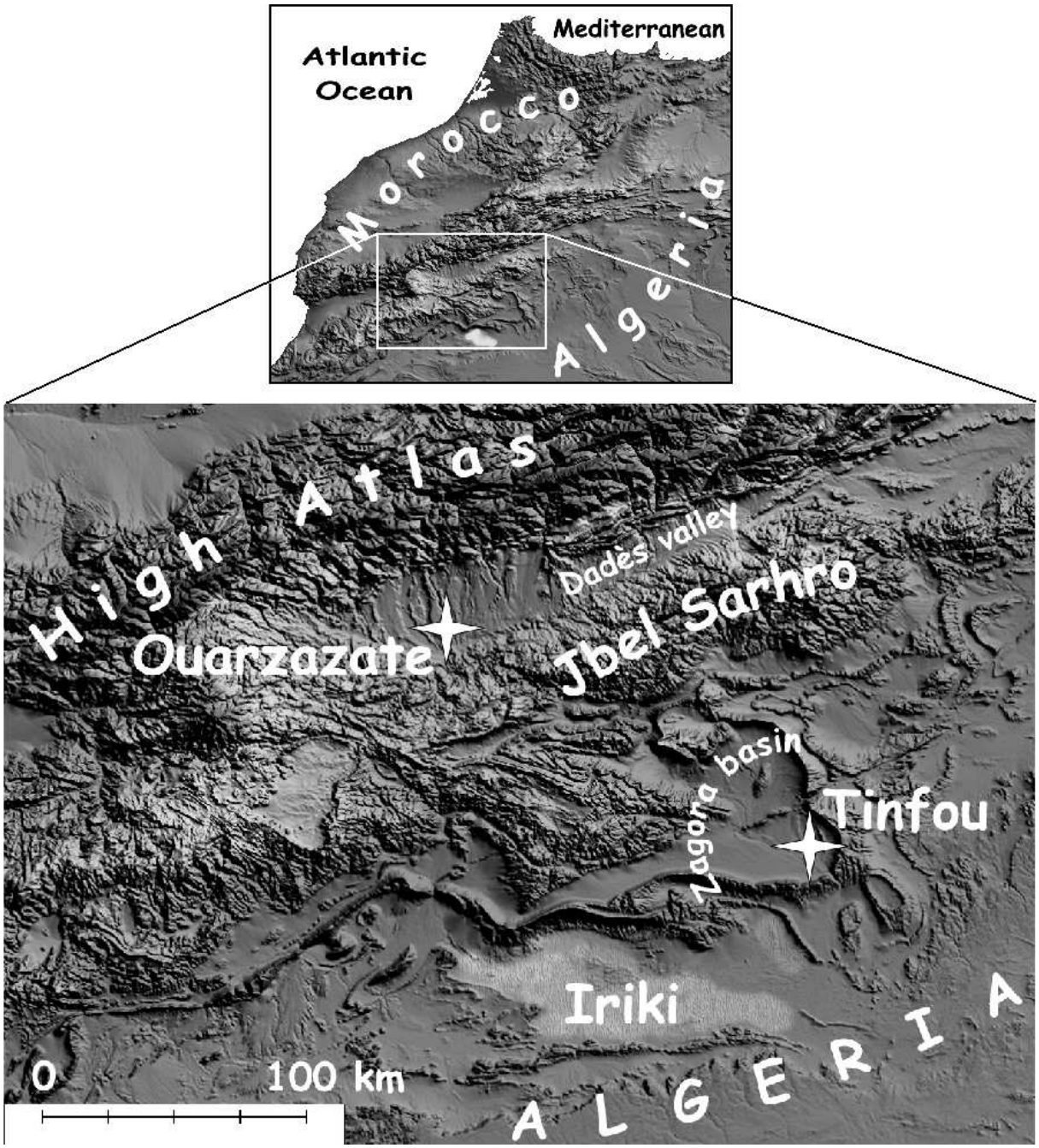

Figure 3.8: Geographical overview of the SAMUM measurement area in Morocco. All Partenavia flights started at Ouarzazate airport (coordinates $30.9^\circ N$, $6.9^\circ W$*), and many targeted the Zagora basin with the Tinfou ground station (coordinates* $30.24^\circ N$, $5.61^\circ W$*).*

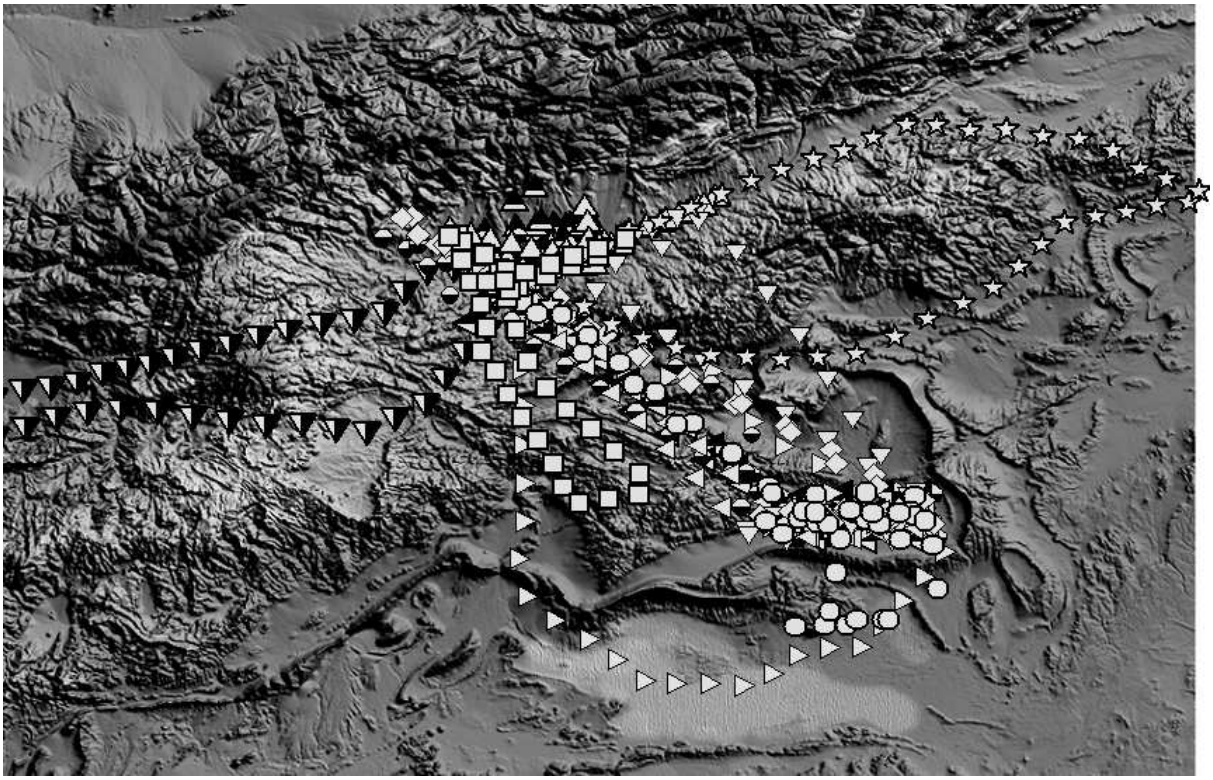

Figure 3.9: Overview of the 13 Partenavia flights during the SAMUM campaign in Morocco. 19 May 2006 — squares, 20 May — pentagons, 21 May — half-filled triangles up, 24 May — half-filled triangle down, 25 May — half-filled triangle left, 27 May — circles, 28 May — open triangles right, 30 May — asterisks, 2 June — half-filled circles, 3 June — open triangles left, 4 June — open triangles up, 5 June — open triangles down, 6 June — open diamonds.

For radiative-transfer modelling, information about the meteorological and aerosol conditions in the atmosphere are required. It was one of the advantages of the SAMUM experiment that such information was available from different instruments.

The vertical profile of the meteorological parameters temperature, pressure, and humidity has been obtained from daily radiosonde launches at Ouarzazate by the IfT lidar team (Ansmann *et al.*, 2009; Tesche *et al.*, 2009). Vertical profiles of the aerosol extinction coefficient have been derived from lidar measurements of the *Po*rtable *Li*dar *S*ystem (POLIS) of the University of Munich (Heese *et al.*, 2009). POLIS was the most suitable of the lidar systems for the purposes of this work because it covers the lowest parts of the atmosphere (lower than the Partenavia flight level). On days when extinction-profile measurements from POLIS were not available, the dust-layer height obtained from measurements of the six-wavelength *B*ackscatter *E*xtinction lidar-*R*atio *T*emperature *H*umidity profiling *A*pparatus (BERTHA) of the IfT was used (Tesche *et al.*, 2009).

Near Tinfou in the Zagora basin (coordinates 30.23°N, 5.61°W), a number of instruments for measurements of optical properties of dust particles have been operated during SAMUM (Schladitz *et al.*, 2009). This work makes use of the single-scattering albedo and asymmetry parameter of the dust particles determined from measurements of the absorption and scattering coefficients as well as the size distribution at this station.

Phase	Period	Description
DP1	12–15 May	Dusty air from Algeria
IP1	16–21 May	Moderately dusty air from Algeria, local dry-convective dust plumes
DP2	22–27 May	High and variable AODs in a low-pressure system
IP2	28–30 May	Clean air from the South-West
DP3	31 May–7 June	Dusty air from the East

Table 3.4: Dust phases during SAMUM, according to Knippertz et al. *(2009). DP means Dust Phase, IP means Intermediate Phase.*

The AOD and its wavelength dependence (expressed by the Ångström parameter) was supplied by Müller *et al.* (2009) (measurements from the sun photometers operated at Ouarzazate airport) and by von Hoyningen-Huene *et al.* (2009) (measurements at the Tinfou station).

The variations of the dust conditions are described and divided into different dust phases by Knippertz *et al.* (2009). These phases are summarised in Table 3.4.

3.2.2 Measured and simulated irradiances

Downwelling irradiances measured by the SMART-Albedometer aboard the Partenavia aircraft have been compared with the output of the radiative transfer model. For this check, the input of the model is set to match the conditions of the measurement by using all available measured parameters. As an example, this comparison is shown for the "golden day" of the SAMUM experiment, 19 May, 2006. The vertical profiles (used in the model) of the aerosol extinction coefficient and of temperature, pressure, and humidity are shown in Fig. 3.10 and Fig. 3.11, respectively. The lidar profile shows that the dust layer has a sharp top boundary at 4 km above ground. Maximum extinction is found close to the surface and to the top boundary of the layer. From the radiosonde data we see that the top boundary of the dust layer coincides with a small temperature inversion and a sharp drop in humidity. The AOD at 500 nm in Ouarzazate during the time of the flight was 0.41 with an Ångström exponent of 0.26. The comparison between radiative transfer model and measurement is shown in Fig. 3.12. In the range between 415 nm and 1800 nm, the measured and the modelled irradiance agree with each other within the limits of the measurement uncertainty — with the exception of the oxygen and water-vapour absorption bands.

The deviations in the water-vapour absorption bands result generally from low radiation levels and a particularly high sensitivity to the uncertainty of the radiosonde humidity data[6]. These bands have therefore have been excluded from further analysis. The larger deviations below 450 nm and above 2100 nm are caused the transmission properties of

[6]The uncertainty of the humidity sensor of Vaisala radiosondes is given as 5 % RH (relative humidity) by the manufacturer. In addition, the humidity may differ spatially and temporally between the radiosonde path and the aircraft location

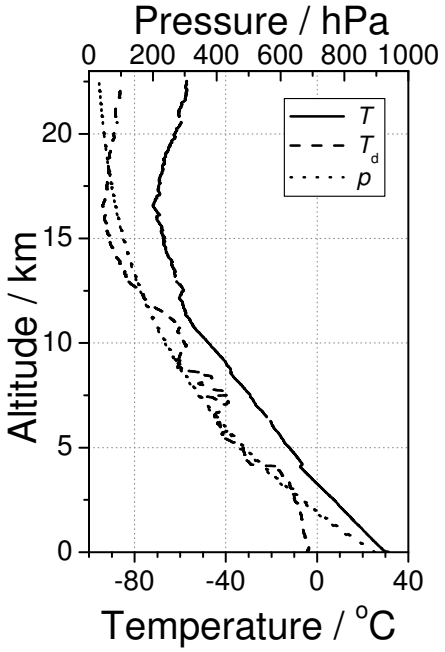

Figure 3.10: Radiosonde profile of temperature T, humidity (dewpoint T_d) and pressure p of 19 May, 2006, launched at 10:38 UTC. These data were provided by Dietrich Althausen and Matthias Tesche, IfT Leipzig.

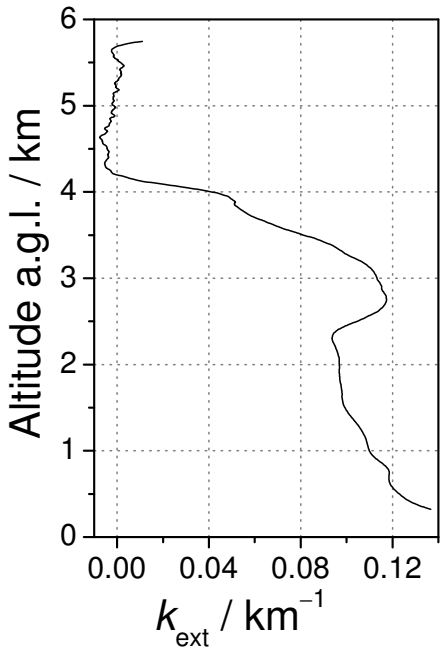

Figure 3.11: Vertical profile of the aerosol extinction coefficient k_{ext} on 19 May, 2006, measured by POLIS. These data were provided by Birgit Heese, University of Munich.

the optical fibres and the lower sensitivity of the spectrometer photodiodes at the edges of their spectral range. This leads to very low measurement signals that are dominated by noise. The observed irradiance mismatch and noise below 400 nm, is a calibration consequence of dividing the lamp spectrum (which is weak at those wavelengths) by the measurement signal that is also weak and fluctuates around zero(!). This results in a noisy ratio and therefore in noisy calibration factors below 400 nm.

Fig. 3.13 shows the measured irradiance spectra at two altitudes in the dust plume of 3 June, 2006, in the Zagora basin, in comparison to the result of the radiative transfer model. The vertical profile of the aerosol was only available at Ouarzazate airport, where the lidars were installed. Differences between the aerosol profile in Ouarzazate and the actual aerosol profile in the Zagora basin lead to differences between the model (which uses the Ouarzazate data) and the measured irradiances. These differences partly exceed the measurement uncertainty of the irradiance in wide spectral ranges even outside the gas absorption bands, especially at a flight altitude of 2710 m above ground (790 m below the assumed dust-layer boundary) where only the spectral range between 415 nm and 715 nm of the model output agrees with the measurement within the uncertainty range. At a lower flight level (360 m above ground), deeper inside the dust plume, the error in the assumed dust-layer height is less important, and in most spectral regions (except the

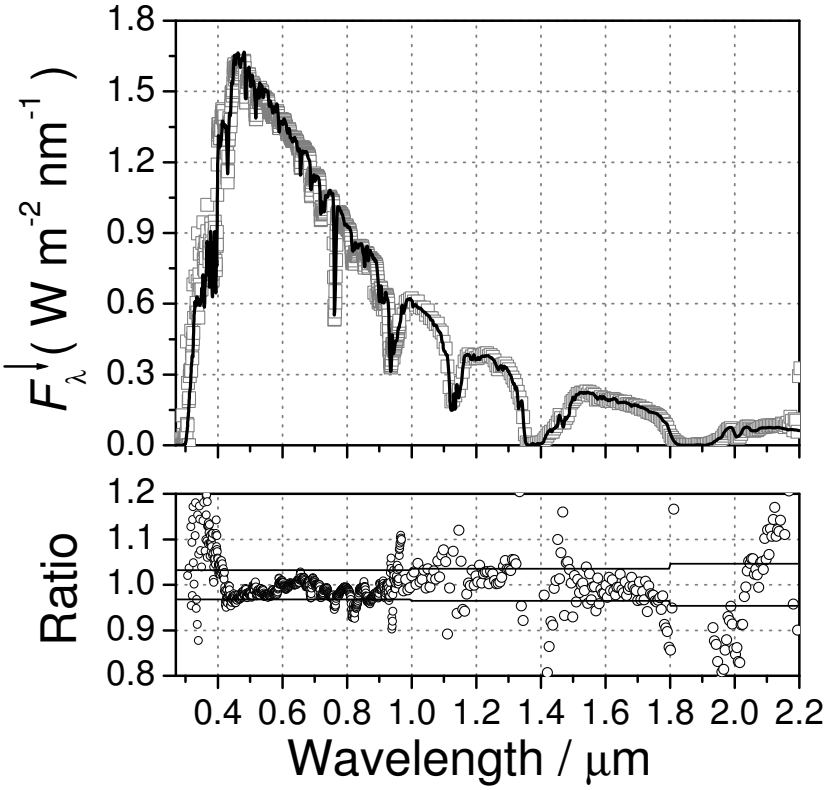

Figure 3.12: Measured (open symbols, gray) and modelled (solid line) downwelling irradiance for the first Partenavia flight on 19 May, 2006, at 10:50 UTC. The lower panel shows the ratio between measurement and model result (grey circles) and the measurement uncertainty range (solid line).

gas absorption bands) the model results agrees with the measured irradiance within the measurement uncertainty limits.

3.3 Radiative transfer model

A radiative transfer model was used to simulate the atmospheric radiation field. Calculations have been performed with the software package *libRadtran*, described by Mayer and Kylling (2005). The radiative transfer equation is solved by the Discrete-Ordinate method in the plane-parallel DISORT2 algorithm by Stamnes *et al.* (1988). For gas absorption the parametrisation SBDART/LOWTRAN by Ricchiazzi *et al.* (1998) was selected. *libRadtran* uses input data of the atmosphere, surface properties, and extraterrestrial radiation to calculate radiation quantities at arbitrary altitudes within the atmosphere.

The *libRadtran* software can be supplied with measured input parameters, if available. Data for which measurements are unavailable are replaced by standard assumptions. The model input can best be explained by an example input file:

```
solar_file /data/solar_flux/NewGuey2003_AlbedoWavelengths.dat
```

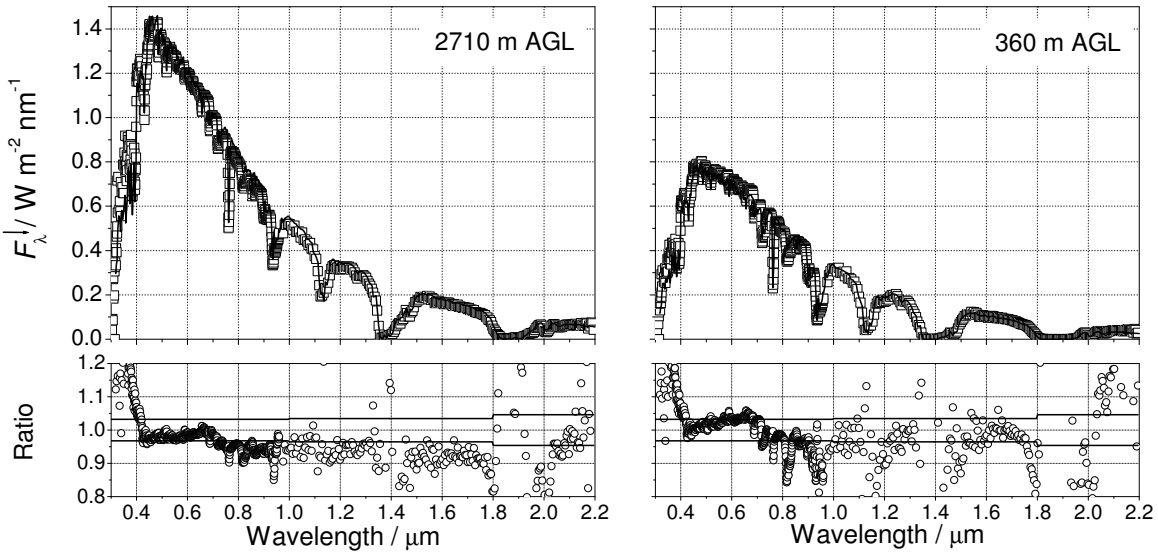

Figure 3.13: The measured (squares) and modelled (solid line) downwelling irradiance at two altitudes, 2710 m and 360 m above ground level (AGL), within the dust layer in Zagora basin. The lower panels show the ratio between measurement and model result (squares) in comparison to the measurement uncertainty of the irradiance (solid line). The dust-layer height used as input to the radiative transfer model is 3.5 km AGL.

```
atmosphere_file /data/atmmod/Atm_RS20060519_lidar_altitudes.DAT
albedo_file /data/SAMUM/Flug_190506/assumed_albedo/it_1_sod_36900.dat
wavelength 316 970
aerosol_files /data/aerosol/SAMUM_POLIS_20060519.layers
ozone_column 292.000
sza 31.1179
day_of_year 139
zout 0 0.312
output_user lambda zout eglo eup
rte_solver disort2
correlated_k LOWTRAN
slit_function_file /data/Gauss_fwhm2.5.dat
```

In the first line, the extraterrestrial solar irradiance is determined by the `solar_file` command. The grid of the specified file determines the wavelength grid and the radiometric unit of the model output. For this work, the spectral data published by Gueymard (2004) has been interpolated to the wavelength grid of the SMART-Albedometer.

The second line defines the file that contains the atmospheric information. The file name `RS20060519` indicates that the data have been derived from the radiosonde (`RS`) launch on 19 May, 2006. These measurements have been combined with the standard *libRadtran* atmosphere profile file (mid-latitude summer). The measured parameters have been interpolated to the vertical grid points of the model atmosphere. These parameters

are air pressure, temperature, and water-vapour density. The air-density profile is derived from pressure and temperature. The remaining parameters that a *libRadtran* atmosphere file must contain are the densities of ozone, oxygen, carbon dioxide, and nitrogen dioxide. The standard profiles (from the mid-latitude summer-conditions atmosphere of Anderson *et al.*, 1986) are scaled to match the profile of the air density. The ozone profile is scaled to match satellite measurements of the columnar ozone concentration (obtained from the Ozone Measurement Instrument, OMI).

The third command gives the user the opportunity to specify the file that contains the spectral surface albedo.

The `wavelength` command specifies the wavelength range (in nm) of the calculation (in this example, a portion of the spectral range of the VIS spectrometer).

The following line (`aerosol_files`) provides the location of the file in which the aerosol layering is described. In this example, a vertical aerosol profile from a lidar measurement on 19 May, 2006, is used. In cases when lidar data are not available, this line can be replaced by commands that specify the aerosol properties. As a starting point, *libRadtran* provides a default aerosol that contains a rural-type aerosol in the boundary layer, background aerosol above 2 km, spring-summer conditions and a visibility of 50 km. Any aerosol parameter (AOD, single-scattering albedo, asymmetry parameter, Ångström parameters) can be overwritten by additional data, e.g.:

```
aerosol_default
aerosol_set_tau 0.5        # AOD for all wavelengths
aerosol_angstrom 0.2 0.5   # Angstrom parameters alpha=0.2, beta=0.5
aerosol_set_gg 0.9         # Set g to 0.9
aerosol_scale_ssa 0.9      # Scale single-scattering albedo
                           #             by a factor of 0.9
```

Next, the columnar ozone concentration is given. These data are obtained from satellite measurements of the Ozone Monitoring Instrument (OMI). The value is given in Dobson units.

The `sza` and `day_of_year` commands give the geometric description of Sun and Earth — the solar zenith angle (in degrees), which has been previously calculated for the given time, date, and geographic location, and the day of the year (139 corresponds to 19 May) which is used to scale the extraterrestrial solar irradiance in dependence on the actual Sun-Earth distance.

The `zout` command determines the altitude above ground (in km) for which the model output shall be stored. For the purposes of this work, this is usually the surface (0) and the flight altitude (here, 312 m). For TOA calculations, `zout` is set to the maximum of the atmospheric profile (120 km). The `output_user` command specifies which quantities are requested. Here, we ask for the output table to contain columns of wavelength (`lambda`), altitude (`zout`), global downwelling (`eglo`) and upwelling irradiance (`eup`).

With the `rte_solver` and `correlated_k` commands, *libRadtran* is told to use the DISORT2 model to solve the radiative transfer equation, and to use the LOWTRAN parametrisation of gas absorption. Other possible choices of parametrisations either do not cover the entire spectral range or are available only for broadband calculations. The

`slit_function_file` contains a normalised Gauss curve with a full width at half maximum (FWHM) of 2.5 nm. The output data is convoluted with this curve to match the spectral resolution of the spectrometers used in the experiments.

4 Spectral Surface Albedo Measurements during SAMUM

4.1 Correction of atmospheric masking

Airborne measurements of the upwelling irradiance detect a signal that contains two components: The *surface* signal that originates from the surface, but has interacted with the atmospheric layer between the surface and the aircraft, and an *atmospheric* signal that is due to scattering and absorption of solar radiation processes within the atmospheric layer without involvement of the surface. The overall modification of the irradiance within the atmosphere is referred to as *atmospheric masking*. For a derivation of the surface albedo from airborne irradiance measurements, the measured signal has therefore to be corrected for atmospheric masking. This correction is performed with an algorithm that has been introduced by Wendisch *et al.* (2004).

The working principle of this algorithm is shown in Fig. 4.1. It starts from an "initial guess" of the surface albedo and iteratively converges to the true surface albedo. The albedo at flight level is used as the "initial guess" input. Irradiances modelled at both altitudes (flight level and surface) are used to extrapolate the airborne measurements to the surface. Differences between the measured and the modelled upwelling irradiance are related to differences between the true surface albedo and that which has been assumed for the calculations. The output surface albedo is compared to the assumed surface albedo of this iteration, and if the difference exceeds a threshold value, the consecutive iteration step is started with the newly obtained albedo as input.

The first step of the algorithm is a validity check for each measured spectrum. For this purpose the downwelling irradiance at flight level is calculated and compared to the measurement. If agreement within the limits of uncertainty is not found, this spectrum is excluded from all further evaluation. One possible reason for disagreement are clouds, which are not included in the model but have a drastic impact on the irradiance. Hence this algorithm automatically includes a cloud-screening.

The algorithm is based on two assumptions: The downwelling irradiance is considered independent of the surface albedo; and the ratio of upwelling irradiance at the ground to that at flight level is the same for both measurement and calculation.

For the evaluation of the SAMUM data, typical numbers of iterations (until the requested convergence criterium is reached) lie between 2 and 20 for the 300–1000 nm range, while in the NIR range (1000–2200 nm) only 1–2 iterations are usually necessary.

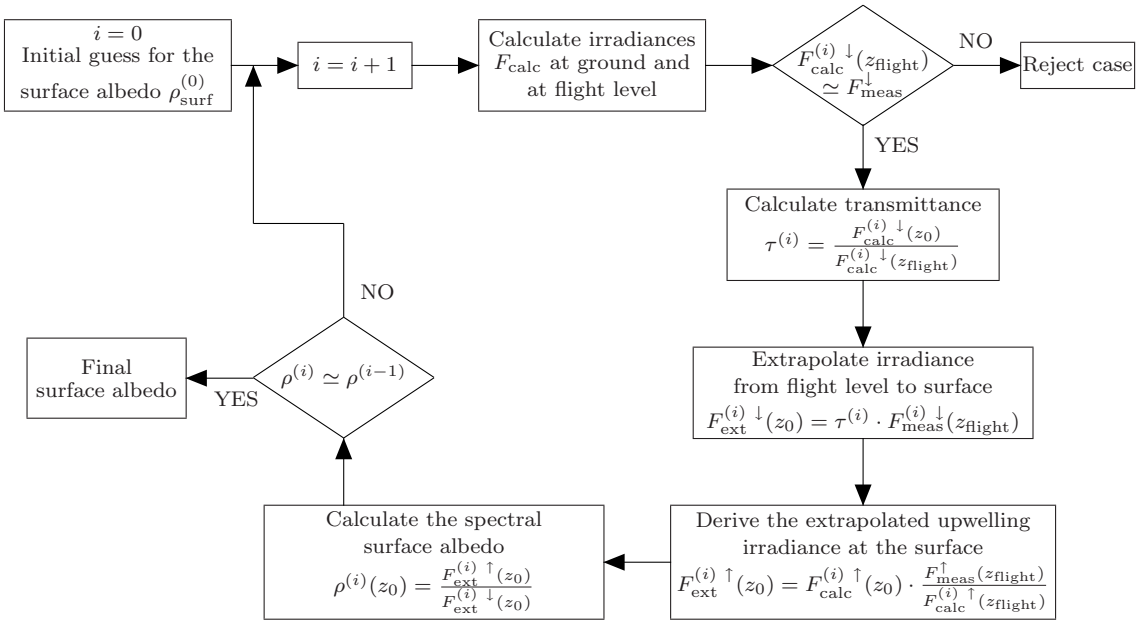

Figure 4.1: Flowchart diagram of the algorithm used for the derivation of the spectral surface albedo from airborne measurements of the upwelling and downwelling irradiance. Their ratio at flight altitude z_{flight} is taken as the "initial guess" $\rho_{\text{surf}}^{(0)}$. The algorithm calculates irradiances at flight altitude z_{flight} and at the surface z_0 and iterates until convergence is reached, i.e., the input and the resulting albedo do not differ from each other by more than a user-adjustable threshold. To assure good convergence, this threshold was set to 1 %.

Application to SAMUM data

Ideally, the algorithm requires a complete description of the optical properties of the atmosphere, at least of the layer between the aircraft and the surface. In practice, however, not all parameters are known individually for each aircraft location. In particular, the aerosol data (spectral AOD, extinction profiles) are available only at two locations — Ouarzazate and Tinfou —, while the aircraft has mostly been at more or less distant locations (up to 200 km from these locations). It has been generally observed during the SAMUM experiment that the aerosol layer often has a homogeneous vertical structure, but the horizontal variation of the AOD within the measurement area (as observed by MISR) was about 30 %. However, sensitivity studies show that these AOD variations lead to variations of the retrieved surface albedo of not more than 1 % (see Section 4.2). This justifies the use of the AOD point measurements from Ouarzazate and Tinfou for data processing of the entire flight track. If at certain locations the aerosol layer is much different to that at Ouarzazate or Tinfou, measurements are rejected for further analysis by the check of the downwelling irradiance at flight level.

In particular, the following SAMUM input parameters have been used to run the radiative transfer calculations:

Atmospheric profiles of pressure, temperature, and humidity have been obtained from daily radiosonde launches (Tesche *et al.*, 2009), scheduled at the take-off time of

each flight.

Ozone column concentrations are taken from the Ozone Monitoring Instrument (OMI) onboard the AURA satellite of the NASA EOS programme. The daily data are downloaded from the website http://acdisc.sci.gsfc.nasa.gov/Giovanni/omi/ .

The solar zenith angle is calculated for each data point using the time and the geographic coordinates from the navigation logs, using the `zenith` program of the *libRadtran* package.

Aerosol information is given to *libRadtran* piecewise, depending on how much is known. The wavelength dependence of the AOD can be given in terms of the Ångström parameters. These are derived from multi-wavelength AOD measurements by sun photometers at Ouarzazate airport (D. Müller et al., 2008) and at the Tinfou ground station (von Hoyningen-Huene *et al.*, 2009).

Scattering and absorption characteristics are determined by two parameters, namely the single-scattering albedo $\tilde{\omega}$ and the asymmetry parameter g. Both have been derived from continuous ground-based measurements in Tinfou (Schladitz *et al.*, 2009). The relevant data for each flight has been extracted from the entire dataset of 30-minute averages. g was derived at 450 nm, 530 nm, 550 nm, 630 nm, and 700 nm. $\tilde{\omega}$ was derived at 530 nm and 630 nm. The wavelength dependence of both parameters outside the measured wavelength range was adopted from Tegen *et al.* (1996) and d'Almeida *et al.* (1991).
The most complete aerosol information is included on those dates for which a lidar profile of the aerosol layer is available. For these cases, an external input file replaces the internal aerosol commands. This file contains the vertical and spectral behaviour of the aerosol extinction coefficient, the single-scattering albedo, and the phase-function coefficient (in terms of the asymmetry parameter). Only lidar profiles from the Portable Lidar System (POLIS) were used (Heese *et al.*, 2009), because the remaining lidar systems do not cover atmospheric layers lower than 2 km. POLIS operated in Tinfou on 26 and 27 May, otherwise in Ouarzazate.
The influence of humidity on the aerosol properties have been neglected. According to analyses of the Tinfou measurements by Kaaden *et al.* (2009), the dominating aerosol component is mineral dust which shows no hygroscopic growth even at humidity values close to saturation. A second anthropogenic component is present as background aerosol, mainly at diameters below 250 nm, which shows hygroscopic growth by a factor of up to 1.65 when it changes from a dry state of 85 % humidity. But on most days the optical properties were dominated by the mineral-dust fraction.

An overview over the aerosol parameters used for each flight day is given in Table 4.1. Lidar data from POLIS are available for 19 May and 3 June, replacing the tabulated data.

The algorithm was implemented as an IDL programme which processes the calibrated measurement data and runs the radiative transfer model by external calls to *libRadtran*. Instead of performing a *libRadtran* calculation for each measured spectrum, a number of spectra is grouped into blocks to reduce computation time. A block is defined as a sequence of datasets with similar environmental conditions: only small changes in surface

Flight Day	Ouarzazate Ångström		Tinfou Ångström		Single-Scattering Albedo $\tilde{\omega}$	Asymmetry Parameter g	Dust phase
	α	β	α	β			
19 May	0.250	0.321			0.95	0.69	IP1
20 May	0.197	0.506	0.528	0.383	0.94	0.69	IP1
21 May	0.236	0.377			0.93	0.69	IP1
24 May	0.165	0.321			0.95	0.70	DP2
25 May	0.060	0.491	0.119	1.114	0.95	0.70	DP2
27 May	0.088	0.450	0.161	0.679	0.96	0.70	DP2
28 May	0.138	0.324	0.383	0.370	0.96	0.70	IP2
30 May	0.684	0.041	1.010	0.093	0.90	0.67	IP2
2 June	0.250	0.198	0.296	0.504	0.95	0.70	DP3
3 June	0.134	0.478	0.176	0.786	0.96	0.70	DP3
4 June	0.175	0.372			0.96	0.70	DP3
5 June	0.214	0.273	0.431	0.304	0.95	0.69	DP3
6 June	0.223	0.433	0.450	0.355	0.94	0.70	DP3

Table 4.1: Aerosol parameters used for the atmospheric correction algorithm of the SAMUM data. AOD is described by Ångström parameters α and β (cf. Eq. 1.19) measured in Ouarzazate and Tinfou. Tinfou values are given only when the flight passed through that region. On 19 May and 3 June, lidar-derived aerosol profiles have been applied instead. $\tilde{\omega}$ and g values are given for $\lambda = 530\,nm$ and $\lambda = 550\,nm$, respectively. The dust phase according to Knippertz et al. *(2009) is indicated, cf. Table 3.4.*

terrain and SZA are allowed (maximum time span is five minutes; the allowed maximum change in surface elevation is 20 %). When these thresholds are exceeded, this is defined as the end of the current block. The AOD is set constant to the values measured at Ouarzazate or Tinfou (whichever is closer to the aircraft location). $F^{\downarrow}$ is calculated once for this block for all occurring flight altitudes, and all spectra are flagged as to whether they match the calculated downwelling irradiance or not. Here the threshold is set to 10 %, i.e. higher than the measurement uncertainty, because the vertical profile of $\tilde{\omega}$ and g as well as the horizontal variability of the layer structure are not known. In the next step, the atmospheric correction is calculated iteratively. For this, a certain set of flight altitudes is chosen that covers the entire flight-altitude span of this block in regular steps. The atmospheric correction factors are calculated only at these chosen flight altitudes. They are then exponentially interpolated to all remaining flight altitudes and applied to the corresponding datasets. This procedure does not introduce significant additional errors because the altitude differences are small (this is warranted by the definition of a block) and because the measured aerosol profiles are generally smooth within the corresponding atmospheric sublayer. With this procedure, the computing time is drastically reduced (by a factor of up to 20). Nevertheless, the processing of one measurement flight still takes 2–3 days computation time.

Certain wavelength regions have been excluded from the surface-albedo analysis for different reasons. First, strong spectral irradiance gradients on the edges of gas absorption bands deteriorate the data quality because of errors made during several interpolation steps that are necessary in the evaluation process. Small differences between the wavelength grids of the two NIR spectrometers and possible inaccuracies in modelling the gas absorption have severe consequences in the retrieval when the gradient is strong. The obtained surface-albedo spectra are not usable due to severe noise in those spectral regions. Second, there are water-vapour absorption bands around 1350 nm and 1900 nm where irradiance in the lower troposphere is entirely attenuated. Under the absence of radiation at these wavelengths, a measurement of the surface albedo is not only impossible, but also meaningless[1].

The following wavelength bands have been excluded from the surface-albedo results: Because of strong spectral slopes: 750–775 nm (oxygen absorption), 930–1008 nm (water vapour), 1099–1177 nm (water vapour). Because of total attenuation: 1320–1490 nm and 1775–1950 nm (both water vapour).

In addition, the spectral range below 317 nm has been excluded because of low irradiance levels which leads to noise in their ratios. Apart from the dark-signal noise of the spectrometers which has a stronger impact for weak signals, calibration is a problem at these small wavelengths because of the low signal output of the calibration lamp. Similar considerations apply for the spectral range above 1950 nm, but the resulting noise levels are lower there.

4.2 Uncertainty of surface-albedo measurements

The surface albedo is subject to two sources of uncertainty: First, the measurement uncertainty of the irradiances measured by the SMART-Albedometer, which has been estimated in Subsection 2.8. Second, the uncertainty of the different aerosol parameters that are included into the retrieval algorithm. For a quantification of the latter, a series of sensitivity studies has been performed. The retrieval algorithm has been executed repeatedly with varying input parameters. In particular, the AOD, the aerosol single-scattering albedo and asymmetry parameter, and the flight altitude have been varied in the model. The range of variation has been chosen to reflect the variations of the measured parameter on 19 May either with time or with space: The single-scattering albedo and the asymmetry parameter have been measured at a fixed location in Tinfou, and varied during the day (by less than 5 % each), while for the AOD its geographical variation in the measurement area as observed by MISR (around ±30 %) has been taken into account. For the flight altitude, an uncertainty of ±30 m has been assumed. The study (cf. Fig. 4.2) showed that all parameters have the strongest influence in the lowest part of the spectrum (below 600 nm). For longer wavelengths, the algorithm is more stable with respect to variation of the input parameters. This agrees with the observation of a much faster convergence of the algorithm for the NIR data.

[1] as long as only natural radiation is investigated.

Error	I	II	III	IV	V
$F^{\downarrow}$	3.2 %	3.2 %	3.2 %	3.5 %	4.6 %
$F^{\uparrow}$	3.2 %	3.2 %	3.2 %	3.5 %	4.6 %
$\tilde{\omega}$	1.2 %	0.8 %	0.5 %	0.5 %	0.5 %
τ	0.8 %	0.8 %	0.2 %	0.2 %	0.2 %
g	6 %	1.5 %	0.3 %	0.3 %	0.3 %
h	4 %	0.5 %	0.2 %	0.2 %	0.2 %
Total	**8.6 %**	**4.9 %**	**4.6 %**	**5.0 %**	**6.5 %**

Table 4.2: Uncertainties of the retrieved surface albedo, a Gaussian combination of the irradiance uncertainty and the variability of the surface-albedo extrapolation algorithm when different input parameters are varied. The spectral range from 317 nm to 2200 nm has been divided into five intervals (I–V). I: 317–400 nm. II: 400–600 nm. III: 600–1000 nm. IV: 1000–1800 nm. V: 1800-2200 nm.

A variation of the AOD of ±30 % gives rise to a variation of the retrieved surface albedo of ∓1 % for wavelengths below 600 nm, and no more than ±0.2 % above 600 nm. A variation of the aerosol single-scattering albedo by 5 % yields a surface-albedo uncertainty of 1.2 % at 350 nm which decreases to 0.4 % at 2200 nm. The measured range of the asymmetry parameter g at the Tinfou station is between 0.67 and 0.72. However, these are measurements at the surface where a large number of coarse aerosol particles are present. At higher altitudes, there are less large particles. Therefore, g has been set to 0.75 in the calculations. Assuming a maximum uncertainty of g by 10 %, the corresponding surface-albedo uncertainty amounts to values between 6 % and 2 % from 300 nm to 400 nm, between 2 % and 0.5 % from 400 nm to 600 nm, and less than 0.5 % for longer wavelengths. Changing the flight altitude in the calculations by ±30 m leads to surface-albedo changes of ±4.5 % at 350 nm, ±1 % at 400 nm and < 0.2 % for longer wavelengths (with the exception of the edges of water-vapour absorption bands).

The assumed variations of the different influential parameters are assumed to occur independently. Therefore, their uncertainty contributions are summed up using Gaussian combination (Table 4.2). The resulting uncertainty of the extrapolated surface albedo lies between 4.6 % and 5.0 % in most parts of the spectral range. For wavelengths above 1800 nm it is determined as 6.5 %, and below 400 nm as 8.6 %.

4.3 Typical surface-albedo spectra

Different surface types have been covered in the 13 measurement flights. Most of the terrain in the Ouarzazate and Zagora basins is a brown-red stone desert, which is also called *hamada*. Furthermore, a number of oases, especially in the valleys of Rivers Drâa and Dadès, have been overflown, as well as the dry lake Iriki lake with its salt crust near the Algerian border. The typical surface-albedo spectra are presented in Fig. 4.3. The surface albedo has not been derived for the flight on 25 May, because the AOD was extremely high on this day, so that the surface was often not visible from the aircraft and thus the

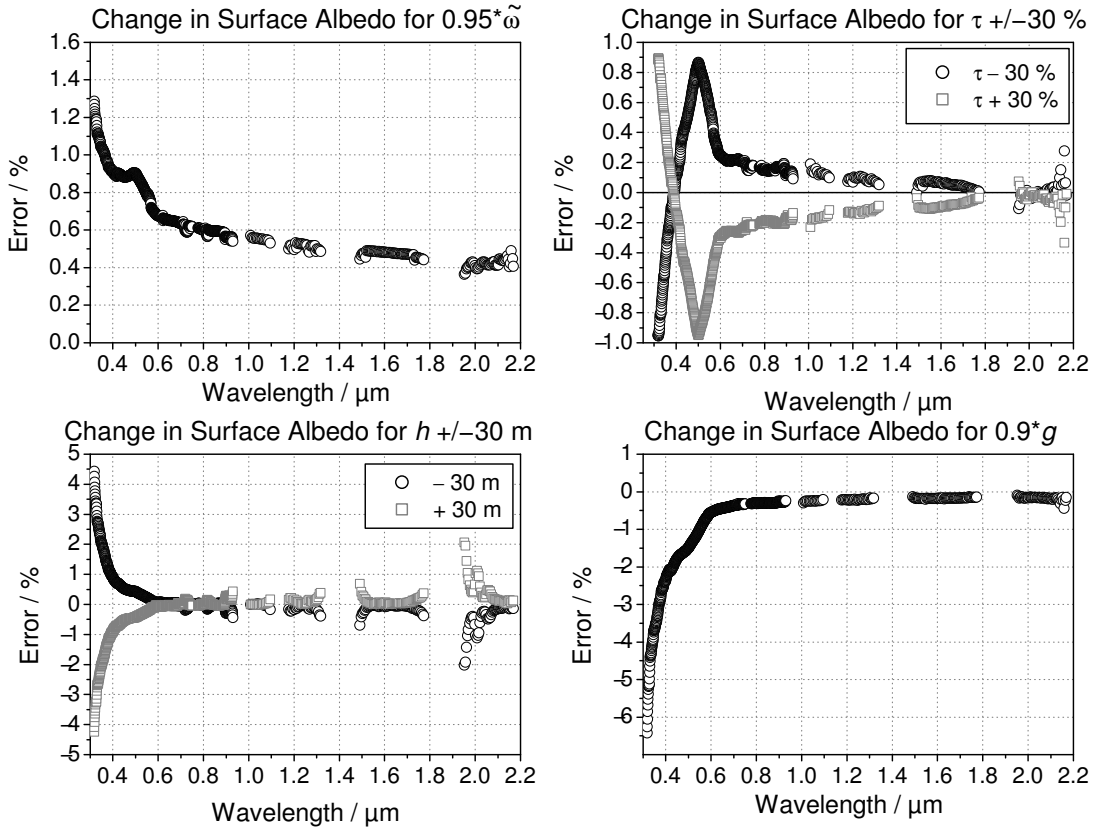

Figure 4.2: Results of a series of sensitivity studies for the surface-albedo retrieval algorithm with respect to the atmospheric input parameters. These parameters are the aerosol single-scattering albedo $\tilde{\omega}$, the aerosol optical depth τ, the aerosol asymmetry parameter g, and the flight altitude h.

non-linear extrapolation algorithm could not be applied.

The most prominent type of surface-albedo spectra in the experiment region is the smooth type with little features, typical for the hamada ground. This hamada spectrum (Fig. 4.3*a*) shows an increase of surface albedo throughout the visible spectral range, from values well below 0.05 in the ultraviolet to values around 0.2–0.3 at 900 nm. This includes an enhancement of the red wavelength range (600–800 nm). At wavelengths above 800 nm, a plateau is observed up to 2200 nm with small slope which is mostly slightly positive but in a few cases also slightly negative.

When flying over vegetation in the oases (Fig. 4.3*b*), characteristic changes occur in the surface-albedo spectrum: A strong step around 700 nm, the so-called vegetation step (or red edge), appears. This enhanced reflection is a natural protection against plant damage caused by NIR radiation and has already been discussed for the Brandis data in Section 3.1.2. As now also the NIR range is available, we see that it is accompanied by

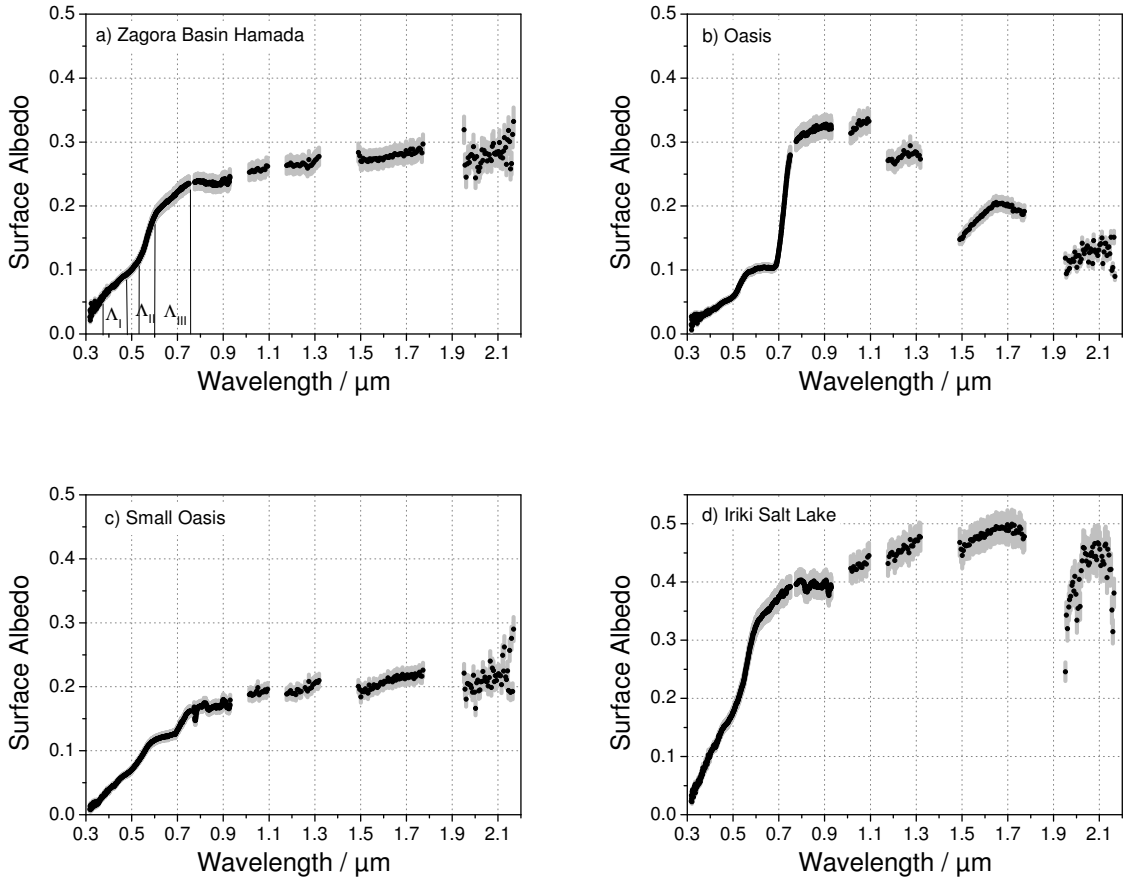

*Figure 4.3: The most important examples of SAMUM albedos (black symbols). The range of the measurement uncertainty (cf. Section 4.2) is shown in grey. Figure 4.3*a *shows a typical surface-albedo spectrum of the red stone-desert (hamada) surface measured in the Zagora basin. The same type of spectrum was found in many parts of the Ouarzazate basin. Figure 4.3*b *is a typical vegetation spectrum of an oasis in the Dadès valley. Figure 4.3*c *was measured over a small oasis in the Atlas mountains with plenty of surrounding hamada in the field of view: even though the spectral shape is dominated by that of barren ground, it clearly shows the vegetation step at 700 nm. Figure 4.3*d *is the surface-albedo spectrum of the dry Iriki salt lake where the hamada is covered by a salt layer formed by the evaporation of the River (or rather* wadi*) Drâa.*

an almost stepwise decrease of the surface albedo between 1000 nm and 2200 nm . This is due to the leaf water content, but also to absorption of incident radiation by liquid surface water. Water exhibits low levels of reflection.

A mixture of these two types of surface-albedo spectra is shown in Fig. 4.3*c*. In this case, the aircraft was above a small oasis on the edge of the Atlas mountains. The field of view was dominated by barren ground, and in consequence the surface-albedo spectrum is dominated by the shape of the hamada spectrum. However, the vegetation step, albeit small, is clearly visible around 700 nm, showing the high sensitivity of the surface albedo to the presence of vegetation in otherwise unvegetated areas.

Fig. 4.3*d* shows an extreme case of the hamada-type surface-albedo spectrum. These data have been collected while flying above the Iriki salt lake. This is a vast, flat dry area of hamada to the south of the Zagora basin, where the rock surface is covered by layers of salt that have been formed by the evaporation of the River Drâa. This area is a bright spot clearly visible from space, with surface albedo reaching values around 0.4 in the red (700 nm) and up to 0.5 around 1.7 μm.

The hamada-type surface-albedo spectrum has a characteristic shape that is made up of three almost linear spectral intervals. These intervals are Λ_{I}=[390 nm, 490 nm], Λ_{II}=[520 nm, 600 nm], and Λ_{III}=[600 nm, 750 nm]. The slope of the surface albedo in these intervals is denoted as $\mathrm{S_I}$, $\mathrm{S_{II}}$, and $\mathrm{S_{III}}$. It appears that $\mathrm{S_{III}}$ is generally similar to $\mathrm{S_I}$, while $\mathrm{S_{II}}$ is larger. This is confirmed by the according histograms derived from the data of 19 May (Fig. 4.4). In 54 % of all cases, the ratio between $\mathrm{S_{III}}$ and $\mathrm{S_I}$ is 1 ± 0.25, while it is larger, 1.5 ± 0.25, in 41 %. That is 95 % with a ratio between 0.75 and 1.75, with the average ratio being 1.22.

The ratio between $\mathrm{S_{II}}$ and $\mathrm{S_I}$ falls between 2.25 and 3.25 in 84 % of all cases, with an average ratio of 2.70. And the ratio between $\mathrm{S_{III}}$ and $\mathrm{S_{II}}$ is 0.5 ± 0.25 in 99.7 % of all cases. The coefficient of determination for a linear fit of one slope to another is: $\mathrm{S_{III}/S_I}$: 0.71, $\mathrm{S_{II}/S_I}$: 0.84, $\mathrm{S_{III}/S_{II}}$: 0.90.

These numbers imply that the spectral shape of the surface albedo in general varies only little over the flight path. This is not, however, a restriction of the variations of the magnitude of the surface albedo.

For further analysis of the data from the flight, two spectral indices are used. First, the Normalized Difference Vegetation Index (*NDVI*), which has been introduced in Eq. 3.2, is calculated as

$$NDVI = \frac{\rho_{900} - \rho_{645}}{\rho_{900} + \rho_{645}} \tag{4.1}$$

where ρ_x is the surface albedo at a wavelength of x nm. As explained in Section 3.1, the *NDVI* is well established for the detection of vegetation. As most of the surface in the measurement area has little or no vegetation, such a vegetation-based index cannot be expected to serve as a sufficient measure for surface variability. Therefore, I introduce a similarly defined Normalized Difference Red-Colour Index *NDRI* defined as

$$NDRI = \frac{\rho_{600} - \rho_{520}}{\rho_{600} + \rho_{520}} \,. \tag{4.2}$$

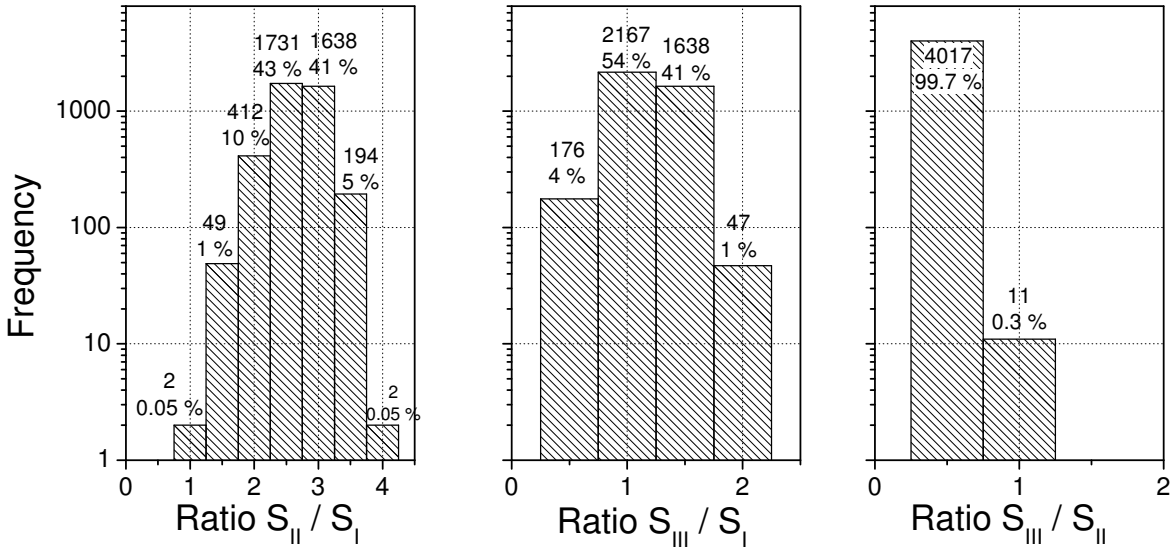

Figure 4.4: Histograms showing the ratio between the slopes S of the spectral regions Λ_{I}*=[390 nm, 490 nm],* Λ_{II}*=[520 nm, 600 nm], and* Λ_{III}*=[600 nm, 750 nm] for the hamada-type (i.e., NDVI<* 0.2*) surface albedo measured on 19 May, 2006. Bin size is 0.5.*

The *NDVI* analyses the vegetation step at 700 nm, and the *NDRI* takes a similar look at the red-colour step below 600 nm and differentiates different shades of red. Both indices for the data of 19 May are shown in Fig. 4.5 (upper left panel), together with typical plots of the corresponding surface-albedo spectra for the different *NDVI*/*NDRI* regions. In general, there is a high variability in *NDRI* but not in *NDVI*. Only 1.6 % of the measured spectra on 19 May have an *NDVI* of higher than 0.2, i.e. are dominated by vegetation beneath the aircraft (see the histograms in Fig. 4.6). The vegetation step is visible in a surface-albedo spectrum when the *NDVI* is at least 0.1. About two thirds of the surface-albedo spectra on 19 May fulfil this criterium, but most of these show a higher variation in *NDRI* than in *NDVI*, and only 7 % of them have an *NDVI* of more than 0.15. 31 % of all spectra have definitely no vegetation contribution (*NDVI* less than 0.1).

A similar analysis for all measurement flights is summarised in Table 4.3. Their *NDVI* and *NDRI* scatter plots are shown in Fig. 4.7 and Fig. 4.8. Often, but not always, the variability in *NDRI* is larger than that in *NDVI*. Regions when the aircraft was above oases are easily identified by peaks of high *NDVI*, especially on 20, 27, 28, and 30 May, and on 6 June. A peak of negative *NDVI* on 5 June stems from a water surface (a reservoir near Ouarzazate).

For comparison, *NDVI* and *NDRI* have been calculated for the desert-type surface albedo spectra from literature which are shown in Fig. 1.2. They are:

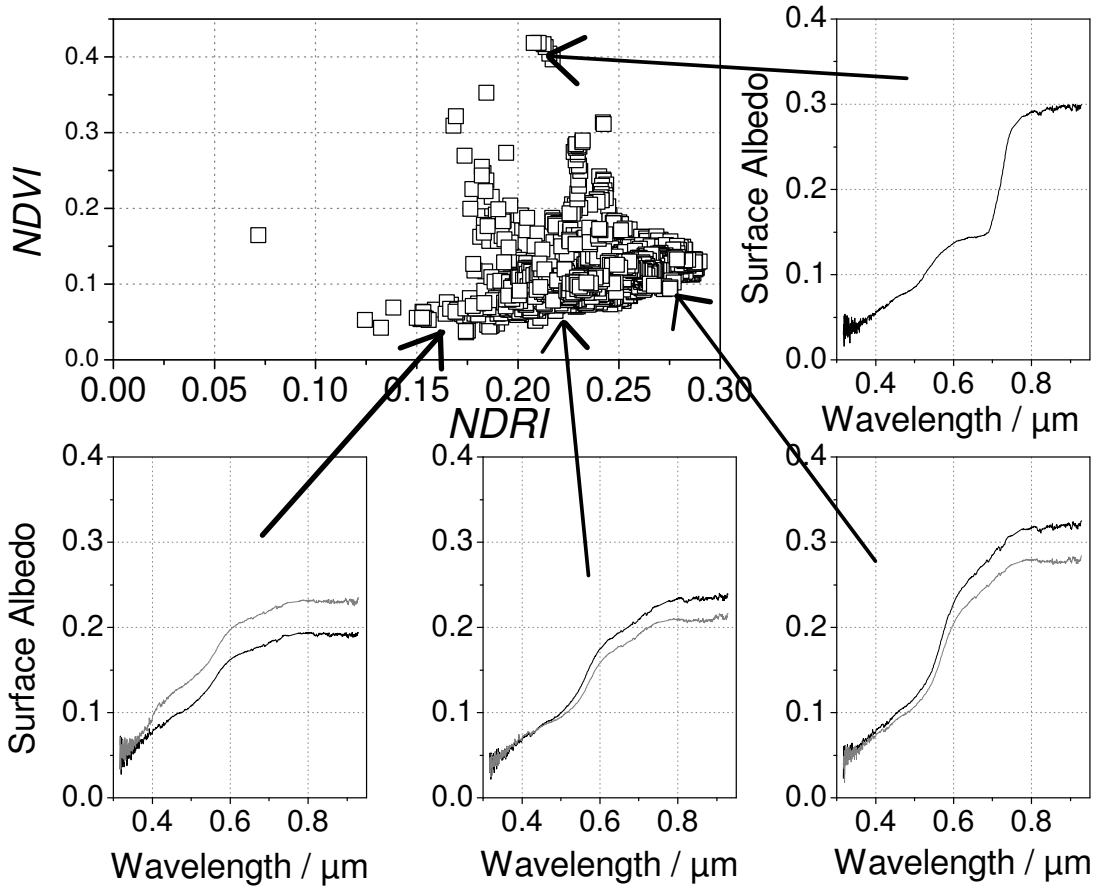

Figure 4.5: Scatter plot of spectral indices NDRI and NDVI (see text) for the measurement flight on 19 May, 2006 (upper left panel). Typical surface-albedo spectra for the different NDVI/NDRI regions are shown: High NDVI (upper right), low NDVI and NDRI of less than 0.2 (lower left), between 0.2 and 0.25 (lower central), and more than 0.25 (lower right).

Type	***NDVI***	***NDRI***
Bowker	0.16	0.48
Koelemeijer	n/a	0.18
Sinai	0.10	0.15
Taklimakan	0.07	0.17
Moon	0.11–0.17	0.08
SAMUM	**0.09**	**0.25**

The desert spectrum of Koelemeijer *et al.* (2003) does not include 900 nm, so the *NDVI* could not be calculated. Nor does the lunar spectrum, but an extrapolation of the almost linear spectrum has been attempted and yielded 0.17 for a linear extrapolation, and 0.11 for the surface albedo at 900 nm set equal to that at 800 nm (so those two values can be considered the limits of the most probable range). *NDVI* values are generally below 0.2, as all spectra stem from desert areas, but the example of the moon shows that an *NDVI* between 0.1 and 0.2 can be obtained without the least trace of vegetation, and should

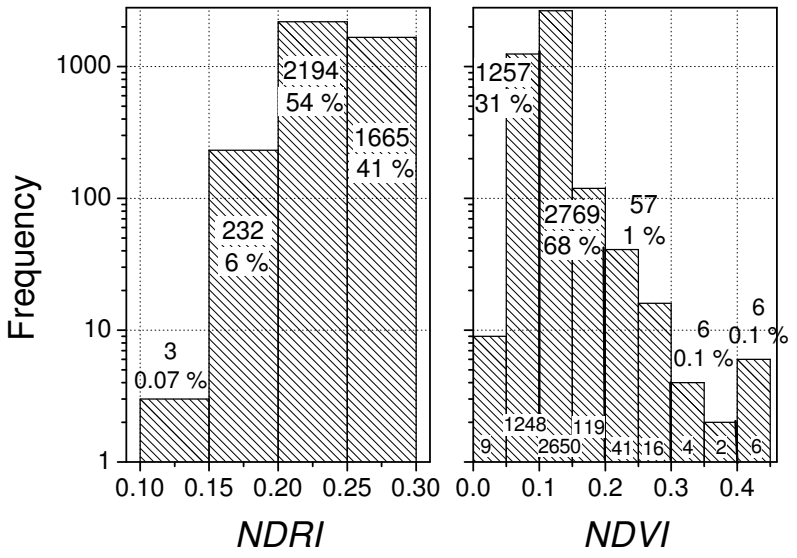

Figure 4.6: Histogram showing the occurence frequency of NDRI (left) and NDVI (right) on 19 May, 2006. Bin size is 0.05. Additionally, percentages for bins of 0.1 width are shown for NDVI.

therefore be treated with caution in interpretation attempts. The *NDRI* is well below the SAMUM average of 0.25 for all spectra except for the Utah sample of Bowker *et al.* (1985) where almost the double value is reached. In fact, photographs from that region (e.g., at `http://www.americansouthwest.net/utah/monument_valley/`) resemble the landscape in south-eastern Morocco, but with an obviously more intense red colour compared to the rather brownish red in the SAMUM region.

NDVI and *NDRI* are not entirely independent for the typical hamada surface-albedo spectrum. Spectra with higher *NDRI* also have a higher *NDVI* than those with low *NDRI*. That is because the *NDVI* is slightly sensitive to changes in surface albedo even of areas without vegetation. The *NDVI* wavelengths 645 nm and 900 nm are influenced by the hamada spectral slope in Λ_{III} which extends up to 750 nm. This hamada slope S_{III} is strongly connected to that in the lower spectral region Λ_{II} (see Fig. 4.4) where the *NDRI* is calculated.

4.4 Comparison with satellite data

During the experimental SAMUM period, four overpasses of the TERRA satellite took place, one of them was disturbed by clouds. The *Multi-Angle Imaging SpectroRadiometer* (MISR) onboard TERRA was programmed to operate in local mode for these overpasses, i.e. to transmit full-resolution data.

The surface-albedo product of MISR (referred to by NASA as Bihemisherical Reflectance, BHR) can be downloaded from the internet (dataset MIL2ASLS) and is supplied at a resolution of 1100 m. MISR data points are geographically referenced as follows:

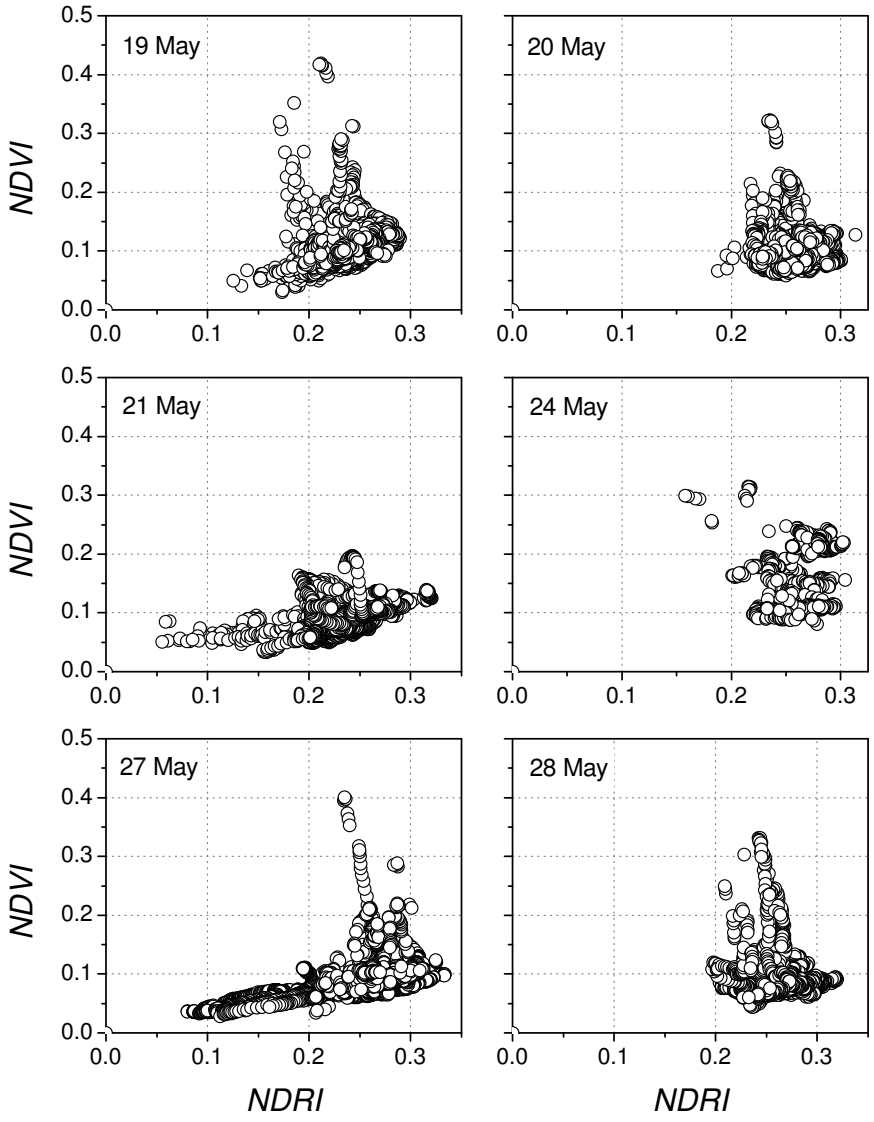

Figure 4.7: Histograms showing the distribution of NDVI and NDRI for all measurements flights from 19 May to 28 May, 2006.

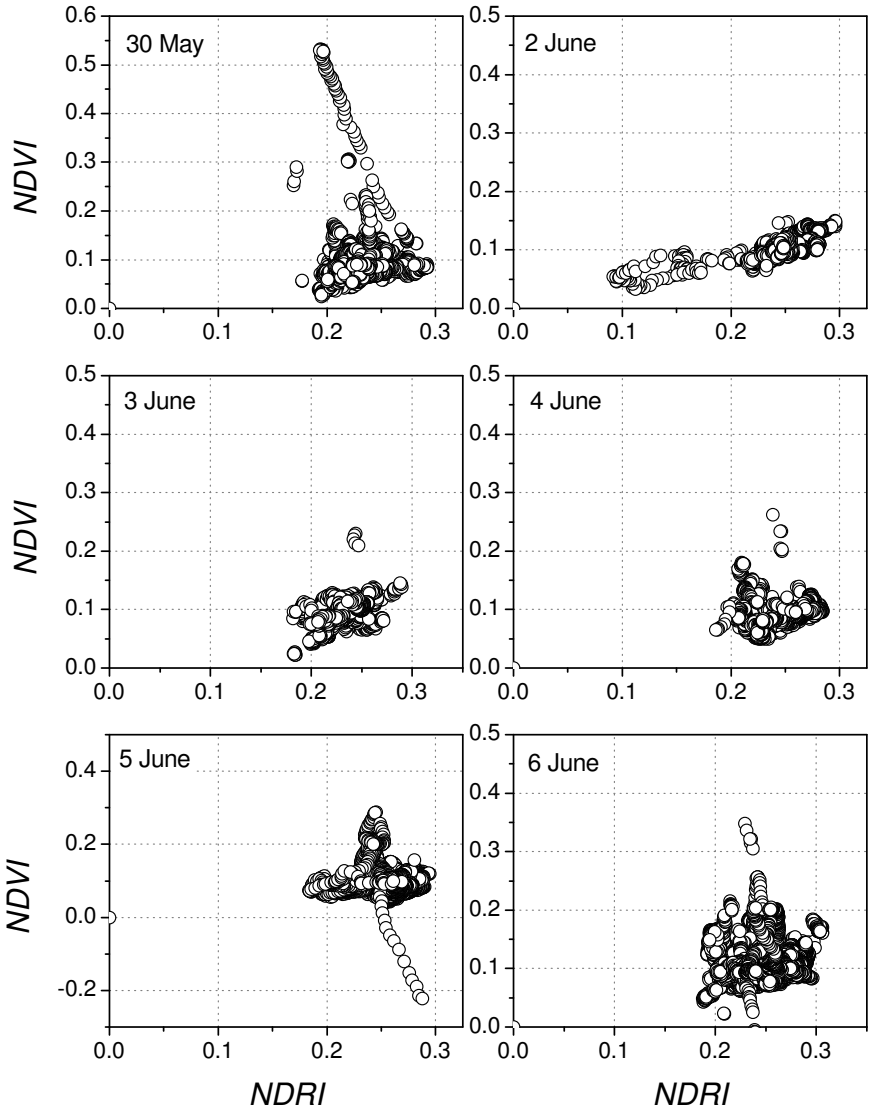

Figure 4.8: Histograms showing the distribution of NDVI and NDRI for all measurements flights from 30 May to 6 June, 2006.

Day	$\overline{\rho_{500}}$	$\overline{\rho_{672}}$	$\overline{\rho_{900}}$	$\overline{NDVI}$	$\overline{NDRI}$	$\overline{S_{\mathrm{II}}/S_{\mathrm{I}}}$	$\overline{S_{\mathrm{III}}/S_{\mathrm{I}}}$	$\overline{S_{\mathrm{III}}/S_{\mathrm{II}}}$	$NDVI > 0.2$	N
19 May	0.10 ± 0.04	0.20 ± 0.09	0.24 ± 0.11	0.11	0.24	2.70 ± 0.74	1.22 ± 0.57	0.45 ± 0.22	1.61 %	4094
20 May	0.09 ± 0.03	0.19 ± 0.07	0.23 ± 0.09	0.10	0.26	2.58 ± 0.48	1.06 ± 0.40	0.41 ± 0.16	1.24 %	3792
21 May	0.10 ± 0.02	0.21 ± 0.06	0.24 ± 0.07	0.08	0.29	2.06 ± 0.64	0.75 ± 0.41	0.36 ± 0.12	0.00 %	5610
24 May	0.08 ± 0.04	0.18 ± 0.09	0.24 ± 0.11	0.15	0.26	2.37 ± 0.95	1.29 ± 0.52	0.56 ± 0.32	27.7 %	675
27 May	0.12 ± 0.09	0.24 ± 0.10	0.28 ± 0.13	0.08	0.24	2.06 ± 0.87	0.74 ± 0.54	0.35 ± 0.16	0.69 %	5693
28 May	0.10 ± 0.05	0.22 ± 0.11	0.25 ± 0.12	0.09	0.26	2.38 ± 0.52	0.90 ± 0.41	0.38 ± 0.17	1.41 %	5186
30 May	0.09 ± 0.03	0.18 ± 0.07	0.21 ± 0.08	0.09	0.23	2.39 ± 0.42	0.91 ± 0.78	0.38 ± 0.40	1.67 %	4480
2 June	0.09 ± 0.05	0.19 ± 0.13	0.23 ± 0.16	0.10	0.24	2.10 ± 0.74	0.84 ± 0.46	0.39 ± 0.13	0.00 %	926
4 June	0.10 ± 0.02	0.22 ± 0.06	0.25 ± 0.07	0.09	0.25	1.99 ± 0.44	0.78 ± 0.29	0.39 ± 0.12	0.21 %	2871
5 June	0.09 ± 0.03	0.20 ± 0.06	0.23 ± 0.07	0.09	0.26	2.21 ± 0.39	0.83 ± 0.37	0.37 ± 0.14	1.01 %	7187
6 June	0.10 ± 0.03	0.21 ± 0.07	0.26 ± 0.08	0.11	0.25	2.29 ± 0.54	0.84 ± 0.42	0.37 ± 0.16	0.95 %	8499
Total	0.10 ± 0.04	0.21 ± 0.08	0.24 ± 0.09	0.09	0.25	2.28 ± 0.57	0.88 ± 0.46	0.38 ± 0.18	1.32 %	49013

Table 4.3: Statistical overview of the surface albedo derived from the SAMUM flights. From left to right, the columns contain the mean spectral surface albedo at 500 nm, 672 nm, and 900 nm; the mean NDVI, the mean NDRI, and the mean slope ratios of hamada-type spectra; and finally the fraction of spectra for which NDVI exceeds 0.2, and the total number of spectra. The uncertainty values are twice the standard deviation along the flight. Spectra with an NDVI of more than 0.2 have not been taken into account for the calculation of the mean slope ratios to keep them free of vegetation influence.

Each orbit of the satellite is along one fixed path. The Moroccan city of Ouarzazate is within the field of view of MISR when the satellite is on path 200, 201, or 202. This condition was fulfilled on 19 May (path 201, orbit # 34136, 11:11 UTC[2]), 26 May (path 202, orbit # 34238, 11:17 UTC), 28 May (path 200, orbit # 34267, 11:05 UTC), and on 4 June (path 201, orbit # 34369). The 26 May overpass was missed because of overcast conditions in Morocco.
Each path is divided in 180 blocks from north to south. Ouarzazate lies in block 66 (on both paths) while parts of the SAMUM flight tracks did penetrate into blocks 65 and 67. Within each block, pixels are arranged on a grid that almost, but not quite follows a west-eastern and a north-southern axis. These "axes" are called *LINE* which increases from North to South, and *SAMPLE* which increases from West to East. Hence, the triple value of block, line, and sample (henceforth *BLS*) determines the location of each pixel within the given MISR path. The *BLS* coordinate depends on the spatial resolution of the chosen dataset. MISR aerosol and surface data come at a resolution of 1.1 km and 17.6 km, respectively. A block is accordingly divided into 32x8 pixels for surface data (resolution 17.6 km) or into 512x128 pixels for aerosol data (resolution 1.1 km).

The *BLS* coordinates of the MISR pixel that contains the city of Ouarzazate are $BLS_{17.6} = (66, 2, 13)$ for 17.6-km data, and $BLS_{1.1} = (66, 43, 217)$ for 1.1-km data. The SAMUM ground station in Tinfou lies in the pixel given by $BLS_{17.6} = (66, 6, 21)$ and $BLS_{1.1} = (66, 100, 337)$.

For programming in IDL, NASA provides algorithm libraries to convert longitude/latitude coordinates into the BLS system, and vice versa (functions `MTK_BLS_TO_LATLON` and `MTK_LATLON_TO_BLS` of the MISR Tool-Kit). Any point on Earth can thus be referred to by fractional *BLS* coordinates as well. Our location at Ouarzazate airport (6.905°W, 30.933°N) converts to $BLS_{17.6} = (66, 2.1976, 13.0726)$ and $BLS_{1.1} = (66, 42.6611, 216.662)$, while the Tinfou ground station is at $BLS_{17.6} = (66, 5.8116, 20.5800)$ and $BLS_{1.1} = (66, 100.485, 336.781)$.

In general, the size of the MISR pixels does not coincide with the size of the surface area detected by the SMART-Albedometer. With the aircraft usually flying rather low, the MISR data are the result of averaging a larger portion of the surface than for the airborne SAMUM data. This possible source of mismatch has to be kept in mind in the following comparison. In order to provide for a geometric matching of the datasets, an empty copy of the MISR grid has been prepared. The geographic coordinates (longitude, latitude) of the SAMUM flight on 19 May are converted to the *BLS* coordinate system, and each surface-albedo value is inscribed into the corresponding pixel of the empty MISR grid. If a MISR pixel contains more than one SAMUM data point, an average value weighted by area fraction is applied, taking into account the geometric relationship between the MISR pixel and the aircraft position and altitude.

[2]UTC is identical to the local time in Morocco.

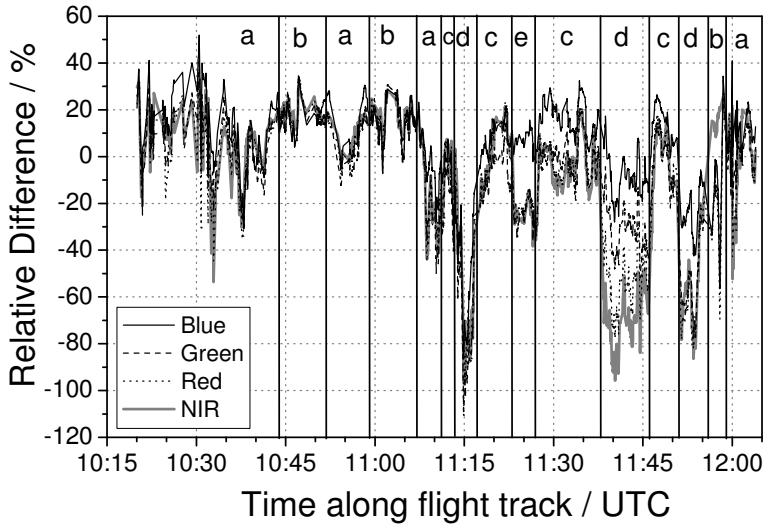

Figure 4.9: Difference between the surface albedo of 19 May derived from the SAMUM Partenavia measurements (ρ_{GERY}) and from MISR (ρ_{MISR}), plotted as a time series of the ratio $(\rho_{\mathrm{GERY}} - \rho_{\mathrm{MISR}})/\rho_{\mathrm{GERY}}$ along the Partenavia flight track. The letters (a)–(e) designate intervals related to certain areas in the scatter plot in Fig. 4.10.

Eventually, all points of the MISR grid that lie beneath the Partenavia flight track have been assigned a SAMUM-derived value of the surface albedo. The difference between all these values and the corresponding MISR values is calculated at all four wavelengths of MISR (Fig. 4.9). For most of the flight time, the difference ranges within ±30 %, while there are certain intervals in which the difference takes considerably higher values (up to 100 %). The data points in these intervals tend to lie in characteristic point clouds when the surface-albedo values of MISR and of SAMUM are plotted against each other (Fig. 4.10). The three intervals with the highest deviations correspond to points in cloud (d). No other intervals have points in this point cloud. The first of these intervals (11:13–11:17 UTC) was measured above rough terrain with slopes and shadows, which yield a different measurement signal depending on the viewing geometry. As both pixel size and viewing angle differ between MISR and the SMART-Albedometer, the result differs accordingly. The difference between the data from both instrument is not wavelength-dependent, as one would expect for a purely geometric reason. Most of the remaining intervals correspond to points in regions (a)–(c) where the difference between the MISR and the SMART-Albedometer data is small. Points of groups (a) and (b) have been measured at flight altitudes less than 300 m above ground, while during the measurement of the points in groups (c), (d), and (e) the aircraft was between 300 m and 1000 m above ground.

Another likely reason for such strong disagreement are local changes of the aerosol properties. The airborne data have been derived using the aerosol optical properties measured at the Tinfou station (which is strictly representative only for the lowest atmospheric layer) and the extinction profile from lidar measurements at Ouarzazate airport. While

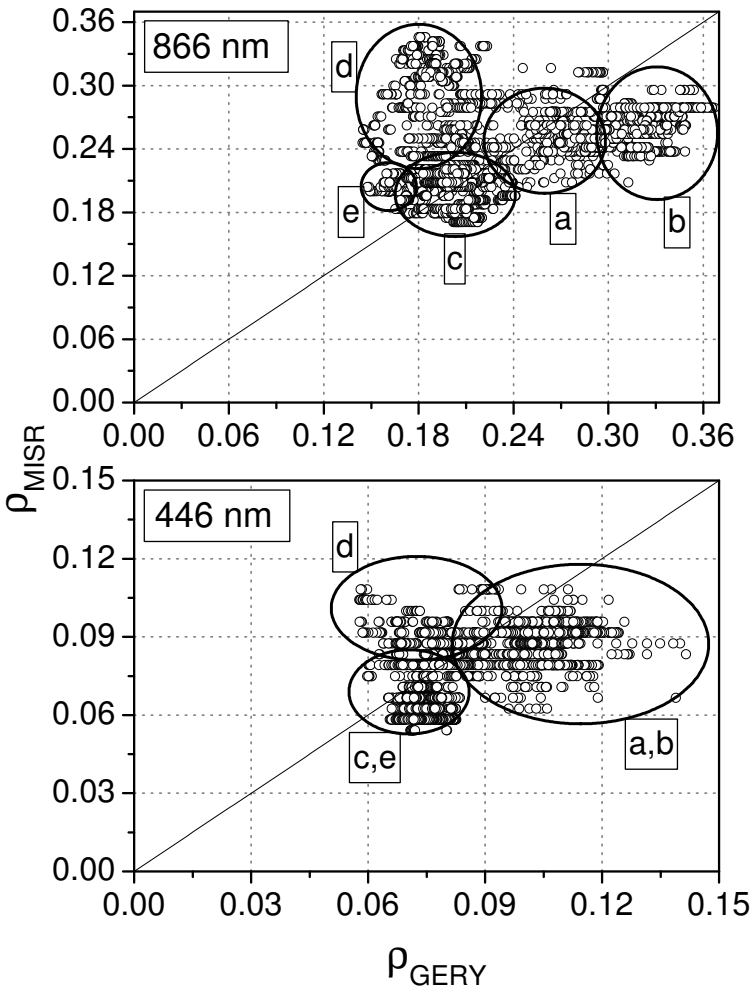

Figure 4.10: Scatter plot of the surface albedo of 19 May derived from the SAMUM Partenavia (GERY) measurements and from MISR. The intervals (a)–(e) in Fig. 4.9 are represented as point clouds in this plot, which are more distinct for longer wavelengths than for shorter ones. Here, the blue channel 446 nm (lower panel) and the NIR channel at 866 nm (upper panel) are shown. In regions (a) and (b) the Partenavia aircraft was flying at altitudes less than 300 m above ground, while in regions (c)–(e) it was at altitudes between 300 and 1000 m above ground.

observed regional fluctuations of the AOD of 30 % in the measurement region do not have a big impact on the surface-albedo retrieval from airborne data (see Section 4.4), a varying choice of best-fit aerosol model determined by the MISR algorithms could lead to a regional variation of the chosen aerosol optical properties thus of the surface-albedo retrieval. This would explain the abrupt start and end of the other two (d) intervals of large MISR/SAMUM difference at MISR pixel borders, and also the wavelength dependence of the difference due to the spectral behaviour of the assumed optical properties.

5 The radiative forcing of Saharan dust

One of the major objectives of SAMUM is the radiative effect of Saharan dust. The measurements in Morocco have provided a dataset that for the first time combines aerosol information (spectral AOD, $\tilde{\omega}$, g, vertical extinction profiles) and the spectral surface albedo which can be esteemed regionally representative. This makes it possible to investigate the influence of the actual spectral surface albedo on the dust radiative forcing in the north-western Sahara.

The radiative forcing (or radiative effect) of a perturbation (subscript "pert") is defined as

$$\Delta F = \left(F^{\downarrow} - F^{\uparrow}\right)_{\text{pert}} - \left(F^{\downarrow} - F^{\uparrow}\right)_{0} . \tag{5.1}$$

In this work, the *perturbation is Saharan dust*. It is important to keep in mind that the radiative forcing of Saharan dust is calculated in dependence on the surface albedo, which is a boundary parameter here, and that it is *not* the radiative forcing of surface-albedo changes or variations. In each calculation of the radiative forcing ΔF, two situations are compared that are entirely identical to each other with the only exception that the first does contain Saharan dust (the "perturbed" case), while the second does not (the "clean" case). In particular, the surface albedo is the same in both terms of the difference.

Furthermore, extraterrestrial perturbations are neglected which means that

$$F_{\text{pert}}^{\text{TOA}\downarrow} = F_{0}^{\text{TOA}\downarrow} . \tag{5.2}$$

This leads to the simplification

$$\Delta F^{\text{TOA}} = F_{0}^{\text{TOA}\uparrow} - F_{\text{pert}}^{\text{TOA}\uparrow} . \tag{5.3}$$

At the surface, the upwelling radiation is determined by the surface albedo ρ and the downwelling radiation:

$$F^{\text{surf}\uparrow} = \rho F^{\text{surf}\downarrow} \tag{5.4}$$

which leads to the simplification

$$\Delta F^{\text{surf}} = (1-\rho)\left(F_{\text{pert}}^{\text{surf}\downarrow} - F_{0}^{\text{surf}\downarrow}\right) . \tag{5.5}$$

5.1 Spectral solar forcing

Using the *libRadtran* radiative transfer model, the shortwave radiative effect of Saharan mineral dust has been calculated for typical dust conditions during SAMUM. The dataset of 19 May, 2006, has been chosen for these calculations, because this was one of the "golden

days" of the field campaign, which means that all instruments were in operation on that day and all needed data are available. Furthermore, the dust conditions of this day are rather typical for most of the experiment period (cf. Table 4.1).

The dependence of the spectral radiative forcing of Saharan dust on different parameters has been investigated by repeating the calculation with different assumption about dust properties ($\tilde{\omega}$, g) and the spectral surface albedo. The dust single-scattering albedo $\tilde{\omega}$ and the asymmetry parameter g have been varied by $\pm 10\,\%$. Three typical spectra of the surface albedo have been used: the standard hamada surface type (Fig. 4.3*a*), the extremely bright salt-crust surface of the dry Iriki lake (Fig. 4.3*d*), and a vegetation type from an oasis (Fig. 4.3*b*). Also the solar zenith angle has been changed between 12° and 30° which have been typical values at the start and at the end of the measurement flights.

For the typical hamada surface, Fig. 5.1 shows that the change of the solar zenith angle during the flight gives rise to only a small change in the radiative effect of the dust (compare upper and lower panel). However, changing the assumed single-scattering albedo of the dust particles has a huge impact: an aerosol with reduced $\tilde{\omega}$ values absorbs more radiation, i.e. more radiative energy is kept within the atmosphere. The dust therefore leads to positive values of ΔF at TOA in the entire solar spectrum. In contrast, almost non-absorbing aerosol (enhanced $\tilde{\omega}$ values) leads to generally negative values. More radiation is not absorbed and has a chance to escape back into space, i.e., to change the TOA forcing to more negative values.

Gas absorption bands (oxygen at 762 nm, water vapour) are a common feature of the forcing spectra. Gas absorption reduces the absolute amount of the radiative effect of the dust at the corresponding wavelengths because the number of photons that can "carry" the dust information is reduced. Interestingly, the radiative effect for the actual SAMUM $\tilde{\omega}$ values is small in amount and can change its sign in dependence on the otherwise less relevant solar zenith angle.

These results have to be compared to those shown in Fig. 5.2. Strong changes in the surface albedo, as they have been encountered in south-eastern Morocco, have a strong impact on the local TOA radiative forcing of dust. Over the highly reflecting surface of the dry Iriki salt lake, the radiative effect is generally positive except for extreme low particle absorption coefficients. On the contrary, the low reflectivity of vegetation below 700 nm leads to a generally negative ΔF^{TOA} in this spectral range, even for the strongly absorbing aerosol type. The large surface-albedo increase at 700 nm is clearly reflected in the spectral radiative effect at TOA, as is the decrease between 1 μm and 2 μm.

The impact of the asymmetry parameter g of the aerosol on the TOA radiative forcing is comparable to that of the single-scattering albedo $\tilde{\omega}$. However, Fig. 5.3 shows that it is reduced over bright surfaces. Over a salt lake (upper panel), which is very bright in all spectral regions, the influence of g on the TOA dust radiative forcing is much lower than that of the single-scattering albedo (Fig. 5.1). Over vegetation (lower panel), which

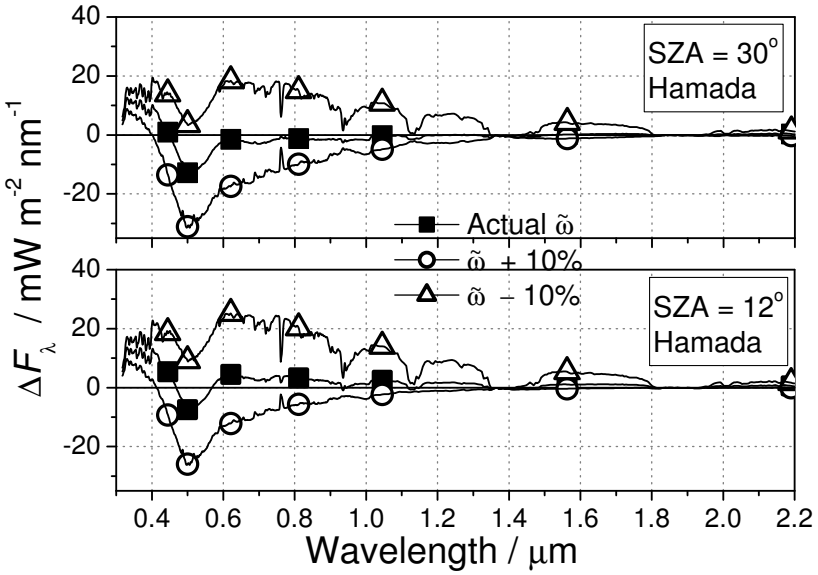

*Figure 5.1: The spectral shortwave radiative effect ΔF at TOA calculated for the dust conditions on 19 May, 2006, and with variations of the dust single-scattering albedo $\tilde{\omega}$ of $\pm 10\,\%$. The upper and lower panels show the radiative effect at the start and at end of the 19-May measurement flight, with a solar zenith angle (SZA) of $30°$ and $12°$, respectively (corresponding to 10:20 and 12:00 UTC). The surface albedo is the hamada standard from Fig. 4.3*a *in both panels.*

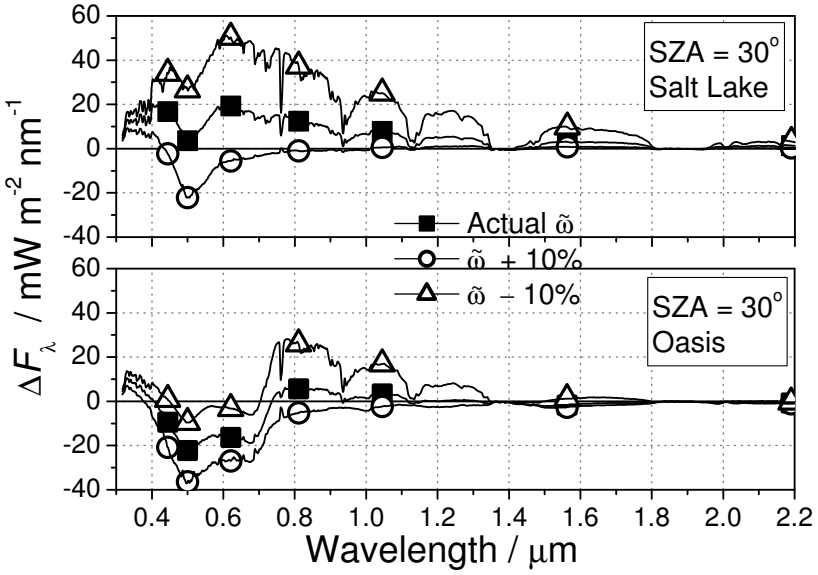

*Figure 5.2: The same as Fig. 5.1, but over different surface types, and at a fixed solar zenith angle (SZA) of $30°$. In the upper panel, the salt-lake albedo spectrum of Fig. 4.3*d *was used, while the lower panel is based on the oasis-type albedo spectrum of Fig. 4.3*b*. Again, the dust single-scattering albedo $\tilde{\omega}$ was varied by $\pm 10\,\%$.*

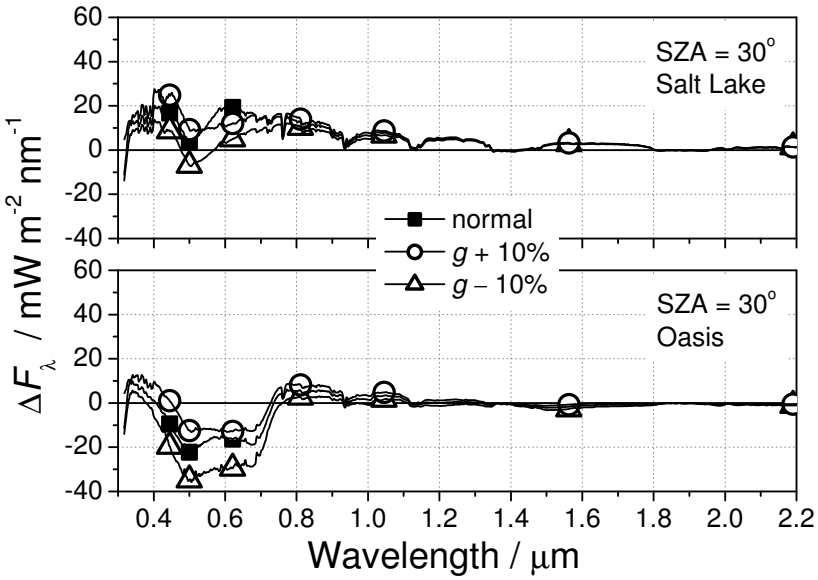

Figure 5.3: The influence of the aerosol asymmetry parameter g on the spectral TOA radiative forcing, for different surface-albedo spectra. The solar zenith angle (SZA) is $30°$*. In the upper panel, the salt-lake albedo spectrum of Fig. 4.3*d *was used, while the lower panel is based on the oasis-type albedo spectrum of Fig. 4.3*b*. g was varied by* $\pm 10\,\%$*.*

is bright only at wavelengths larger than 700 nm, the influence of g is comparable to that of $\tilde{\omega}$ below 700 nm, but lower at longer wavelengths.

5.2 Broadband solar forcing along flight track

In order to quantify the net radiative effect of the Saharan dust in dependence on the surface albedo, it is necessary to add the broadband radiative forcing of the solar (shortwave) and of the thermal infrared (longwave) ranges. As these two ranges require separate treatment, the broadband radiative effect in the solar range is determined in this section, while in the thermal range it is investigated in Section 5.3.

As the previous section has shown, the spectral radiative effect of dust strongly depends on the dust properties, as well as on the surface albedo. It is therefore expected that also the broadband radiative effect may vary widely, especially in the different dust phases during SAMUM (cf. Table 3.4). Three scenarios are investigated here:

- Moderate dust conditions of **19 May** in Ouarzazate, surface albedo to the South of Ouarzazate.
- High dust load of **27 May**, surface albedo in the Zagora basin and Iriki salt lake.
- High dust load of **3 June**, surface albedo to the East of Ouarzazate (Jbel Sahrho and Dadès valley).

For each scenario, the broadband solar TOA radiative forcing of the Saharan dust is calculated along the flight track of that day. At each point of the flight track at which the spectral surface albedo is available on the entire spectral range, the irradiance at TOA and at the surface is modelled twice — once with dust, once without dust — at full spectral resolution, using the spectral surface albedo at that location as boundary parameter. The broadband solar radiative forcing is calculated as the difference of the integrated irradiances of these two cases (Eq. 5.3 and 5.5). The information about the optical properties of the dust (optical depth, single-scattering albedo, asymmetry parameter) have been kept constant in the calculations because only the point measurements at Ouarzazate and Tinfou are available. The remaining parameters (solar zenith angle, surface and aircraft elevation) are also kept constant in order to separate the influence of the surface albedo. Only for the first scenario (19 May), an additional calculation has been performed that included the actual variations of these parameters along the flight track, in order to check whether their influence is significant.

5.2.1 Radiative forcing for 19 May, 2006

This day falls into dust phase IP1 with average dust conditions. A moderate dust load was transported by air flowing in from Algeria, enhanced by local dry-convective dust plumes. The vertical profile of the aerosol extinction coefficient at 355 nm was determined by the POLIS lidar in Ouarzazate (see Fig. 3.11), and extrapolated to other wavelengths using the Ångström coefficients obtained from spectral AOD measurements. The surface albedo is obtained from a flight to the South of Ouarzazate (open squares in Fig. 3.9).

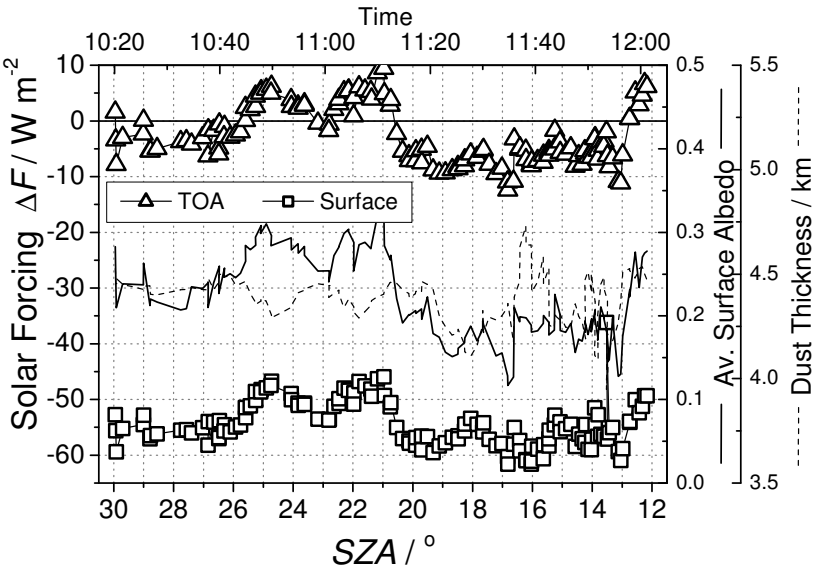

Figure 5.4: The broadband shortwave radiative effect of dust at TOA and at the surface along the Partenavia flight track on 19 May, 2006. The dust layer was assumed to have a constant boundary height above sea level, so the local dust-layer thickness varies with the surface elevation. The two most influential parameters are shown for comparison: surface albedo (solid line) and dust-layer thickness (dashed line). Variations of the solar zenith angle have only minor influence (not shown).

First, a calculation was performed that included all flight-time variations of the surface albedo, the surface elevation, and the solar zenith angle. The dust-layer height, however, was modified for each data point, following the surface elevation. This takes the observation into account that the dust top boundary was flat. Fig. 5.4 shows that most features of the TOA and surface radiative effect coincide with variations of the surface-albedo, but a few peaks — especially of the radiative effect at the surface — coincide with variations of the dust-layer thickness. Except for a single point (at a solar zenith angle of 13.5°), however, the surface elevation varied not strongly enough to have more influence on the radiative effect than the surface albedo.

In order to extract the influence of the surface albedo, we have to eliminate this influence of topography and of the varying position of the sun. To this purpose, the calculation has been repeated, first with the solar zenith angle (SZA), then with both surface elevation and solar zenith angle fixed at average values. The influence of the variations of the solar zenith angle (which took values between 12° and 30°) is small (not shown). The result of the calculation with surface elevation and SZA fixed is shown in Fig. 5.5. The shortwave radiative effect at TOA varies between +10 and $-15\,\mathrm{W\,m^{-2}}$, so even its sign is determined by the surface albedo under the given conditions.

The shortwave radiative effect at the surface varies between -45 and $-65\,\mathrm{W\,m^{-2}}$. It is also dominated by the surface albedo, but a comparison of Fig. 5.4 and Fig. 5.5 shows

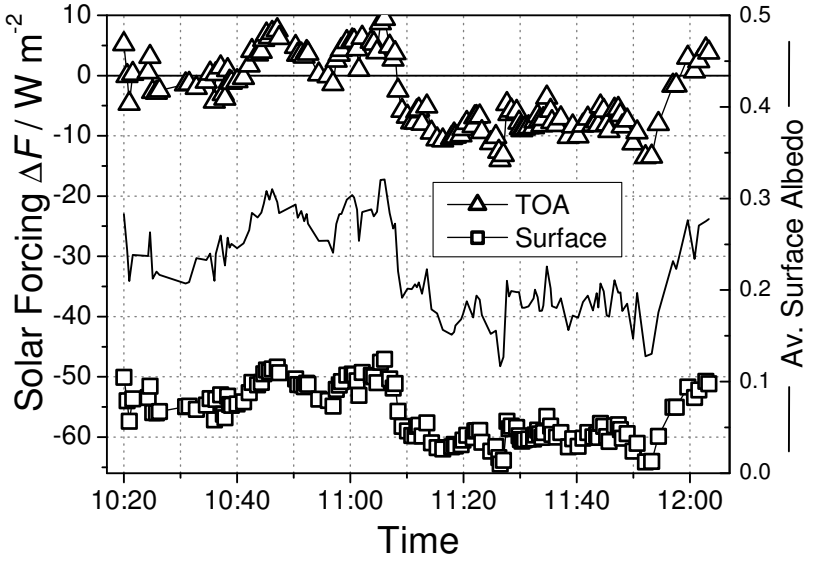

*Figure 5.5: The broadband shortwave radiative effect of dust along the Partenavia flight track on 19 May, 2006, calculated with the solar zenith angle and the surface elevation fixed to average values (*21° *and 1.135 km, respectively; the latter results in a dust-layer thickness of 4.5 km).*

that it is more sensitive to the dust-layer thickness than at TOA.

The dependence of the shortwave radiative effect of Saharan dust on the surface albedo is almost linear (see Fig. 5.6). The correlation coefficient for the linear fit is 0.98 for ΔF at both TOA and the surface. In the following, the slope of this linear fit is denoted as $S\Delta F$, i.e.

$$S\Delta F^{\mathrm{TOA}} = \frac{\partial(\Delta F^{\mathrm{TOA}})}{\partial \rho_{\mathrm{surf}}} \tag{5.6}$$

and

$$S\Delta F^{\mathrm{surf}} = \frac{\partial(\Delta F^{\mathrm{surf}})}{\partial \rho_{\mathrm{surf}}} \tag{5.7}$$

In this case, $S\Delta F^{\mathrm{TOA}} = 121.8\,\mathrm{W\,m^{-2}}$ and $S\Delta F^{\mathrm{TOA}} = 91.1\,\mathrm{W\,m^{-2}}$ which means that the dust radiative effect at TOA and at the surface grows by $12.2\,\mathrm{W\,m^{-2}}$ and $9.1\,\mathrm{W\,m^{-2}}$ per 0.1 surface-albedo increase, respectively.

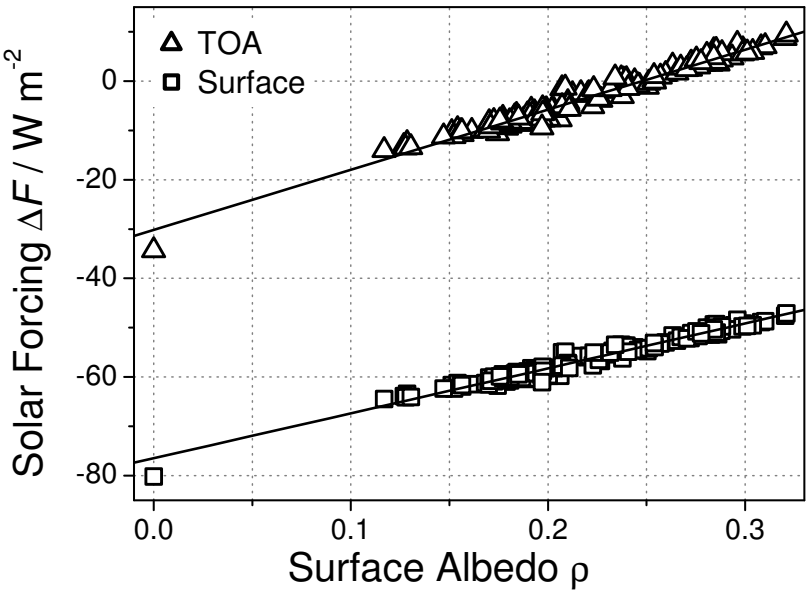

Figure 5.6: Correlation plot of the shortwave radiative effect in dependence on the surface albedo for the flight on 19 May, 2006. An additional hypothetical case with zero surface albedo has been additionally calculated. The linear fits yields the following results: $\Delta F^{\mathrm{TOA}} = -30.2\ W m^{-2} + (121.8\ W m^{-2}) \cdot \rho$ *and* $\Delta F^{\mathrm{surf}} = -76.5\ W m^{-2} + (91.1\ W m^{-2}) \cdot \rho$ *.*

5.2.2 Radiative forcing for 27 May

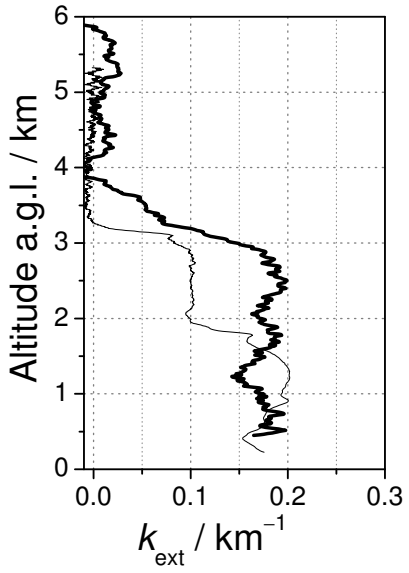

Figure 5.7: The vertical profile of the dust extinction coefficient on 27 May in Tinfou (thick line) and on 3 June in Ouarzazate (thin line), as measured by the POLIS lidar. These data were provided by Birgit Heese, University of Munich.

27 May falls into dust period DP2 in which the highest AOD values in SAMUM have been observed. This coincides with the lowest Ångström exponents observed. This reflects the presence of a large number of large dust particles from local sources, which was typical for DP2. 27 May is not the day with the highest dust load, but nevertheless it has been chosen for this survey because on this day the POLIS lidar was installed at Tinfou in the Zagora basin, and provided the vertical profile of the dust extinction coefficient there (see Fig. 5.7, thick line). The AOD was higher on 25 May, but POLIS was not operational on that date.

The broadband solar radiative forcing of the Saharan dust has been calculated at TOA and at the surface, using the surface albedo measured on the Partenavia flight of the same day (open circles in Fig. 3.9). The study area is the Zagora basin and the dry lake Iriki. Other parts of the flight track have been excluded, as dust conditions varied significantly between Ouarzazate and Zagora.

The obtained radiative forcing is presented in Fig. 5.8. The high surface-albedo values lead to high values of the TOA radiative forcing of up to $30\,\mathrm{W\,m^{-2}}$. The lowest values are $-14\,\mathrm{W\,m^{-2}}$ over dark surfaces. The radiative forcing at the surface ranges between $-67\,\mathrm{W\,m^{-2}}$ and $-35\,\mathrm{W\,m^{-2}}$. The dependence of the radiative forcing on the surface albedo is again almost linear (see Fig. 5.9). The linear fit is shown in Fig. 5.9, the correlation coefficient is 0.94 both at TOA and at the surface. The slope is higher than for the 19-May case: $15.5\,\mathrm{W\,m^{-2}}$ and $11.4\,\mathrm{W\,m^{-2}}$ per 0.1 change in surface albedo at TOA and at the surface, respectively ($S\Delta F^{\mathrm{TOA}} = 154.8\,\mathrm{W\,m^{-2}}$, $S\Delta F^{\mathrm{TOA}} = 113.7\,\mathrm{W\,m^{-2}}$).

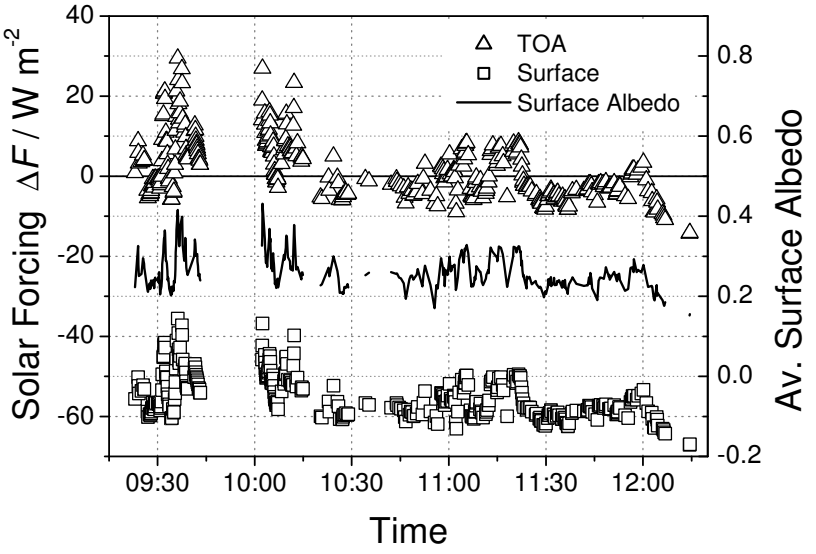

Figure 5.8: The broadband shortwave radiative effect of dust along the Partenavia flight track on 27 May, 2006.

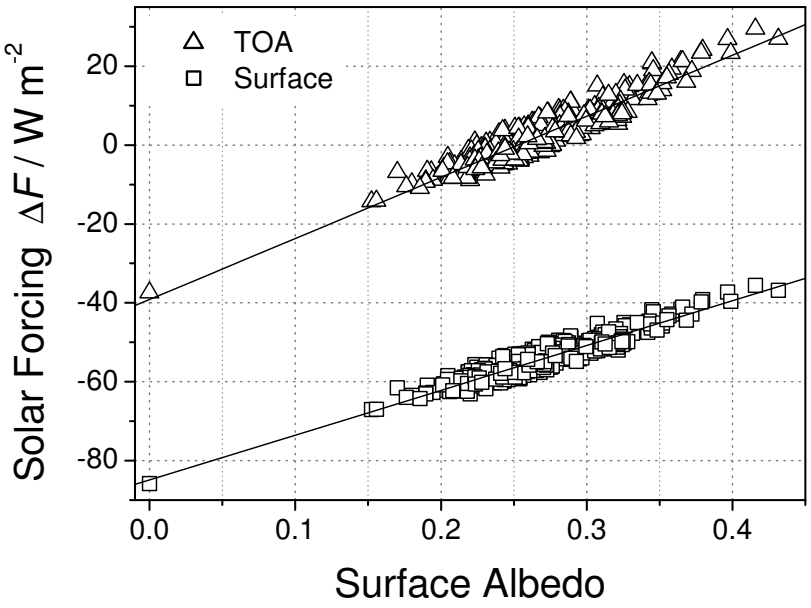

Figure 5.9: Correlation plot of the shortwave radiative effect in dependence on the surface albedo for the flight on 27 May, 2006. An additional hypothetical case with zero surface albedo has been additionally calculated. The linear fits yields the following results: $\Delta F^{\mathrm{TOA}} = -39.1\ W m^{-2} + (154.8\ W m^{-2}) \cdot \rho$ *and* $\Delta F^{\mathrm{surf}} = -84.9\ W m^{-2} + (113.7\ W m^{-2}) \cdot \rho$ *.*

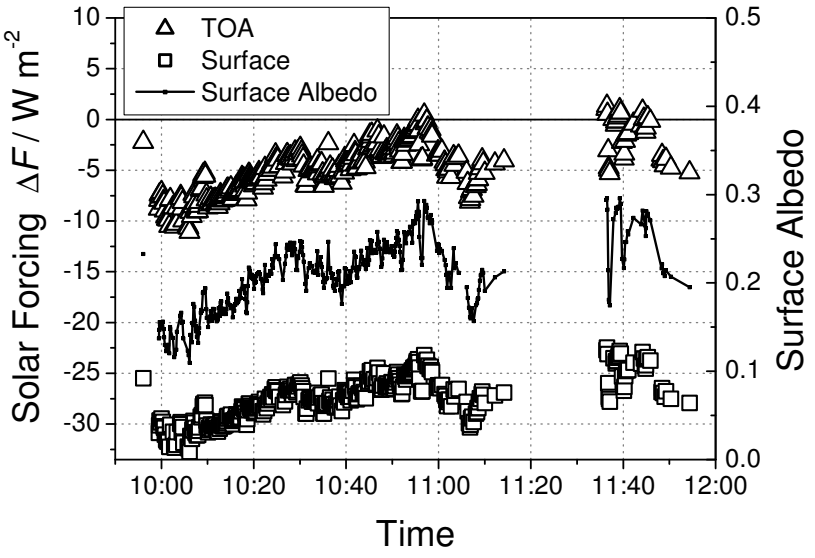

Figure 5.10: The broadband shortwave radiative effect of the Saharan dust observed on 3 June, 2006, calculated over the surface albedo measured to the East of Ouarzazate.

5.2.3 Radiative forcing for 3 June

The surface albedo for the third study is from a flight to the East of Ouarzazate, encircling the *Jbel Sarhro* mountain range and passing through the cultivated Dadès valley. This flight was performed on 30 May (asterisks in Fig. 3.9). This choice is made because this route differs from that on all other flights. However, 30 May was an essentially dust-free day (dust phase IP2) with clean south-westerly air masses. Therefore the surface-albedo data of that day is combined with the aerosol conditions of a dusty day, 3 June.
This day falls into dust phase DP3 with moderately variable dust conditions at medium-high AOD levels. Dust is transported to the SAMUM region from the East. The vertical profile of the dust extinction coefficient (from lidar measurements at 355 nm, see Fig. 5.7, thin line) is again transferred to other wavelengths by the Ångström exponent derived from spectral AOD measurements.

The radiative forcing on 3 June is shown in Fig. 5.10. While the average surface albedo ranges from 0.1 to 0.3, the TOA radiative forcing of the Saharan dust does not exceed $1.5\,\mathrm{W\,m^{-2}}$. The radiative forcing at the surface lies between $-41\,\mathrm{W\,m^{-2}}$ and $-22\,\mathrm{W\,m^{-2}}$. The linear fit in Fig. 5.11 reveals that the slope of the radiative forcing is lower than on 19 and 27 May: at TOA, a 0.1 change in surface albedo leads to a change in radiative forcing of $6.4\,\mathrm{W\,m^{-2}}$, and of $5.3\,\mathrm{W\,m^{-2}}$ at the surface.

5.2.4 Discussion

The surface albedo has a strong impact on the radiative forcing of Saharan dust both at TOA and at the surface. The dependence is well described by a linear fit, so the conditions

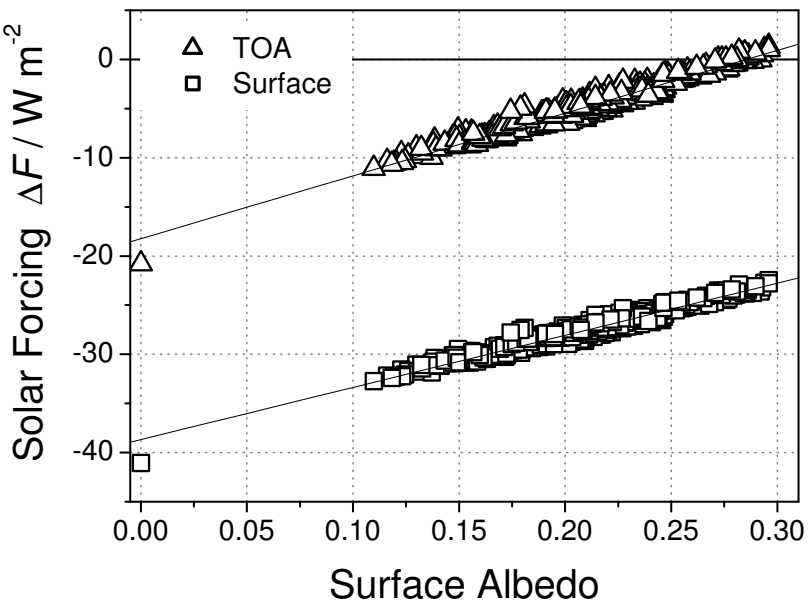

Figure 5.11: Correlation plot of the shortwave radiative effect of the dust observed on 3 June in dependence on the surface albedo measured to the East of Ouarzazate. An additional hypothetical case with zero surface albedo has been additionally calculated. The linear fits yields the following results: $\Delta F^{\mathrm{TOA}} = -18.2\ W m^{-2} + (63.8\ W m^{-2}) \cdot \rho$ *and* $\Delta F^{\mathrm{surf}} = -38.7\ W m^{-2} + (53.0\ W m^{-2}) \cdot \rho$ *.*

for which Eq. 1.14 predicts a linear dependence are fulfilled, i.e. $(1 - \overline{s} \cdot \rho_{\mathrm{surf}})$ is close to unity in all cases in this study, even for the cases of higher AOD.
If the broadband solar radiative forcing is plotted as a function of the average surface albedo, the resulting slopes vary widely for the three analysed days. The following table compares the obtained forcing slopes to the Ångström parameters on these days (from Table 4.1):

Day	α	β	$S\Delta F^{\mathrm{TOA}}$ / W m^{-2}	$S\Delta F^{\mathrm{surf}}$ / W m^{-2}
19 May	0.250	0.321	121.8	91.1
27 May	0.161	0.679	154.8	113.7
3 June	0.134	0.478	63.8	53.0

While the maximum slopes coincide with the maximum of the AOD (the maximum of β) on 27 May, the minima do not agree. The AOD is higher on 3 June than on 19 May, but $S\Delta F$ is stronger on 19 May. This, however, seems more intuitive than the coinciding maxima, at least at TOA where the impact of the surface should be strongest for low AOD values, because at high AOD the dust layer hides the surface from an observer at TOA.
This mismatch is much less pronounced if only the radiative forcing over a "standard" surface is regarded which shall be a surface that has a surface albedo of 0.22. This is the average of all broadband surface-albedo values. Over such a surface, the radiative forcing is obtained from the linear fit formulas as follows:

TOA	P19	P27	P03	$\overline{P}$
AOD 19	75.3	103.5	92.6	90.5
AOD 27	207.1	114.8	177.5	166.5
AOD 03	153.0	145.5	64.4	121.0
$\overline{AOD}$	145.1	121.3	111.5	126.0
surf	P19	P27	P03	$\overline{P}$
AOD 19	57.7	79.9	76.2	71.3
AOD 27	159.2	88.6	145.8	131.2
AOD 03	117.1	112.5	53.2	94.3
$\overline{AOD}$	111.3	93.7	91.7	98.9

Table 5.1: Dependence of the broadband solar radiative forcing at TOA and at the surface on the broadband surface albedo ($S\Delta F^{\mathrm{TOA,surf}}$), given in $\mathrm{W\,m^{-2}\,1^{-1}}$. Columns (P) contain calculations with the vertical profile of the aerosol extinction coefficient chosen for 19 May, 27 May, and 03 June. Rows (AOD) contain calculations with the Ångström parameters (spectral AOD) chosen for the conditions on 19 May, 27 May, and 03 June.

Day	α	β	$\Delta F^{\mathrm{TOA}}(\rho_{\mathrm{surf}} = 0.22)\,/\,\mathrm{W\,m^{-2}}$	$\Delta F^{\mathrm{surf}}(\rho_{\mathrm{surf}} = 0.22)\,/\,\mathrm{W\,m^{-2}}$
19 May	0.250	0.321	−3.4	−56.5
27 May	0.161	0.679	−5.0	−59.9
3 June	0.134	0.478	−4.2	−27.0

Now the radiative forcing at TOA tends to reflect the AOD changes. It is negative in all cases, and strongest when the AOD is highest. The radiative forcing at the surface, however, is almost equal at the maximum *and* at the minimum AOD, but is weaker on 3 June when the AOD is between that of the other two days.

Summarising, the *dependence* of the dust radiative forcing on the surface albedo ($S\Delta F$) is strongly influenced by the aerosol parameters. I have regarded three sets of Ångström parameters, three sets of vertical extinction profiles of a dust layer over three different sets of surface albedo. In an attempt to clarify this situation, the extent of variation is reduced in a new set of calculations. As a first measure, the number of surface-albedo sets is reduced to **one** for all three dust situations. In a second step, the Ångström parameters are also fixed to each single pair of values for all three profiles. Eventually, all nine combinations of profile-shape and spectral AOD are applied. The resulting broadband radiative forcing at TOA and at the surface are given in Table 5.1. The resulting spectral radiative forcing at TOA is shown in Fig. 5.12 for all nine combinations (over one of the darkest and over one of the brightest of surfaces in the dataset).

Both the spectral AOD and the vertical profile of the aerosol extinction coefficient have a strong influence on how strongly the surface albedo can control the radiative forcing of the Saharan dust, even though the variations of the latter are not that strong that this would have been expected. The distribution of minima and maxima in each row or column in Table 5.1 does not follow a clear pattern, when compared to the variation of the optical properties, and the vertical aerosol profile. The large AOD on 27 May produces

the largest values of $S\Delta F$, except for one case when the AOD of 3 June is combined with the profile shape of 27 May. None of the three vertical profiles clearly favours strong or weak values of $S\Delta F$, although their influence is significant.

Meloni *et al.* (2005) found that the shape of the vertical aerosol profile only weakly influences the TOA radiative forcing in the case of weakly absorbing aerosol, but strongly if absorption is high; and that the influence of the vertical aerosol distribution is most important at short wavelengths. Fig. 5.12 does not fully support this principle, because for a fixed spectral AOD (i.e. in each row of the figure) the three different vertical profiles lead to considerable variations of the radiative forcing at TOA. These variations are strongest around 500 nm, but this is mainly caused by the general maximum of solar radiation at those wavelengths. Even in the NIR, at wavelengths around 1.6 microns, there are significant contributions to the TOA radiative forcing, depending on the surface albedo.

These studies have shown that variations or uncertainties in any of the parameters in question (spectral AOD, vertical aerosol profile, spectral surface albedo) can lead to significant variations in the solar radiative forcing of Saharan dust, both at TOA and at the surface.

5.3 Thermal-infrared and net radiative forcing

The broadband longwave radiative effect of the dust in the thermal infrared is calculated in dependence on the surface temperature. The surface temperature has been derived from the continuous pyrgeometer measurements at Ouarzazate airport and varies between 15 °C during the night and maximum values of 56 °C on clear-sky days. The optical properties of the Saharan dust in the thermal infrared have not been measured during SAMUM. Therefore, they are extrapolated to longwave wavelengths by scaling the spectral shape from d'Almeida *et al.* (1991) to the values that have been determined in the shortwave spectral range. The longwave calculations have been performed for only one dust case, because it is highly uncertain in which extent the spectral behaviour from literature is representative for the SAMUM dust, so no trustworthy conclusions about the variations of the longwave optical properties during SAMUM can be made.

The obtained longwave forcing of the dust layer of 19 May is shown in Fig. 5.13. The longwave radiative effect at TOA is strongest when the infrared emission of the surface is strongest, i.e. at high surface temperatures, when it reaches $+22\,\mathrm{W\,m^{-2}}$. Assuming the very same dust layer, at night-time surface temperatures the longwave radiative effect at TOA would drop to $+5\,\mathrm{W\,m^{-2}}$. The decrease can be explained by the decreasing temperature difference between the surface and the cooler dust layer; an observer from above could (thermally) not distinguish the two emitters.

The longwave radiative effect at the surface varies much less with surface temperature, because it is dominated by the temperature of the dust layer which is not varied in these calculations. The dust-layer emissions lead to a surface effect in the range from $+22\,\mathrm{W\,m^{-2}}$

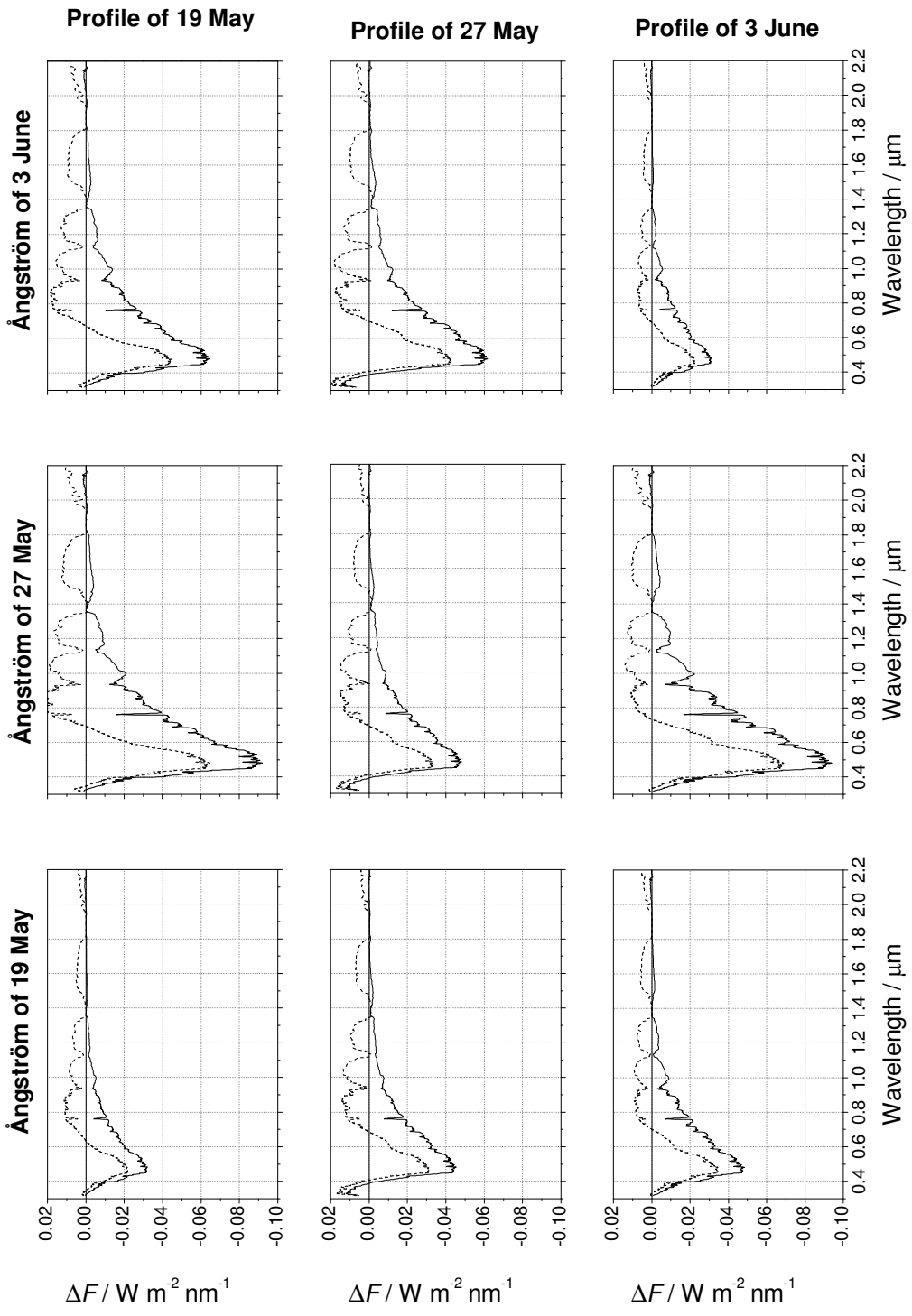

Figure 5.12: Spectral radiative forcing at TOA for all nine combinations of Ångström parameters (rows) and vertical profiles of the aerosol extinction coefficient (columns), from datasets measured during SAMUM on 19 May, 27 May, and 3 June, 2006. The solid lines stand for the radiative forcing of dust over a relatively dark surface (broadband surface albedo of 0.11), the dashed lines over a bright surface (0.30).

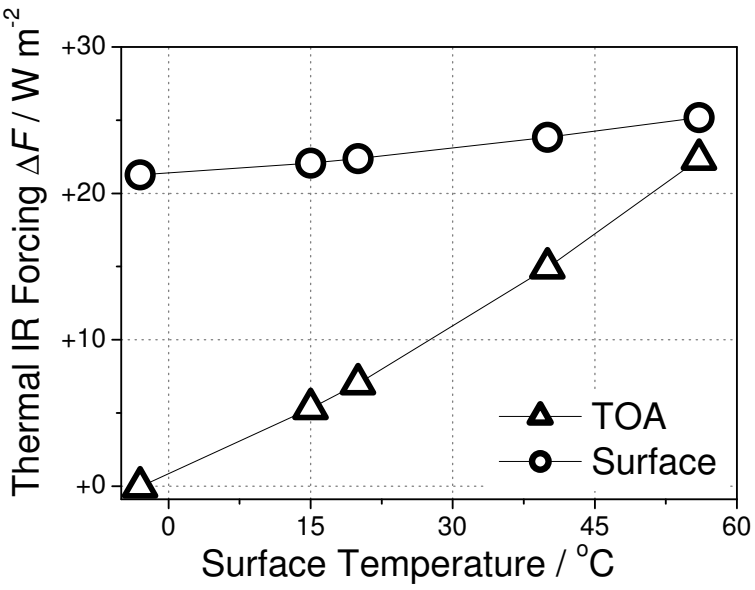

Figure 5.13: Broadband longwave (thermal infrared) radiative effect for the dust conditions of 19 May, 2006, and for the surface-temperature range during SAMUM: $15\,^{\circ}C$ *for the coldest night, and* $56\,^{\circ}C$ *for a hot day's noon. An additional case has been calculated which results in zero radiative effect at TOA. This occurs at* $-3\,^{\circ}C$ *when the surface temperature equals the temperature of the uppermost kilometre of the dust layer.*

to $26\,\mathrm{W\,m^{-2}}$.

In order to get an idea of the overall radiative effect of the Saharan dust, the net effect (shortwave plus longwave) is shown in Fig. 5.14. For the longwave component the surface temperature has been set to two values: 15 °C which is the night-time minimum[1], and 40 °C which is the average surface temperature of the diurnal cycle on 19 May. As the longwave component does not depend on the (shortwave) surface albedo, it leads only to a shift of the values of the solar radiative forcing, not to a change of its slope.

At daytime (the case with surface temperature of 40 °C) the net radiative effect at TOA has only positive values for the entire range of the surface albedo. However, it would turn negative over darker surfaces with broadband surface albedo lower than 0.1. Over cooler surfaces (15 °C), negative values for the net radiative forcing at TOA are obtained for locations where the surface albedo is below 0.2.

The net radiative effect of the dust at the surface is negative for all cases, and is hardly influenced by the change of the surface temperature. It takes values between −42 and $-22\,\mathrm{W\,m^{-2}}$.

[1]Studies of the night-time solar radiative forcing are of course irrelevant. But let us assume that such temperatures are the minimum that can be encountered in the earliest hours of the day.

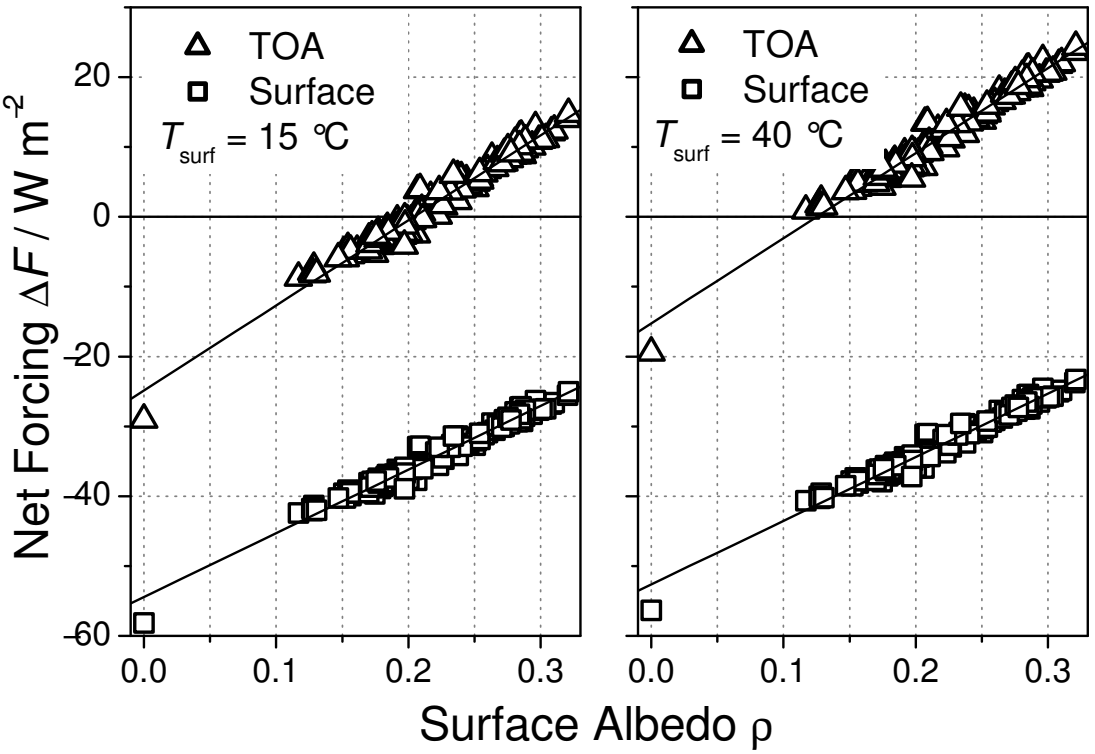

Figure 5.14: Net (shortwave plus longwave) radiative effect of the SAMUM Saharan dust in dependence on the surface albedo for the case of 19 May, 2006, at TOA and at the surface. For the longwave component the surface temperature was set to the minimum temperature of $15\,^{\circ}C$ *(left panel) and to the average value of* $40\,^{\circ}C$ *(right panel).*

6 Summary, Conclusions, and Outlook

The objective of this work is the compilation of a dataset of the spectral surface albedo in a desert region to enable an estimation of the dependence of the radiative forcing of Saharan dust on variations of the reflecting properties of the surface. This work is part of the Saharan Mineral Dust Experiment (SAMUM), a joint project of different research groups with the aim to assess the optical and microphysical properties, the transport, and the radiative effect of Saharan dust close to its sources in north-western Africa.

The spectral surface albedo is derived from airborne measurements of the spectral irradiance. Such measurements are possible with the Spectral Modular Airborne Radiation Measurement System (SMART)-Albedometer.

First, the SMART-Albedometer has been successfully extended into the near-infrared (NIR) to 2200 nm. This was accomplished with a new generation of photodiode-array (PDA) spectrometers for the NIR range that have been tested, characterised and implemented into the original albedometer (which measured up to 1 μm). The SMART-Albedometer now contains six spectrometers that cover almost the entire solar spectral range from 250 nm to 2200 nm and is capable of measuring irradiances, radiances, and actinic flux densities. For these quantities different optical inlets are available that are connected to the spectrometers with optical fibres. In airborne operation the optical inlets are mounted on a stabilisation platform that guarantees horizontal alignment of the inlets within 0.2° for aircraft attitude angles of up to 6°. A first version of NIR spectrometers (MMS) had very poor dark-signal characteristics which made these spectrometers unsuitable for measurements of atmospheric radiation in this system. They have therefore been replaced by Plain-Grating Spectrometers (PGS) with a new generation of photodiode material that produces less dark signal. With these spectrometers, useful airborne irradiance measurements up to 2200 nm are possible. An optical shutter has been incorporated into the system to allow in-flight measurements of the NIR dark signal.

The extended SMART-Albedometer has been used for the first time in the field campaign of the Saharan Mineral Dust Experiment (SAMUM) which was conducted in Morocco from 19 May to 6 June, 2006. The SMART-Albedometer was mounted on a Partenavia aircraft that performed measurement flights from the airport of Ouarzazate. Upwelling and downwelling spectral irradiances have been measured on 13 measurement flights over a variety of surface types. After each flight, a transfer-calibration measurement has been performed to monitor the calibration stability of the system.
From the airborne measurements of the upwelling and downwelling spectral irradiance, the spectral surface albedo has been derived by the application of a non-linear extrapolation algorithm that makes use of atmospheric and aerosol parameters measured by other

SAMUM participants.

The extended SMART-Albedometer and the large extent of available data from all SAMUM participants made it possible to obtain a unique dataset of the surface albedo in south-eastern Morocco. Representative surface-albedo spectra at high spectral resolution have not been available before, nor has information about its regional variability. The main obstacle in airborne measurements of the surface albedo is atmospheric masking of radiation by the atmospheric layer between the aircraft and the surface. But the wealth of data available during SAMUM made it possible to account for this effect and correct its influence.

The dominant spectral shape of the surface albedo is that of the red-coloured stone desert (hamada). These spectra show an increase in surface albedo for wavelengths from 0.3μm to 0.9μm, and a more or less constant surface albedo for longer wavelengths. Typical maximum values of the spectral surface albedo are 0.2 to 0.3. The average of all measurements is 0.10 ± 0.04 at 500 nm, 0.21 ± 0.08 at 672 nm, and 0.24 ± 0.09 at 900 nm. In extreme cases (such as the whitish crust of the dry Iriki lake) the spectral surface albedo reaches values of 0.4–0.5. Due to the aridity of the region, very few spectra show the vegetation step at 700 nm. This vegetation step therefore serves well as an indicator for the presence of plants within the field of view, usually plantations in oases. To this purpose, the Normalized Difference Vegetation Index (*NDVI*) is calculated from the surface albedo at wavelengths below and above the vegetation step, namely 645 nm and 900 nm. For mostly non-vegetated areas, the *NDVI* bears relatively little information. For this reason a similar indicator, the Normalized Difference Red-Colour Index (*NDRI*) is newly defined which is sensitive for changes in the red-colour step that is typical for most of the surface types in the measurement region. With the aid of these two indices, a classification of the surface type has been performed for all measured datasets. Only 1.3 % of all measured spectra have an *NDVI* larger than 0.2 which would indicate that the underlying surface is dominantly covered by vegetation. The average *NDVI* of the covered area is low at 0.09 which means that on a regional scale the radiative effect of vegetation is negligible. The variability of the spectral surface-albedo type is better quantified by the *NDRI*. When comparing the *NDVI* and *NDRI* for different desert regions, the values of the *NDVI* are in a range from 0.07 to 0.16 which does not mean much more than that there is little to no vegetation. The *NDRI*, however, varies between 0.08 for the lunar "desert" and 0.15 for the Sinai region to 0.48 in Utah, with the SAMUM region lying inbetween at 0.25. The *NDRI* is therefore more suitable for a spectral classification of desert surfaces.

SAMUM also provided a unique opportunity to compare airborne and spaceborne surface-albedo measurements. On 19 May, 2006, the MISR instrument on the TERRA satellite passed over Ouarzazate. At the same time, the Partenavia aircraft conducted a measurement flight in the vicinity of Ouarzazate. For a comparison of the surface-albedo results, the surface albedo derived from the airborne measurements has been transferred

onto a grid equal to that of the MISR pixels. During most parts of the flight the difference does not exceed 30 % which is a good level of agreement given the different viewing geometry and the completely different retrieval methods, especially the different handling of aerosol properties: MISR retrieves the AOD from the measured multi-angle radiances by comparing them to a look-up table that contains various aerosol models. Optical properties such as single-scattering albedo and phase function are contained in these models and are not otherwise measured. The optical properties used for the evaluation of the airborne measurements have been obtained from stationary aerosol measurements at Tinfou, which can be trusted for the lowest atmospheric layers where the measurements took place, but need not be constant throughout the entire atmospheric column. Lidar measurements provided the vertical profile of the extinction coefficient but not of other optical properties, and at a location (Ouarzazate) which is 200 km away from Tinfou. In certain areas, however, the difference between the surface albedo derived from the airborne and satellite measurements exceeds those 30 % significantly (up to 100 %). This may partially be caused by irregular underlying terrain which is viewed differently, or by local changes in the aerosol cloud which are not accounted for in the analysis of the airborne data.

For the first time, it was possible to calculate the spectral radiative forcing of the Saharan dust over typical surface types of the experiment region. Three characteristic spectra of the surface albedo have been used in the calculations. The solar zenith angle was set to the lowest (12°) and highest (30°) values encountered during most measurement flights. The aerosol optical properties measured in Tinfou have been used. In addition to the measured single-scattering albedo of the dust, more cases have been investigated with $\tilde{\omega}$ and g increased and reduced by 10 %. The resulting radiative forcing of dust shows little dependence on the solar zenith angle (in the given range of angles). The dependence on the surface albedo, on the single-scattering albedo and on the asymmetry parameter of the aerosol, however, is large. Variations in these quantitites are capable to change the sign of the local radiative forcing. Keeping the surface albedo constant (at the typical hamada-type spectrum), the ± 10 % variations of $\tilde{\omega}$ decide whether the forcing is positive or negative. The radiative forcing decreases with wavelength (because of the reduced incoming solar radiation) and is greatly reduced in amount inside the gas absorption bands because the number of photons that could be influenced by dust has already been reduced, especially by water-vapour molecules.
The influence of the asymmetry parameter g is comparable to that of the single-scattering albedo, but it turned out that this influence is reduced over bright surfaces.
When the spectral surface albedo is varied in the calculations, even stronger variations in the radiative forcing of the dust are observed. Over the extremely bright salt-covered surface of the dry lake Iriki the spectral radiative forcing of the dust reaches values up to three times that obtained with the standard hamada-type surface albedo. On the other hand, the spectral radiative forcing above vegetated areas clearly reflects the spectral reflection characteristics of such surfaces, with negative forcing values (even for the reduced-$\tilde{\omega}$ case) below 700 nm where the surface albedo is low, and a strong increase that corresponds to the vegetation step. Values above 700 nm are similar to those obtained

above hamada surfaces, as the surface albedo is similar for both types in that spectral range.

In addition, the broadband (spectrally integrated) shortwave radiative forcing of the Saharan dust at TOA and at the surface has been calculated along the flight track of three measurement scenarios with moderate and above-average dust load. For 19 May, 2006 (one of the "golden days" of SAMUM), in a first calculation all observed variations of the surface albedo, of the dust-layer thickness (driven by the surface elevation), and of the solar zenith angle have been taken into account. The obtained radiative forcing at TOA varies between $+10\,\mathrm{W\,m^{-2}}$ and $-12\,\mathrm{W\,m^{-2}}$, and the variations follow the variations of the surface albedo along the flight track. Similarly, the radiative forcing at the surface varies between $-62\,\mathrm{W\,m^{-2}}$ and $-45\,\mathrm{W\,m^{-2}}$. In order to rule out possible influences of variations of the solar zenith angle and the dust-layer thickness, these two parameters have been set constant to average values in a second calculation. The resulting radiative forcing at TOA and at the surface changes only slightly compared to the first calculation. This indicates that the surface albedo is the most influential parameter of these three. It alone shifts the values of the calculated radiative forcing and at TOA even determines whether the forcing is positive or negative. A linear fit to the broadband radiative forcing of the dust in dependence on the surface albedo reveals that a 0.1 increase in surface albedo gives rise to a radiative forcing increased by $12.2\,\mathrm{W\,m^{-2}}$ at TOA and by $9.1\,\mathrm{W\,m^{-2}}$ at the surface.

The radiative forcing has also been calculated for two days with higher dust load and on which a vertical profile of the aerosol extinction coefficient was available from lidar measurements. For the case of 27 May, the scenario in the Zagora basin was investigated, while the Ouarzazate dust situation of 3 June was applied for the surface albedo measured in the eastern mountains and valleys. Again, the radiative forcing of the dust has a linear dependence on the broadband surface albedo. However, the slope of this dependence varies widely between the three scenarios. In the case of 27 May, when the AOD was about twice that of the 19-May case study, a 0.1 increase in surface albedo leads to an increase of the radiative forcing of $15.5\,\mathrm{W\,m^{-2}}$ at TOA and $11.4\,\mathrm{W\,m^{-2}}$ at the surface. On 3 June the AOD was lower than on 27 May, but higher than on 19 May, but the impact of the surface albedo on the radiative forcing was lower than on 19 May: a 0.1 increase in surface albedo gives rise to a radiative forcing increased by $6.4\,\mathrm{W\,m^{-2}}$ at TOA and by $5.3\,\mathrm{W\,m^{-2}}$ at the surface. In order to shed some light in this unclear situation, a test series of calculations was performed above a fixed set of surface albedos, and with all combinations of the three datasets of aerosol optical properties and of the vertical aerosol distribution. The outcome, however, does not possess a clear structure. A high AOD tends to increase the impact of the surface albedo on the radiative forcing, but the extent of this still depends significantly on the vertical structure of the dust layer. What is more, the same vertical aerosol profile can have contradicting effect: that of 19 May leads to the highest radiative forcing when combined with the AOD of May 27 and June 3, but with the AOD of 19 May it leads to the weakest radiative forcing.

The most important conclusion of this study is that most parameters that were involved have a strong impact on the radiative forcing of Saharan dust. The influence of the solar zenith angle was low (although this might change in a different situation, or at higher angles). The remaining parameters, namely the spectral surface albedo, the spectral AOD, the single-scattering albedo and asymmetry parameter, and the vertical profile of the aerosol have a significance influence on ΔF both at TOA and at the surface. Without accurate information about all these (and possibly more) quantities, the solar radiative forcing will be hard to estimate. The demand for good measured data and the warning to be cautious with regard to the assumptions about these quantities in models, expressed e.g. by Sokolik and Toon (1996), is again emphasised by this outcome.

The obtained values for the broadband radiative forcing compare well with most of the cited values from literature (Table 1.2). The finding of Díaz *et al.* (2001) that the local shortwave radiative forcing of mineral dust over a broadband land surface albedo of 0.22 amounts to $-4.5\,\mathrm{W\,m^{-2}}$ is fully confirmed by the three case studies in this work. The statement of Balkanski *et al.* (2007) about the shortwave radiative forcing of dust being positive when the broadband surface albedo exceeds 0.2 is confirmed for the case study of 19 May, while the threshold value is different in the two other cases. This reflects the non-negligible influence of variations of aerosol properties which are hard to model.

Also the radiative forcing of the Saharan dust in the longwave (thermal infrared) range (4–42 μm) has been calculated. This has been done using the dust conditions of 19 May, 2006, and the observed range of surface temperatures (between 15 °C and 56 °C at Ouarzazate airport). The radiative forcing at the surface shows only little dependence on the surface temperature, as it is dominated by the temperature profile of the dust. It varies between $+22\,\mathrm{W\,m^{-2}}$ and $+26\,\mathrm{W\,m^{-2}}$. In contrast, the TOA forcing strongly depends on the surface temperature and varies between $+5\,\mathrm{W\,m^{-2}}$ at night time and $+22\,\mathrm{W\,m^{-2}}$ at noon. As zero forcing is obtained when the surface temperature is set equal to the temperature of the uppermost dust layers, the TOA radiative forcing is determined by the temperature *difference* between dust and surface.

The net (shortwave plus longwave) radiative forcing of the Saharan dust has been calculated for a daytime situation with surface temperature being set to the minimum temperature (15 °C) and to the average 40 °C. The net radiative forcing at the surface is generally negative and ranges from $-22\,\mathrm{W\,m^{-2}}$ to $-42\,\mathrm{W\,m^{-2}}$ for the observed surface-albedo range (with minor dependence on the surface temperature). The radiative forcing at TOA ranges from $0\,\mathrm{W\,m^{-2}}$ to $+22\,\mathrm{W\,m^{-2}}$ for the same surface-albedo range, but over darker surfaces than those observed it would reach negative values ($-20\,\mathrm{W\,m^{-2}}$ for a surface albedo of 0). When the surface is cooler (15 °C), a negative radiative forcing is obtained over surfaces with a broadband albedo less than 0.2, while it is still positive over brighter surfaces. This implies that the same dust cloud can lead to a positive radiative forcing at TOA over the continent and to a negative radiative forcing at TOA over the ocean.

Outlook

The SMART-Albedometer has recently been used in the second phase of SAMUM which focuses on Saharan dust that has been transported from the African continent out over the Atlantic Ocean and is partially mixed with biomass-burning aerosol advected from southern West Africa. For this reason, the experiment was located on Cape Verde Islands and took place in January-February 2008, as biomass burning occurs prevailingly in the winter months. Airborne radiance and irradiance measurements, successfully performed with the SMART-Albedometer, will be used to assess the radiative impact of that type of aerosol.

Datasets of the spatial distribution of the surface albedo in Morocco obtained during SAMUM and from several satellite instruments are planned to be used for three-dimensional radiative transfer calculations. So-called adjacency effects scatter radiation from surface areas that are out of sight into the field of view, e.g., of a satellite instrument. This leads to a blurring of the image and to a degradation of the spatial resolution of the measurement, especially for surface properties. The goal of three-dimensional radiative transfer calculations is to estimate this effect and the influence of spatial surface-albedo inhomogeneities on the radiance at TOA, as it is measured by satellites.

Bibliography

Anderson, G., Clough, S., Kneizys, F., Chetwynd, J., and Shettle, E. (1986). *AFGL Atmospheric Constituent Profiles (0-120 km)*. Tech. Rep. AFGL-TR-86-0110, AFGL (OPI), Hanscom AFB, MA 01736.

Ansmann, A., Tesche, M., Knippertz, P., Bierwirth, E., Althausen, D., Müller, D., and Schulz, O. (2009). Vertical profiling of convective dust plumes in southern Morocco during SAMUM. *Tellus* **61B, submitted**.

Aoki, T., Mikami, M., and Liu, W. (2002). Spectral Albedos of Desert Surfaces and Size Distributions of Soil Particles Measured Around Qira and Aksu in the Taklimakan Desert. *J. Arid Land Studies* **11**: 259–266.

Ba, M., Frouin, R., Nicholson, S., and Dedieu, G. (2001). Satellite-Derived Surface Radiation Budget over the African Continent. Part I: Estimation of Downward Solar Irradiance and Albedo. *J. Climate* **14**: 45–58.

Balkanski, Y., Schulz, M., Claquin, T., and Guibert, S. (2007). Reevaluation of mineral aerosol radiative forcings suggests a better agreement with satellite and AERONET data. *Atmos. Chem. Phys.* **7**: 81–95.

Ben-Gai, T., Bitan, A., Manes, A., Alpert, P., and Israeli, A. (1998). Aircraft Measurements of Surface Albedo in Relation to Climate Changes in Southern Israel. *Theor. Appl. Climatol.* **61**: 207–215.

Bierwirth, E., Wendisch, M., Ehrlich, A., Heese, B., Tesche, M., Althausen, D., Schladitz, A., Müller, D., Otto, S., Trautmann, T., Dinter, T., von Hoyningen-Huene, W., and Kahn, R. (2009). Spectral surface albedo over Morocco and its impact on the radiative forcing of Saharan dust. *Tellus* **61B, submitted**.

Bonfils, C., de Noblet-Ducoudré, N., Braconnot, P., and Joussaume, S. (2001). Hot Desert Albedo and Climate Change: Mid-Holocene Monsoon in North Africa. *J. Climate* **14**: 3724–3737.

Bowker, D., Davis, R., Myrick, D., Stacy, K., and Jones, W. (1985). *Spectral Reflectances of Natural Targets for Use in Remote Sensing Studies*. NASA RP-1139, NASA Langley Research Center, Hampton (VA), USA.

Bronstein, I. and Semendjajev, K. (1981). *Taschenbuch der Mathematik*. 20th Edition. BSB B.G. Teubner Verlagsgesellschaft / Verlag Nauka, Leipzig / Moskau.

Cakmur, R., Miller, R., Perlwitz, J., Geogdzhayev, I., Ginoux, P., Koch, D., Kohfeld, K., Tegen, I., and Zender, C. (2006). Constraining the magnitude of the global dust cycle by minimizing the difference between a model and observations. *J. Geophys. Res.* **111**: doi:10.1029/2005JD005791.

Chandrasekhar, S. (1950). *Radiative transfer*. Oxford University Press, London, UK.

Charney, J. (1975). Dynamics of deserts and drought in the Sahel. *Quart. J. Roy. Meteor. Soc.* **101**: 193–202.

Christopher, S. and Jones, T. (2007). Satellite-based assessment of cloud-free net radiative effect of dust aerosols over the Atlantic Ocean. *Geophys. Res. Lett.* **34**: doi:10.1029/2006GL027783.

Claquin, T., Roelandt, C., Kohfeld, K., Harrison, S., Tegen, I., Prentice, I., Balkanski, Y., Bergametti, G., Hansson, M., Mahowald, N., Rodhe, H., and Schulz, M. (2003). Radiative forcing of climate by ice-age atmospheric dust. *Clim. Dyn.* **20**: 193–202.

Claquin, T., Schulz, M., Balkanski, Y., and Boucher, O. (1998). Uncertainties in assessing radiative forcing by mineral dust. *Tellus* **50B**: 491–505.

Coddington, O., Schmidt, K., Pilewskie, P., Gore, W., Bergstrom, R., Román, M., Redemann, J., Russell, P., Liu, J., and Schaaf, C. (2008). Aircraft measurements of surface spectral albedo and its consistency with ground-based and space-borne observations. *J. Geophys. Res.* **in press**: doi:10.1029/2008JD010089.

Costa, M., Sohn, B.-J., Levizzani, V., and Silva, A. (2006). Radiative forcing of Asian dust determined from the synergized GOME and GMS satellite data - a case study. *J. Met. Soc. Japan* **84**: 85–95.

Crowther, B. (1997). *The Design, Construction, and Calibration of a Spectral Diffuse/-Global Irradiance Meter*. Ph.D. thesis, University of Arizona.

d'Almeida, G., Koepke, P., and Shettle, E. (1991). *Atmospheric Aerosols, Global Climatology and Radiative Characteristics*. A. DEEPAK Publishing, Hampton, Virginia, USA.

Deepshikha, S., Satheesh, S., and Srinivasan, J. (2006). Dust aerosols over India and adjacent continents retrieved using METEOSAT infrared radiance. Part II: quantification of wind dependence and estimation of radiative forcing. *Ann. Geophys.* **24**: 63–79.

Deuzé, J., Bréon, F., Devaux, C., Goloub, P., Herman, M., Lafrance, B., Maignan, F., Marchand, A., Nadal, F., Perry, G., and Tanré, D. (2001). Remote sensing of aerosols over land surfaces from POLDER-ADEOS-1 polarized measurements. *J. Geophys. Res.* **106**: 4913–4926.

Díaz, J., Expósito, F., Torres, C., Herrera, F., Prospero, J., and Romero, M. (2001). Radiative properties of aerosols in Saharan dust outbreaks using ground-based and satellite data: Applications to radiative forcing. *J. Geophys. Res.* **106**: 18403–18416.

Diner, D., Beckert, J., Reilly, T., Bruegge, C., Conel, J., Kahn, R., Martonchik, J., Ackerman, T., Davies, R., Gerstl, S., Gordon, H., Muller, J.-P., Myneni, R., Sellers, P., Pinty, B., and Verstraete, M. (1998). Multi-angle Imaging SpectroRadiometer (MISR) Instrument Description and Experiment Overview. *IEEE Trans. Geosci. Remote Sensing* **36**: 1072–1087.

Dobber, M., Goede, A., and Burrows, J. (1998). Observations of the moon by the global ozone monitoring spectrometer experiment: radiometric calibration and lunar albedo. *Appl. Opt.* **37**: 7832–7841.

Forster, P., Ramaswamy, V., Artaxo, P., Berntsen, T., Betts, R., Fahey, D., Haywood, J., Lean, J., Lowe, D., Myhre, G., Nganga, J., Prinn, R., Raga, G., Schulz, M., and Van Dorland, R. (2007). *Climate Change 2007: The Physical Science Basis. Contribution of Working Group I to the Fourth Assessment Report of the Intergovernmental Panel on Climate Change*, chap. Changes in Atmospheric Constituents and in Radiative Forcing. Cambridge University Press, Cambridge, United Kingdom and New York, NY, USA.

Frey, C., Rigo, G., and Parlow, E. (2007). Urban radiation balance of two coastal cities in a hot and dry environment. *Int. J. Remote Sensing* **28**: 2695–2712.

Gamon, J., Field, C., Goulden, M., Griffin, K., Hartley, A., Joel, G., Peñuelas, J., and Valentini, R. (1995). Relationships between NDVI, Canopy Structure, and Photosynthesis in three Californian Vegetation Types. *Ecological Applications* **5**: 28–41.

Grenfell, T. C., Warren, S. G., and Mullen, P. C. (1994). Reflection of solar-radiation by the Antarctic snow surface at ultraviolet, visible, and near-infrared wavelengths. *J. Geophys. Res-Atmos.* **99**: 18.669–18.684.

Gueymard, C. A. (2004). The sun's total and spectral irradiance for solar energy applications and solar radiation models. *SOLAR ENERGY* **76**: 423–453.

Hansen, J., Sato, M., and Ruedy, R. (1997). Radiative forcing and climate response. *J. Geophys. Res.* **102**: 6831–6864.

Hatzianastassiou, N., Katsoulis, B., and Vardavas, I. (2004). Global distribution of aerosol direct radiative forcing in the ultraviolet and visible arising under clear skies. *Tellus* **56B**: 51–71.

Haywood, J., Francis, P., Glew, M., and Taylor, J. (2001). Optical properties and direct radiative effect of Saharan dust: A case study of two Saharan dust outbreaks using aircraft data. *J. Geophys. Res.* **106**: 18417–18430.

Haywood, J., Francis, P., Osborne, S., Glew, M., Loeb, N., Highwood, E., Tanré, D., Myhre, G., Formenti, P., and Hirst, E. (2003). Radiative properties and direct radiative effect of Saharan dust measured by the C-130 aircraft during SHADE: 1. Solar Spectrum. *J. Geophys. Res.* **108**: doi:10.1029/2002JD002687.

Heese, B., , Althausen, D., Dinter, T., Esselborn, M., Müller, T., Tesche, M., and Wiegner, M. (2009). Vertically resolved Dust Optical Properties during SAMUM: Tinfou compared to Ouarzazate. *Tellus* **61B, submitted**.

Heintzenberg, J. (2009). The SAMUM-1 experiment over Southern Morocco: Overview and introduction. *Tellus* **61B, submitted**.

Helmert, J., Heinold, B., Tegen, I., Hellmuth, O., and Wendisch, M. (2007). On the direct and semidirect effects of Saharan dust over Europe: A modeling study. *J. Geophys. Res.* **112**: doi:10.1029/2006JD007444.

Highwood, E., Haywood, J., Silverstone, M., Newman, S., and Taylor, J. (2003). Radiative properties and direct radiative effect of Saharan dust measured by the C-130 aircraft during SHADE: 2. Terrestrial Spectrum. *J. Geophys. Res.* **108**: doi:10.1029/2002JD002552.

Hsu, N., Herman, J., and Weaver, C. (2000). Determination of radiative forcing of Saharan dust using combined TOMS and ERBE data. *J. Geophys. Res.* **105**: 20649–20661.

Hsu, N., Tsay, S., King, M., and Herman, J. (2006). Deep Blue Retrievals of Asian Aerosol Properties During ACE-Asia. *IEEE Trans. Geosci. Remote Sens.* **44**: 3180–3195.

Jacobson, M. (2001). Global direct radiative forcing due to multicomponent anthropogenic and natural aerosols. *J. Geophys. Res.* **106**: 1551–1568.

Jäkel, E., Wendisch, M., Kniffka, A., and Trautmann, T. (2005). Airborne system for fast measurements of upwelling and downwelling spectral actinic flux densities. *Appl.Opt.* **44**: 434–444.

Kaaden, N., Massling, A., Schladitz, A., Müller, T., Kandler, K., Schütz, L., Weinzierl, B., Petzold, A., Tesche, M., Leinert, S., and Wiedensohler, A. (2009). State of Mixing, Shape Factor, Number Size Distribution, and Hygroscopic Growth of the Saharan Anthropogenic and Mineral Dust Aerosol at Tinfou, Morocco. *Tellus* **61B, submitted**.

Knippertz, P., Ansmann, A., Althausen, D., Müller, D., Tesche, M., Bierwirth, E., Dinter, T., Müller, T., von Hoyningen-Huene, W., Schepanski, K., Wendisch, M., Heinold, B., Kandler, K., Petzold, A., Schütz, L., and Tegen, I. (2009). Dust Mobilization and Transport in the Northern Sahara during SAMUM 2006 — a meteorological overview. *Tellus* **61B, submitted**.

Knorr, W. and Schnitzler, K.-G. (2006). Enhanced albedo feedback in North Africa from possible combined vegetation and soil-formation processes. *Climate Dyn.* **26**: 55–63.

Koelemeijer, R., de Haan, J., and Stammes, P. (2003). A database of spectral surface reflectivity in the range 335-772 nm derived from 5.5 years of GOME observations. *J. Geophys. Res.* **108**: doi:10.1029/2002JD002429.

Kokhanovsky, A., Breon, F.-M., Cacciari, A., Carboni, E., Diner, D., Di Nicolantonio, W., Grainger, R., Grey, W., Holler, R., Lee, K.-H., Li, Z., North, P., Sayer, A., Thomas, G., and von Hoyningen-Huene, W. (2007). Aerosol remote sensing over land: A comparison of satellite retrievals using different algorithms and instruments. *Atmos. Res.* **85**: 372–394.

Kylling, A., Persen, T., Mayer, B., and Svenoe, T. (2000). Determination of an effective spectral surface albedo from ground-based global and direct UV irradiance measurements. *J. Geophys. Res-Atmos.* **105**: 4.949–4.959.

Levin, N., Kidron, G., and Ben-Dor, E. (2007). Surface properties of stabilizing coastal dunes: combining spectral and field analyses. *Sedimentology* **54**: 771–788.

Levy, R., Remer, L., Mattoo, S., Vermote, E., and Kaufman, Y. (2007). Second-generation operational algorithm: Retrieval of aerosol properties over land from inversion of Moderate Resolution Imaging Spectroradiometer spectral reflectance. *J. Geophys. Res.* **112**: doi:10.1029/2006JD007811.

Li, Z., Barker, H., and Moreau, L. (2005). A general two-stream algorithm for retrieving spectral surface albedo. *Can. J. Remote Sensing* **31**: 391–399.

Li, Z. and Trishchenko, A. (2001). Quantifying uncertainties in determining SW cloud radiative forcing and cloud absorption due to variability in atmospheric conditions. *J. Atmos. Sci.* **58**: 376–389.

Liou, K. (2002). *An Introduction to Atmospheric Radiation*. Academic Press, San Diego, London.

Liu, X., Penner, J., Das, B., Bergmann, D., Rodriguez, J., Strahan, S., Wang, M., , and Feng, Y. (2007). Uncertainties in global aerosol simulations: Assessment using three meteorological data sets. *J. Geophys. Res.* **112**: doi:10.1029/2006JD008216.

Lyamani, H., Olmo, F., Alcántara, A., and Alados-Arboledas, L. (2006). Atmospheric aerosols during the 2003 heat wave in southeastern Spain II: Microphysical columnar properties and radiative forcing. *Atmos. Env.* **40**: 6465–6476.

Mannstein, H. (1985). The interpretation of albedo measurements on a snowcovered slope. *Arch. Met. Geoph. Biocl.* **36**: 73–81.

Matthews, S., Schwerdtfeger, P., and Hacker, J. (2002). Use of albedo modelling and aircraft measurements to examine the albedo of Nauru. *Aust. Met. Mag.* **51**: 229–236.

Mayer, B. and Kylling, A. (2005). Technical note: The libRadtran software package for radiative transfer calculations - description and examples of use. *Atmos. Chem. Phys.* **5**: 1.855–1.877.

McComiskey, A., Ricchiazzi, P., Gautier, C., and Lubin, D. (2006). Assessment of a three dimensional model for atmospheric radiative transfer over heterogeneous land cover. *Geophys. Res. Lett.* **33**: doi:10.1029/2005GL025356.

Meloni, D., di Sarra, A., di Iorio, T., and Fiocco, G. (2004). Direct radiative forcing of Saharan dust in the Mediterranean from measurements at Lampedusa Island and MISR space-borne observations. *J. Geophys. Res.* **109**: doi:10.1029/2003JD003960.

Meloni, D., di Sarra, A., di Iorio, T., and Fiocco, G. (2005). Influence of the vertical profile of Saharan dust on the visible direct radiative forcing. *J. Quant. Spectrosc. Ra.* **93**: 397–413.

Michalsky, J., Min, Q., Barnard, J., Marchand, R., and Pilewskie, P. (2003). Simultaneous spectral albedo measurements near the Atmospheric Radiation Measurement Southern Great Plains (ARM SGP) central facility. *J. Geophys. Res.* **108**: doi:10.1029/2002JD002906.

Miller, R., Cakmur, R., Perlwitz, J., Geogdzhayev, I., Ginoux, P., Koch, D., Kohfeld, K., Prigent, C., Ruedy, R., Schmidt, G., and Tegen, I. (2006). Mineral dust aerosols in the NASA Goddard Institute for Space Sciences ModelE atmospheric general circulation model. *J. Geophys. Res.* **111**: doi:10.1029/2005JD005796.

Miller, R. and Tegen, I. (1998). Climate response to soild dust aerosols. *J. Clim.* **11**: 3247–3267.

Miller, R., Tegen, I., and Perlwitz, J. (2004). Surface radiative forcing by soil dust aerosols and the hydrological cycle. *J. Geophys. Res.* **109**: doi:10.1029/2003JD004085.

Müller, D., Dubovik, O., Ansmann, A., Weinzierl, B., Kandler, K., Müller, T., Petzold, A., Sinyuk, S., Freudenthaler, V., Heese, B., Tesche, M., Esselborn, M., Althausen, D., von Hoyningen-Huene, W., Schladitz, A., and Knippertz, P. (2009). AERONET Sun Photometer Observations During SAMUM 2006: Comparison of Mineral Dust Optical and Microphysical Properties to Results From Lidar, and Airborne and Ground-Based In-Situ Measurements. *Tellus* **61B, submitted**.

Myhre, G., Grini, A., Haywood, J., Stordal, F., Chatenet, B., Tanré, D., Sundet, J., and Isaksen, I. (2003). Modeling the radiative impact of mineral dust during the Saharan Dust Experiment (SHADE) campaign. *J. Geophys. Res.* **108**: doi:10.1029/2002JD002566.

Myhre, G. and Stordal, F. (2001). On the tradeoff of the solar and thermal infrared radiative impact of contrails. *Geophys. Res. Lett.* **28**: 3119–3122.

Otterman, J. (1981). Satellite and field studies of man's impact on the surface in arid regions. *Tellus* **33**.

Peñuelas, J. and Filella, I. (1998). Visible and near-infrared reflectance techniques for diagnosing plant physiological status. *Trends Plant Sci.* **3**: 151–156.

Perlwitz, J., Tegen, I., and Miller, R. (2001). Interactive soil dust aerosol model in the GISS GCM. 1. Sensitivity of the soil dust cycle to radiative properties of soil dust aerosols. *J. Geophys. Res.* **106**: 18167–18192.

Pilewskie, P., Pommier, J., Bergstrom, R., Gore, W., Howard, S., Rabbette, M., Schmid, B., Hobbs, P. V., and Tsay, S. C. (2003). Solar spectral radiative forcing during the Southern African Regional Science Initiative. *J. Geophys. Res.* **108**: doi:10.1029/2002JD002411.

Pinty, B., Roveda, F., Verstraete, M., Gobron, N., Govaerts, Y., Martonchik, J., Diner, D., and Kahn, R. (2000). Surface albedo retrieval from meteosat. 1. theory. *J. Geophys. Res.* **105**.

Ricchiazzi, P. and Gautier, C. (1998). Investigation of the effect of surface heterogeneity and topography on the radiation environment of Palmer Station, Antarctica, with a hybrid 3-D radiative transfer model. *J. Geophys. Res.* **103**: 6161–6178.

Ricchiazzi, P., Yang, S., Gautier, C., and Sowle, D. (1998). SBDART: A research and teaching software tool for plane-parallel radiative transfer in the Earth's atmosphere. *Bull. Amer. Meteorol. Soc.* **79**: 2101–2114.

Rockwood, A. and Cox, S. (1978). Satellite inferred surface albedo over northwestern Africa. *J. Atmos. Sci.* **35**: 513–522.

Rutan, D., Rose, F., Madigan, J., and Charlock, T. (2003). Surface Albedo at the Atmospheric Radiation Measurement Southern Great Plains Site from Helicopter Observations. In *Thirteenth Atmospheric Radiation Measurement (ARM) Program Science Team Meeting* (Edited by Carrothers, D.). US Department of Energy, Richland, WA.

Schaaf, C. B., Gao, F., Strahler, A. H., Lucht, W., Li, X. W., Tsang, T., Strugnell, N. C., Zhang, X. Y., Jin, Y. F., Muller, J. P., Lewis, P., Barnsley, M., Hobson, P., Disney, M., Roberts, G., Dunderdale, M., Doll, C., d'Entremont, R. P., Hu, B. X., Liang, S. L., Privette, J. L., and Roy, D. (2002). First operational BRDF, albedo nadir reflectance products from MODIS. *Remote Sens. Environ.* **83**: 135–148.

Schladitz, A., Müller, T., Massling, A., Kaaden, N., Kandler, K., and Wiedensohler, A. (2009). In situ measurements of Optical Properties at Tinfou (Morocco) during the Saharan Mineral Dust Experiment SAMUM 2006. *Tellus* **61B, submitted**.

Schollaert, S. and Merrill, J. (1998). Cooler sea surface west of the Sahara Desert correlated to dust events. *Geophys. Res. Lett.* **25**: 3529–3532.

Shell, K. and Somerville, R. (2007a). Direct radiative effect of mineral dust and volcanic aerosols in a simple aerosol climate model. *J. Geophys. Res.* **112**: doi:10.1029/2006JD007197.

Shell, K. and Somerville, R. (2007b). Sensitivity of climate forcing and response to dust optical properties in an idealized model. *J. Geophys. Res.* **112**: doi:10.1029/2006JD007198.

Sicart, J., Ribstein, P., Wagnon, P., and Brunstein, D. (2001). Clear-sky albedo measurements on a sloping glacier surface: A case study in the Bolivian Andes. *J. Geophys. Res.* **106**: 31729–31737.

Sokolik, I. and Toon, O. (1996). Direct radiative forcing by anthropogenic airborne mineral aerosols. *Nature* **381**: 681–683.

Song, J. and Gao, W. (1999). An improved method to derive surface albedo from narrowband AVHRR satellite data: Narrowband to broadband conversion. *J. Appl. Meteorol.* **38**: 239–249.

Stamnes, K., Tsay, S., Wiscombe, W., and Jayaweera, K. (1988). A numerically stable algorithm for discrete-ordinate-method radiative transfer in multiple scattering and emitting layered media. *Appl. Opt.* **27**: 2502–2509.

Stone, R., Anderson, G., Andrews, E., Dutton, E., Shettle, E., and Berk, A. (2007). Incursions and radiative impact of Asian dust in northern Alaska. *Geophys. Res. Lett.* **34**: doi:10.1029/2007GL029878.

Strugnell, N., Lucht, W., and Schaaf, C. (2001). A global albedo data set derived from AVHRR data for use in climate simulations. *Geophys. Res. Lett.* **28**: 191–194.

Sun, Z. and Shine, K. P. (1994). Studies of the radiative properties of ice and mixed-phase clouds. *Quart. J. Roy. Meteor. Soc.* **120**: 111–137.

Tanskanen, A. and Manninen, T. (2007). Effective UV surface albedo of seasonally snow-covered lands. *Atmos. Chem. Phys.* **7**: 2759–2764.

Tegen, I. and Lacis, A. (1996). Modeling of particle size distribution and its influence on the radiative properties of mineral dust aerosol. *J. Geophys. Res.* **101**: 19237–19244.

Tegen, I., Lacis, A., and Fung, I. (1996). The influence on climate forcing of mineral aerosols from disturbed soils. *Nature* **380**: 419–422.

Tesche, M., Ansmann, A., Müller, D., Althausen, D., Mattis, I., Heese, B., Freudenthaler, V., Wiegner, M., Esselborn, M., Pisani, G., and Knippertz, P. (2009). Vertical profiling of Saharan dust with Raman lidars and airborne HSRL in southern Morocco during SAMUM. *Tellus* **61B, submitted**.

Trishchenko, A., Luo, Y., Khlopenkov, K., and Li, Z. (2004). Dynamics of the surface albedo over the ARM SGP area during spring 2003 aerosol IOP. In *Fourteenth ARM Science Team Meeting Proceedings*. US Department of Energy, Washington, D.C.

Tsvetsinskaya, E., Schaaf, C., Gao, F., Strahler, A., Dickinson, R., Zeng, X., and Lucht, W. (2002). Relating MODIS-derived surface albedo to soils and rock types over Northern Africa and the Arabian peninsula. *Geophys. Res. Lett.* **29**: doi:10.1029/2001GL014096.

Veefkind, J., de Leeuw, G., Stammes, P., and Koelemeijer, R. (2000). Regional Distribution of Aerosol over Land, Derived from ATSR-2 and GOME. *Rem. Sens. Env.* **74**: 377–386.

von Hoyningen-Huene, W., Dinter, T., Kokhanovsky, A., Burrows, J., Wendisch, M., Bierwirth, E., Müller, D., and Diouri, M. (2009). Measurements of desert dust optical characteristic at Porte au Sahara during SAMUM. *Tellus* **61B, submitted**.

von Hoyningen-Huene, W., Freitag, M., and Burrows, J. (2003). Retrieval of aerosol optical thickness over land surfaces from top-of-atmosphere radiance. *J. Geophys. Res.* **108**: doi:10.1029/2001JD002018.

Wang, H., Shi, G., Li, S., Li, W., Wang, B., and Huang, Y. (2006). The impacts of optical properties on radiative forcing due to dust aerosol. *Adv. Atm. Sci.* **23**: 441–441.

Wang, J., Bastiaanssen, W., Ma, Y., and Pelgrum, H. (1998). Aggregation of land surface parameters in the oasis-desert systems of north-west China. *Hydrological Processes* **12**: 2133–2147.

Wang, K., Wang, P., Liu, J., Sparrow, M., Haginoya, S., and Zhou, X. (2005). Variation of surface albedo and soil thermal parameters with soil moisture content at a semi-desert site on the western Tibetan plateau. *Boundary-Layer Meteorology* **116**: 117–129.

Webb, A., Stromberg, I., Li, H., and Bartlett, L. (2000). Airborne spectral measurements of surface reflectivity at ultraviolet and visible wavelengths. *J. Geophys. Res.* **105**: 4945–4948.

Webb, A. R., Kylling, A., Wendisch, M., and Jäkel, E. (2004). Airborne measurements of ground and cloud spectral albedos under low aerosol loads. *J. Geophys. Res-Atmos.* **109**: Art. No. D20205.

Wendisch, M. (2002). *Absorption of Solar Radiation in the Cloudless and Cloudy Atmosphere*. Habilitation thesis, 174 pp., Univ. of Leipzig, Leipzig, Germany.

Wendisch, M., Keil, A., Müller, D., Wandinger, U., Wendling, P., Stifter, A., Petzold, A., Fiebig, M., Wiegner, M., Freudenthaler, V., Armbruster, W., von Hoyningen-Huene, W., and Leiterer, U. (2002). Aerosol-radiation interaction in the cloudless atmosphere during LACE 98. Part 1: Measured and calculated broadband solar and spectral surface insolations. *J. Geophys. Res.* **107**: 10.1029/2000JD000226.

Wendisch, M., Müller, D., Schell, D., and Heintzenberg, J. (2001). An airborne spectral albedometer with active horizontal stabilization. *J. Atmos. Oceanic Technol.* **18**: 1856–1866.

Wendisch, M., Pilewskie, P., Jäkel, E., Schmidt, S., Pommier, J., Howard, S., Jonsson, H. H., Guan, H., Schroder, M., and Mayer, B. (2004). Airborne measurements of areal spectral surface albedo over different sea and land surfaces. *J. Geophys. Res-Atmos.* **109**: Art. No. D08203.

Woodward, S. (2001). Modeling the atmospheric life cycle and radiative impact of mineral dust in the Hadley Centre climate model. *J. Geophys. Res.* **106**: 18155–18166.

Wu, J., Fu, C., Jiang, W., Liu, H., and Zhao, R. (2005). A preliminary simulation study of direct radiative forcing of mineral dust aerosol over the East Asia region. *Chinese Journal of Geophysics – Chinese Edition* **48**: 1250–1260.

Wuttke, S., Seckmeyer, G., and Konig-Lang, G. (2006). Measurements of spectral snow albedo at Neumayer, Antarctica. *Annales Geophysicae* **24**: 7–21.

Yoshioka, M., Mahowald, N., Conley, A., Collins, W., Fillmore, D., Zender, C., and Coleman, D. (2007). Impact of desert dust radiative forcing on Sahel precipitation: Relative importance of dust compared to sea surface temperature variations, vegetation changes, and greenhouse gas warming. *J. Climate* **20**: 1445–1467.

Zhou, L., Dickinson, R., Ogawa, K., Tian, Y., Jin, M., Schmugge, T., and Tsvetsinskaya, E. (2003a). Relations between albedos and emissivities from MODIS and ASTER data over North African Desert. *Geophys. Res. Lett.* **30**: doi:10.1029/2003GL018069.

Zhou, L., Dickinson, R., Tian, Y., Zeng, X., Dai, Y., Yang, Z.-L., Schaaf, C., Gao, F., Jin, Y., Strahler, A., Myneni, R., Yu, H., Wu, W., and Shaikh, M. (2003b). Comparison of seasonal and spatial variations of albedos from Moderate-Resolution Imaging Spectroradiometer (MODIS) and Common Land Model. *J. Geophys. Res.* **108**: doi:10.1029/2002JD003326.

Zhu, A., Ramanathan, V., Li, F., and Kim, D. (2007). Dust plumes over the Pacific, Indian, and Atlantic oceans: Climatology and radiative impact. *J. Geophys. Res.* **112**: doi:10.1029/2007JD008427.

List of symbols

Symbol	Unit	Description
A	m^2	Area
b_{abs}	m^{-1}	Absorption coefficient
b_{ext}	m^{-1}	Extinction coefficient
b_{sca}	m^{-1}	Scattering coefficient
$c_i, i = 0..9$	$(^\circ)^{-i}$	Polynomial coefficients for the direct cosine correction function
$d_i, i = 0..9$	nm^{-i}	Polynomial coefficients for the diffuse cosine correction function
d_g	1	Diffuse fraction
E	J	Energy
f_{abs}	$\mathrm{W\,m^{-2}}$	Absolute calibration factors
f_{cos}	1	Cosine correction function
f_{diff}	1	Diffuse cosine correction function
f_{tra}	1	Transfer calibration factors
F	$\mathrm{W\,m^{-2}}$	Irradiance
F_λ	$\mathrm{W\,m^{-2}\,nm^{-1}}$	Spectral irradiance
F_0	$\mathrm{W\,m^{-2}}$	Initial, or extraterrestrial, irradiance
$F^\uparrow$	$\mathrm{W\,m^{-2}}$	Upwelling Irradiance
$F^\downarrow$	$\mathrm{W\,m^{-2}}$	Downwelling Irradiance
F_{cal}	$\mathrm{W\,m^{-2}}$	Measured irradiance during calibration
F_{calc}	$\mathrm{W\,m^{-2}}$	Calculated irradiance
F_{diff}	$\mathrm{W\,m^{-2}}$	Diffuse component of the irradiance
F_{dir}	$\mathrm{W\,m^{-2}}$	Direct component of the irradiance
F_{exp}	$\mathrm{W\,m^{-2}}$	“Experiment” irradiance during transfer calibration
F_{lab}	$\mathrm{W\,m^{-2}}$	“Laboratory” irradiance during transfer calibration
F_{meas}	$\mathrm{W\,m^{-2}}$	Measured irradiance
F^{a}	$\mathrm{W\,m^{-2}}$	Actinic flux density
g	1	Asymmetry parameter
h	m	Flight altitude above ground
i, j	1	Index variables
I	$\mathrm{W\,m^{-2}\,sr^{-1}}$	Radiance
n_{pix}	1	Total number of pixels
$p(\vartheta)$	1	Phase function
r	m	Radius
R	1	Reflectance
s	m	Distance, path length
$S_{\mathrm{I,II,III}}$	nm^{-1}	Slope of spectral intervals $\Lambda_{\mathrm{I,II,III}}$

Symbol	Unit	Description
$S\Delta F$	$\mathrm{W\,m^{-2}\,1^{-1}}$	Derivative of ΔF with respect to surface albedo
t	s	Time
t_{int}	ms	Integration time
W_{cal}	1	Measured raw irradiance signal during calibration
y_n	1	Dark signal of pixel n
z	m	Altitude
z_0	m	Surface elevation
α	1	Ångström exponent
β	1	Ångström coefficient (AOD at $1\,\mu$m)
ΔF	$\mathrm{W\,m^{-2}}$	Radiative forcing (or radiative effect)
ΔF_λ	$\mathrm{W\,m^{-2}\,nm^{-1}}$	Spectral radiative forcing
θ	$^\circ$	Angle of incidence
θ_s	$^\circ$	Solar zenith angle
θ_{sig}	$^\circ$	Viewing angle that yields a significant contribution to the signal
ϑ	$^\circ$	Scattering angle
λ	nm or μm	Wavelength
Λ	nm or μm	Spectral Interval
μ	1	$= \cos\theta$
ρ	1	Albedo
ρ_{surf}	1	Surface albedo
$\sigma(\theta_{\mathrm{sig}})$	1	Significance of signal contribution from θ_{sig}
τ	1	Aerosol Optical depth
τ^i	1	Calculated transmittance in iteration i
Ω	sr	Solid angle
$\tilde{\omega}$	1	Single-scattering albedo

List of abbreviations

AERONET	Aerosol Robotic Network
AFDM	Actinic Flux Density Meter
AGL	Above ground level
AHS	Artificial Horizon System
AOD	Aerosol optical depth
ASL	Above sea level
ASTER	Advanced Spaceborne Thermal Emission and Reflection Radiometer
AVHRR	Advanced Very High Resolution Radiometer
BAERI	Bay Area Environmental Research Institute
BERTHA	Backscatter Extinction lidar-Ratio Temperature Humidity profiling Apparatus
BHR	Bihemispherical Reflectance (same as surface albedo)
BLS	Block-line-sample coordinate system of MISR
CORAS	Compact Radiation Measurement System
CPC	Condensation Particle Counter
DC	Direct current (Gleichstrom)
DFG	Deutsche Forschungsgemeinschaft (German Research Foundation)
DISORT2	Discrete Ordinate algorithm, version 2
DLR	Deutsches Zentrum für Luft- und Raumfahrt (German Aerospace Centre)
DRE	Direct radiative effect
EM	Electromagnetic
EOS	Earth Observing System
ESA	European Space Agency
FEE	Front-end electronics
FWHM	Full width at half maximum
GPS	Global Positioning System
IfT	Leibniz Institute for Tropospheric Research, Leipzig, Germany
InGaAs	Indium-Gallium Arsenide
IPCC	Intergovernmental Panel on Climate Change
JPL	Jet Propulsion Laboratory, USA
LH	Lower hemisphere
libRadtran	Library for radiative transfer
LOWTRAN	Low-resolution transmittance
LW	Longwave (terrestrial / thermal infrared) spectral range
MERIS	Medium-Resolution Imaging Spectrometer
MISR	Multi-Angle Imaging Spectroradiometer
MMS	Monolithic Miniature Spectrometer

MOCIS	Mobile Cascade Impaction System
MODIS	Moderate Resolution Imaging Spectroradiometer
NASA	National Aeronautics and Space Administration, USA
NDRI	Normalized Difference Red-Colour Index
NDVI	Normalized Difference Vegetation Index
NIR	Near Infrared spectral range (here, 1000–2200 nm)
NIST	National Institute for Standards and Technology, USA
NOP	Number of overloaded pixels
OMI	Ozone Measurement Instrument
PDA	Photo-diode array
PGS	Plain-Grating Spectrometer
POLIS	Portable Lidar System
PSAP	Particle Soot/Absorption Photometer
RH	Relative Humidity
SAMUM	Saharan Mineral Dust Experiment
SBDART	Santa Barbara DISORT Atmospheric Radiative Transfer
SMART	Spectral Modular Airborne Radiation Measurement System
SSFR	Solar Spectral Flux Radiometer
STRAP	Stabilized Radiometer Platform
SW	Shortwave (solar) spectral range
SZA	Solar zenith angle
TOA	Top of atmosphere
TOMS	Total Ozone Mapping Spectrometer
UH	Upper hemisphere
USA	United States of America
UNEP	United Nations Environment Programme
UTC	Universal Time Coordinated
UV	Ultraviolet
VIS	Visible spectral range (here, 250–1000 nm)
VN1/2/3/4	Optical inlets for VIS and NIR
WMO	World Meteorological Organization
1D	One-dimensional
3D	Three-dimensional

List of Figures

List of Tables